Insights into early winter Southern Indian Ocean dissolved iron distributions and remineralisation using excess barium (GEOTRACES GIPr07 cruise)

Natasha René van Horsten

THESE DE DOCTORAT EN

COTUTELLE INTERNATIONALE DE

L'UNIVERSITE
DE BRETAGNE OCCIDENTALE

ECOLE DOCTORALE N° 598
Sciences de la Mer et du littoral
Spécialité : Chimie marine

STELLENBOSCH UNIVERSITY
Department of Earth Sciences
Spécialité : Earth Sciences

Par

Natasha René VAN HORSTEN

Insights into early winter Southern Indian Ocean dissolved iron distributions and remineralisation using excess barium (GEOTRACES GIPr07 cruise)

Distributions en fer dissous et en baryum particulaire pour l'étude de la reminéralisation en début d'hiver dans le secteur Indien de l'Océan Austral (mission GEOTRACES GIPr07)

Thèse présentée et soutenue à Stellenbosch, Afrique du Sud, 16 novembre 2021

Unité de recherche : Laboratoire de Sciences de l'Environnement Marin
: TracEx laboratory

Rapporteurs avant soutenance :

Damien CARDINAL	Professeur des Universités, Sorbonne Université, Paris, France
Murat ARDELAN	Professor, Norwegian University of science and technology, Trondheim, Norway
Suzanne FIETZ	Senior lecturer, Stellenbosch University, Stellenbosch, South Africa

Composition du Jury :

Président : Damien CARDINAL	Professeur des Universités, Sorbonne Université, Paris, France
Murat ARDELAN	Professor, Norwegian University of science and technology, Trondheim, Norway
Suzanne FIETZ	Senior lecturer, Stellenbosch University, Stellenbosch, South Africa

Directeurs de thèse

Géraldine SARTHOU	Directrice de Recherche, LEMAR, Brest, France

Invités

Alakendra ROYCHOUDHURY	Professor, Department of Earth Sciences, University of Stellenbosch, Stellenbosch, South Africa
Thato MTSHALI	Head of Chemistry, Department of Environment, Forestry and Fisheries, Cape Town, South Africa
Eva BUCCIARELLI	Maître de Conférences, UBO, LEMAR, Brest, France
Hélène PLANQUETTE	Directrice de Recherche, CNRS, LEMAR, Brest, France

‘How inappropriate to call this planet Earth when it is quite clearly Ocean.’ Arthur C. Clarke

Acknowledgements

Throughout the duration of my PhD I have received a great deal of support and assistance, both professionally and personally. Firstly, I would like to thank my supervisors in France, Dr Eva Bucciarelli, Dr Hélène Planquette and Dr Géraldine Sarthou. Thank you for giving me the opportunity to work with you and never giving up on my ability to make it to the end of the road. To my South African supervisors, Dr Thato Mtshali and Prof. Alakendra Roychoudhury, thank you for making this all possible for me. To all my supervisors, your knowledge and guidance have contributed to my career in an invaluable way. Thank you to my external PhD committee members Dr Alessandro Tagliabue and Dr Catherine Jeandel for your invaluable input and reassurances.

Thank you to all the funding bodies who made this endeavour possible, the ISblue project, Interdisciplinary graduate school for the blue planet and the French government under the program "Investissements d'Avenir", the South African National Research Foundation, the French-South African National Research Foundation Collaboration, the South African Department of Science and Technology, French Ministry of National Education, Higher Education and Research, the French Ministry of Foreign Affairs and International Development, CSIR, and the SOCCO research group. With the support received from all these institutions I have received the support of a fantastic international collaboration.

The captains and crew members of the R/V *SA Agulhas II*, as well as all the research participants who assisted with my fieldwork, have been part of my journey for quite some time now, preceding my PhD, their invaluable efforts have been the reason for any success achieved in the harsh conditions of the Southern Ocean. Thank you to Prof. Isabelle Ansorge, Dr Marcel du Plessis, Dr Esther Portela and Dr Sarah-Anne Nicholson for your assistance with all things physics related. Dr Natalia Llopis Monferrer your schematic diagram creating skills were much appreciated, making my manuscript that much more visually appealing.

Across continents, to my colleagues who became friends, Tommy, Ryan, Natalia, Hannah, David, Sandy, Sarah, Tahlia and the list goes on. I want to thank you all for your professional input when asked and your support as friends. Thank you to everyone at LEMAR, ifremer, UCT, Stellenbosch University, and SOCCO who were part of this journey, every bit helped.

To friends who have become family, Tommy, Lee, Michelle, Justin, Waleed, Thys, Johan and Jason, you have been there for all the ups and down over the last few years and without you I would not have made it out whole. Finally, to my family who even though you are far away, you support throughout everything I have taken on in my life is the reason I have made it this far.

Although one might feel quite isolated during such an endeavour, especially in the times we currently find ourselves, it truly has been a massive network of support and assistance that has made it possible for me to get to this point.

Table of Contents

List of Figures

Chapter 1

Chapter 2

Chapter 3

Chapter 4

Appendix A

Appendix B

List of Tables

Chapter 2

Chapter 3

Appendix A

Appendix B

Appendix C

Abbreviations

^{234}Th	Naturally occurring thorium isotope, produced by the decay of uranium-238
^{238}U	Most abundant uranium isotope
AABW	Antarctic bottom water
AAIW	Antarctic intermediate water
AASW	Antarctic surface water
ACC	Antarctic circumpolar current
AOU	Apparent oxygen utilisation
ARC	Agulhas return current
AZ	Antarctic zone
Ba	Barium
$Ba_{residual}$	Background barium excess signal referred to as barium residual
Ba_{xs}	Particulate biogenic barium in the form of barite crystals referred to as barium excess
BCP	Biological carbon pump
C	Carbon
CbPM	Carbon-based productivity model
CDW	Circumpolar deep water
Chl α	Chlorophyll α (phytoplankton light harvesting pigment)
CO_2	Carbon dioxide
CTD	Conductivity-Temperature-Depth
dFe	Dissolved iron
DWA	Depth weighted average
Fe	Iron
Fe*	Iron limitation tracer
HF	Hydrofluoric acid
HNLC	High nutrient low chlorophyll
HNO_3	Nitric acid
HPLE	High productivity low export
k_z	Diffusivity constant
LCDW	Lower circumpolar deep water
MADT	Mean absolute dynamic topography
MLD	Mixed layer depth
n	Number of observations
NADW	North Atlantic deep water
NO_3^-	Nitrate
NPF	North of the Polar Front
O_2	Oxygen
OC-CCI	Ocean Colour Climate Change Initiative
P	Phosphorus
pAl	Particulate aluminium
PAR	Photosynthetically active radiation
pBa	Particulate barium

PF	Polar Front
pFe	Particulate iron
PFZ	Polar frontal zone
PO_4^{3-}	Phosphate
POC	Particulate organic carbon
PP	Primary productivity
SACCf	Southern Antarctic circumpolar front
SAF	Subantarctic front
SAMW	Subantarctic mode water
SASW	Subantarctic surface water
SAZ	Subantarctic zone
Sbdy	Southern boundary
SD	Standard deviation
SF-ICP-MS	Sector field inductively coupled mass spectrometry
Si	Silicon
$Si(OH)_4$	Silicic acid
SICW	South Indian central water
SIO	Southern Indian Ocean
SO	Southern Ocean
SPF	South of the Polar Front
STF	Subtropical front
STSW	Subtropical surface water
STZ	Subtropical zone
SWIR	Southwest Indian ridge
T-S	Temperature-Salinity
TCO_2	Total dissolved carbon dioxide
UCC	Upper continental crust
UCDW	Upper circumpolar deep water
θ	Potential temperature
σ_θ	Potential density

Chapter 1: Introduction

1.1 The global significance of the Southern Ocean biological carbon pump

When viewing the global ocean (Figure 1.1) as a unified body of water, the central significance of the Southern Ocean (SO) and the Antarctic Circumpolar Current (ACC) becomes obvious, connecting the Atlantic, Pacific and Indian ocean basins. Large quantities of heat, carbon and nutrients are transported between the ocean basins via the thermohaline circulation (Figure 1.1; Meredith, 2019). The SO is also the point at which old, deep waters outcrop and interact with the atmosphere, exchanging heat and carbon, before once again being subducted into the interior ocean as intermediate and deep waters. As a result, the SO is crucial to the Earth's climate, present and future (Akhoudas et al., 2021; Meredith, 2019; Pope et al., 2017; Rintoul et al., 2012).

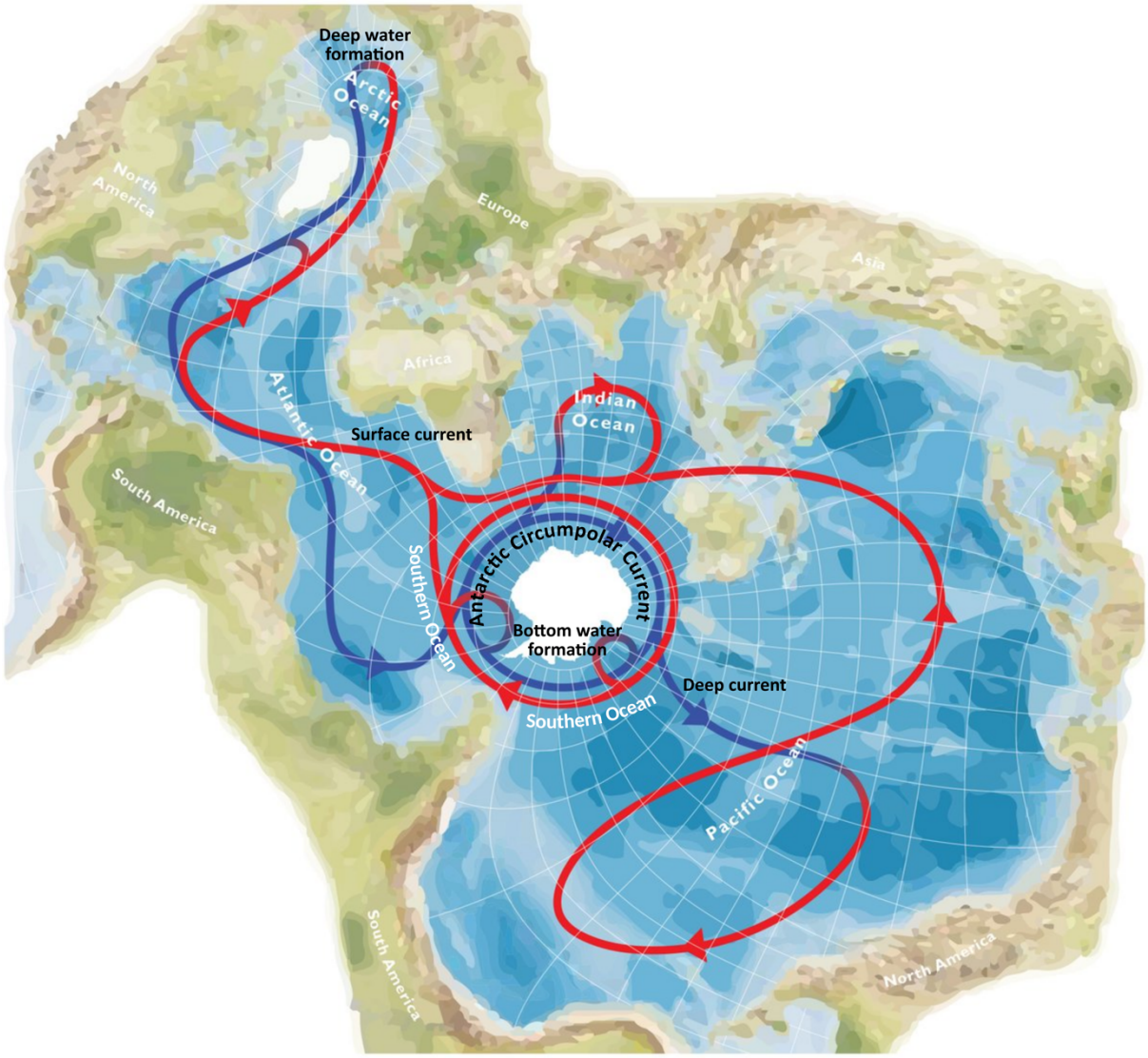

Figure 1.1: A spilhaus projection of the global ocean, viewed as a unified body, linked by the ACC via thermohaline circulation (simplified) shown with surface water flow in red and deep water flow in blue (Modified from Meredith, 2019).

Inorganic carbon is taken up by the ocean through two pathways, the solubility pump which is governed by physical properties, temperature and salinity, and the biological carbon pump (BCP) which is governed by the biological uptake of carbon by phytoplankton in surface waters, through photosynthesis. Near surface (10 m) total dissolved carbon dioxide (TCO_2) concentrations in the SO (Figure 1.2) indicate the significance of the SO as a carbon sink and source (Gottschalk et al., 2016; Goyet et la., 2000). Atmospheric pulses in carbon dioxide (CO_2) during glacial and interglacial periods have been linked to decreases in the biological export of C and increases in deep ocean ventilation via SO water masses, thereby linking the

SO's BCP to atmospheric CO_2 and the climate, through the synergy of physical and biological processes (Gottschalk et al., 2016). The SO BCP is, however, inefficient due to widespread iron (Fe) limitation (Martin, 1990; Martin et al., 1990; Moore et al., 2001). Indeed, Fe is an essential micronutrient required by phytoplankton for metabolic processes such as photosynthesis, nitrate assimilation and respiration, and although SO phytoplankton species have adapted to the extreme conditions of their environment, at sub-nanomolar concentrations the availability of Fe for production in surface waters has a substantial control over the BCP, in combination with environmental factors such as light and temperature, which in turn influences atmospheric CO_2 drawdown (Martin et al., 1990, Strzepek et al., 2012; 2019). The areas within the SO where Fe limitation predominates, are termed High-Nutrient-Low-Chlorophyll (HNLC) regions, which are characterized by large amounts of unused macronutrients accompanied by sub-nanomolar Fe concentrations.

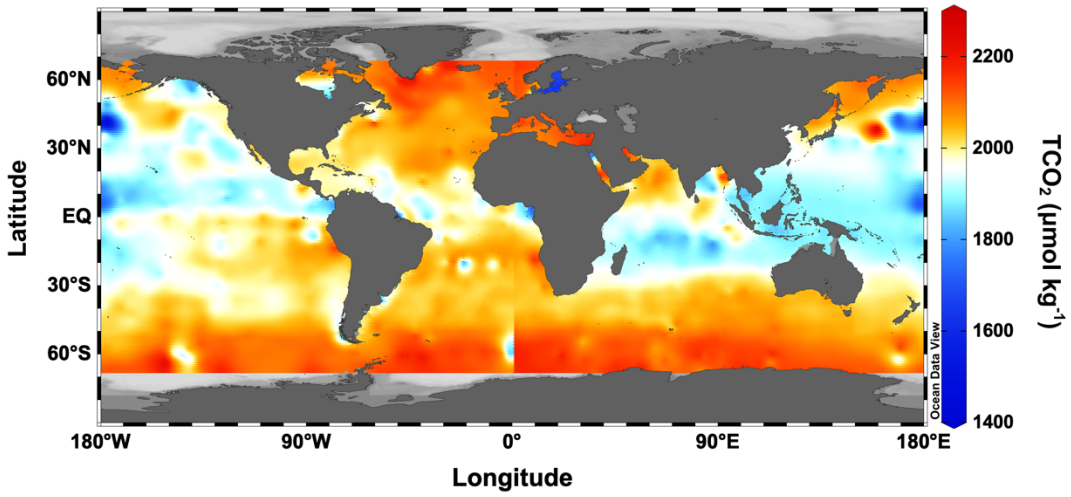

Figure 1.2: Global annual mean, near sea surface (10 m) total dissolved carbon dioxide (TCO_2) estimates from the Carbon Dioxide Information Analysis Center (Goyet et al., 2000).

1.2 The marine Fe biogeochemical cycle

The marine Fe biogeochemical cycle (Figure 1.3) is complex and encompasses multiple sources, sinks, and processes which affect the distribution of the different physical and chemical species of Fe within the marine environment, which remain poorly quantified. This biologically essential micronutrient is present throughout the water column, originating from

external sources such as atmospheric inputs, continental margins, sedimentary resuspension, hydrothermal vents and sea ice melt, supplying both lithogenic and biogenic forms of new Fe (Tagliabue et al., 2017). Processes such as photoreduction, excess ligand production, dissolution and remineralisation influence the partitioning of Fe, to varying degrees, between the different size fractions; namely, the dissolved (< 0.2 μm) fraction which is made up of the soluble (< 0.02 μm) and colloidal (0.02 - 0.2 μm) fractions, and the particulate (> 0.45 μm) fraction (Cutter et al., 2017). Inorganic Fe(III) is the most abundant form of Fe and is also highly insoluble in the marine environment, Fe(II) is readily oxidised to Fe(III), due to oxic conditions, causing Fe to precipitate into sinking particles (Golderg, 1954). Organic Fe-binding ligands, which are biologically produced by phytoplankton, bacteria, viruses, and remineralisation throughout the water column, bind to Fe keeping the Fe in a soluble phase, increasing the residence time of Fe in the mixed layer where it is accessible to phytoplankton and can be transported laterally to adjacent water masses (Völker and Tagliabue, 2015; Tagliabue et al., 2017). The particulate fraction is also an important part of the Fe cycle which can influence the interactions of the dissolved phase. Adsorption of Fe on particles would be responsible for the removal of dissolved Fe (dFe) through scavenging (Thuróczy et al., 2010). Biological uptake, aggregate formation, vertical export, and scavenging are sinks which remove Fe from surface waters down into the interior and deep ocean. Beyond the sources, sinks and internal cycling of Fe, physical transport mechanisms such as lateral and vertical advection, entrainment and vertical diffusion redistribute Fe throughout the global ocean. These processes can act as sources or sinks of Fe to surface and intermediate waters, where Fe availability is crucial to the functioning of the BCP (Boyd and Ellwood, 2010; Tagliabue et al., 2017).

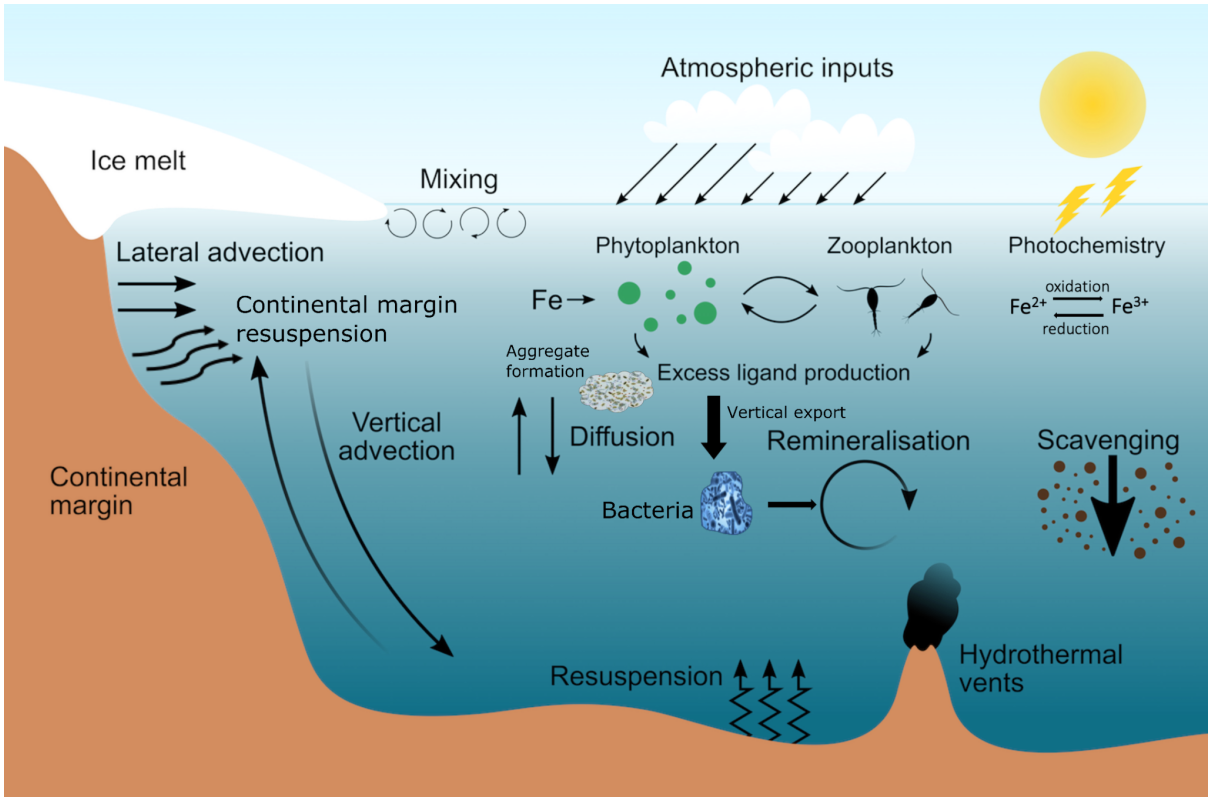

Figure 1.3: A schematic diagram of the major sources, sinks and processes which affect the distribution of Fe in the SO. Sources include atmospheric inputs (e.g., dust), continental margin resuspension, sediment resuspension, sea ice and hydrothermal inputs. Surface water mixing, vertical and lateral advection, and diffusion are physical processes which transport Fe throughout the water column. Photochemical oxidation and reduction of Fe, excess ligand production, biological uptake, aggregate formation, vertical export, bacterial mediated remineralisation, and scavenging are internal processes which drive the physical and chemical speciation of Fe throughout the water column (Created by Dr Llopis Monferrer).

Many questions still exist surrounding the interactions between Fe species and how these interactions affect speciation and distribution of Fe, now and in future oceans (Tagliabue and Völker, 2011). New dFe supply to surface waters of the SO remains low due to low external inputs and the complex matrix of processes controlling the internal cycling of Fe in the ocean interior is hypothesised to be the dominant control on the distribution of dFe throughout large regions of the SO (Boyd and Ellwood, 2010; Boyd et al., 2010; 2017; Tagliabue et al., 2014; 2019). It is predicted that changes brought about by climate change will alter numerous environmental factors which control the distribution of Fe in the global ocean and to understand and predict these changes, a comprehensive understanding of spatio-temporal variability of the current marine Fe cycle must be acquired (Hutchins and Boyd, 2016; Pope et al., 2017;

Tagliabue and Völker, 2011). The relative importance of sources, sinks, and processes on SO Fe biogeochemistry is also assumed to be affected by seasonality (Tagliabue et al., 2014).

1.3 The seasonal cycle of dFe in the SO

Seasonality is an important component which is not present in current models due to the absence of winter observations (Tagliabue et al., 2014, 2017). In high latitude regions like the SO, substantial seasonal changes in environmental variables such as temperature and irradiance, make seasonal variability a crucial component (Tagliabue and Arrigo, 2006) that also affects the seasonality of primary productivity (PP) (Tagliabue and Völker, 2011). The inclusion of this component is invaluable and may improve the accuracy of these models substantially.

Hypothesised seasonal changes in dFe supply pathways to the surface mixed layer proposes that winter entrainment accesses the subsurface dFe winter reservoir, thereby supplying the required dFe for bloom initiation during austral spring (Figure 1.4; Tagliabue et al., 2014). As the spring bloom is initiated a reduction in the surface dFe stock occurs due to detrainment and biological uptake. As the season progresses the surface dFe stock is depleted and the bloom Fe requirements are primarily sustained through diapycnal diffusion and increased remineralisation in surface waters (Tagliabue et al., 2014). The replenishment of the subsurface dFe winter reservoir would therefore be crucial for the resupply of dFe into surface waters during the following spring bloom initiation. It is believed that the winter reservoir is primarily replenished through remineralised Fe in the open waters of the SO (Boyd et al., 2017; Tagliabue et al., 2014; 2019). However, there is currently not enough data available to determine the relative importance of remineralisation during winter.

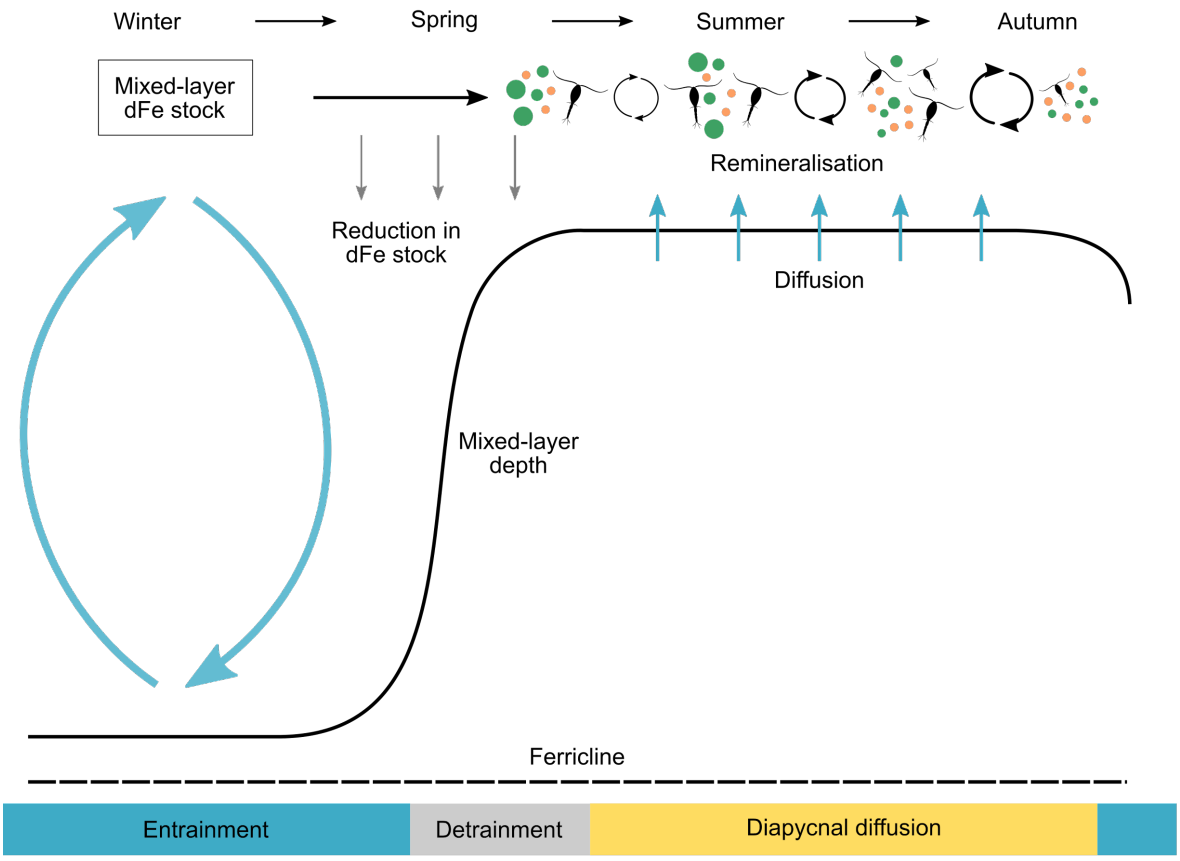

Figure 1.4: A schematic diagram, adapted from Tagliabue et al. (2014), depicting the hypothesis of seasonal changes in the physical dFe supply pathways into the surface mixed layer. As the bloom season progresses, the magnitude of remineralisation increases and changes in the pelagic community composition, to smaller cells, occur. The dominant physical processes across seasons are shown at the bottom of the figure, where winter entrainment is the dominant supply term in winter, increasing dFe surface stocks. Detrainment then decreases surface dFe during spring after which diapycnal diffusion and surface remineralisation take over as the dominant supply mechanisms to sustain surface mixed layer dFe stocks.

1.4 Observational gaps in dFe measurements in the SO

The SO is the least sampled oceanic region due to the vast size and inaccessibility during certain months of the year, especially winter, when strong winds, rough seas, and the expansion of sea ice make ship-based observations in the SO extremely challenging (Meredith, 2019). Although large strides have been made with regard to autonomous sampling, many of the measurements we need, specifically Fe measurements, cannot yet be made using these techniques, making data collected from the SO, especially in winter, of uniquely high value (Meredith, 2019). The spatial and temporal distribution of dFe observations in the open waters of the SO (Figure 1.5) make it clear that significant observational gaps remain in this region. Spatially, measurements

are concentrated in the Atlantic basin and the Australian sector of the SO and temporally, observations have been focused on spring and summer months. In order to better constrain the internal cycling of Fe in the SO and how environmental changes will affect this, it is pertinent that seasonal and spatial changes in this vast and dynamic oceanic region is understood.

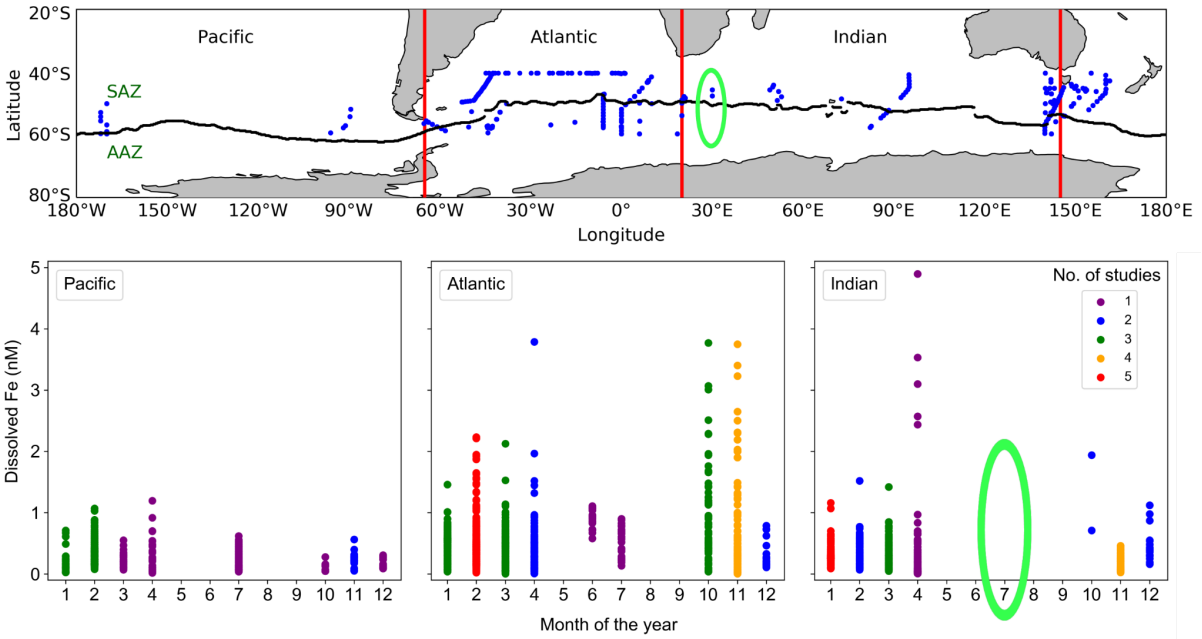

Figure 1.5: A compilation of SO open ocean dFe observations, obtained from Tagliabue et al. (2012), Schlitzer et al. (2018; GEOTRACES IDP2017), Grand et al. (2015), and Mtshali et al. (2019) are displayed as positions (blue) on a cylindrical equal-area projection of the SO, with the three basin cut offs indicated by the red lines, from left to right, Pacific, Atlantic and Indian, and the black line is the mean northern branch of the PF (Tagliabue et al., 2012), acting as the cut off between the SAZ and the AZ (top panel). Using the same compilation data, the plots on the bottom panel indicate the monthly frequency of dFe observations within each SO basin. Green circles indicate the spatial and temporal gaps to be addressed during this study.

1.5 The significance of remineralisation for dFe distributions in the SO

In the open waters of the SO external sources of Fe are relatively low, making internal cycling a dominant process in driving the availability of dFe (Tagliabue et al., 2019). This process has, however, not yet been sufficiently characterised to fully understand the effects of environmental variables on the distribution and speciation of Fe, and the consequences thereof on PP (Tagliabue et al., 2019). Despite progress made in understanding the Fe cycle regarding sources, remineralisation and factors influencing remineralisation (Boyd and Ellwood, 2010; Boyd et al., 2017), a lot is still unknown regarding net remineralisation in intermediate waters, on temporal and spatial scales (Tagliabue et al., 2019). Estimates of Fe remineralisation have

revealed that only 2 - 8% of the non-lithogenic particulate Fe (pFe) from the upper ocean is accounted for in intermediate water remineralised dFe observations (Tagliabue et al., 2019). Hypotheses explaining the low percentages of remineralised dFe in intermediate waters, compared to the phytoplankton and pFe stocks are that the biogenic pFe is not exported from surface waters and is instead recycled in the waters above intermediate waters. The second hypothesis is that biogenic pFe is exported but not remineralised and the third hypothesis is that Fe is exported and remineralised but is largely removed by scavenging, thereby resulting in much lower intermediate water remineralised dFe than what is expected (Tagliabue et al., 2019).

Multiple studies have proved that although Fe is significantly recycled in surface waters, there is still substantial surface export (Tagliabue et al., 2014; Boyd et al., 2017; 2015; Strzepek et al., 2005; Boyd et al., 2012), debunking the first hypothesis. The second hypothesis can also be rejected based on the outcomes of field experiments that have assessed the dissolution of Fe below the mixed layer (Boyd et al., 2010) and subsurface dFe remineralisation rates (Ellwood et al., 2014), where the dissolution of Fe from particles just below the mixed layer was found to range from 120 - 1314 nmol m^{-3} yr^{-1} (Ellwood et al., 2014; Boyd et al., 2010; Velasquez et al., 2016). Based on these estimates of dissolution, dFe removal rates of ~ 0.4 - 10 µmol m^{-2} d^{-1} (Frew et al., 2006; Ellwood et al., 2014; Tagliabue et al., 2019) are required when taking into consideration the estimated accumulation rate of dFe ~ 2 nmol m^{-3} yr^{-1} in intermediate waters (Tagliabue et al., 2019). Leaving us with the third hypothesis, that a significant loss of dFe occurs via scavenging onto particles in intermediate waters (Figure 1.6; Boyd and Ellwood, 2010; Thuróczy et al., 2010; Twining et al., 2014).

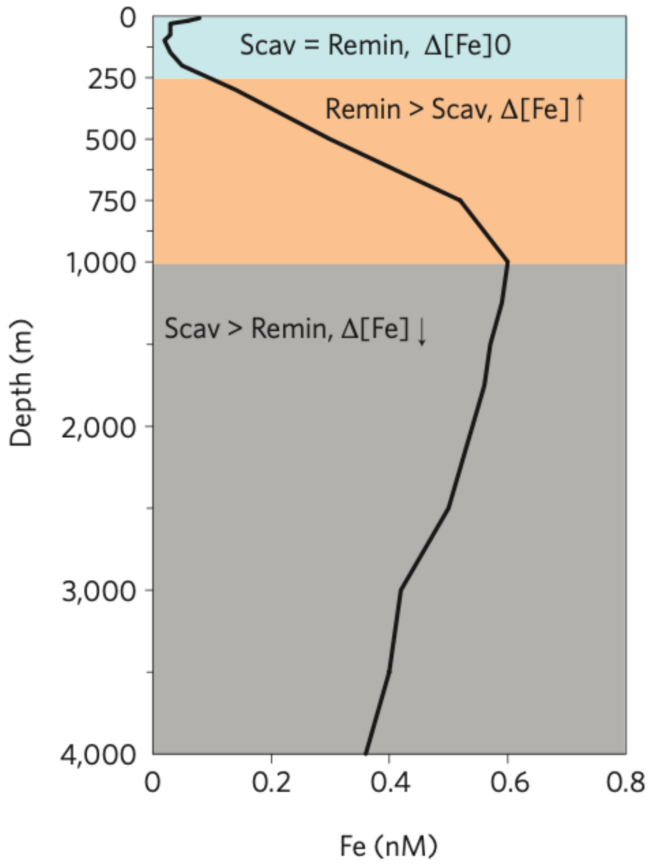

Figure 1.6: A typical dFe profile, indicating the relative influence of scavenging (Scav) versus remineralisation (Remin). Δ[Fe] indicates the change in dFe concentration (Boyd and Ellwood, 2010).

1.6 Surface export and mesopelagic remineralisation

Surface export and the subsequent remineralisation of particles in the mesopelagic zone is vital for the replenishment of the subsurface dFe reservoir (Tagliabue et al., 2014; 2019). Although the mesopelagic layer is clearly of substantial importance, it is still largely under-studied, especially in the high latitudes, and therefore processes occurring in this section of the water column are poorly constrained, despite their importance to global elemental cycles, including that of carbon and Fe (Le Moigne, 2019; Robinson et al., 2010).

A variety of interlinked processes and environmental factors affect mesopelagic remineralisation (Boyd et al., 2017). The efficiency of remineralisation is influenced by the size and composition of exported particles (Rosengard et al., 2015; Twining et al., 2014) as well as the surface export pathway of these particles (Boyd et al., 2019; Le Moigne, 2019),

creating an intricate web of variables to disentangle. Nutrient limitation in surface mixed layer waters tends to limit export and consequently mesopelagic remineralisation, by creating a shift to smaller phytoplankton assemblages which preferentially survive on recycled nutrients in these surface waters (Planchon et al., 2013). Temperature is also a control on mesopelagic remineralisation, especially in high latitude waters, due to temperature-dependent heterotrophs that facilitate remineralisation (DeVries and Weber, 2017; Marsay et al., 2015).

When taking into consideration all the factors influencing remineralisation and how important this process is to the distribution of nutrients in the global ocean, it becomes clear that a stronger understanding needs to be gained with regard to all these variables. In order to better estimate net remineralisation in the SO and how this affects the BCP, apparent oxygen utilisation (AOU) and barium excess (Ba_{xs}) are two proxies that have been successfully used to assess remineralisation within the mesopelagic zone (Ito and Follows, 2005; Dehairs et al., 1997; Lemaitre et al., 2018).

1.7 Apparent oxygen utilisation remineralisation proxy

AOU is an estimation of oxygen (O_2) consumed by the remineralisation of biogenic particles in the ocean interior, relative to surface saturation, when surface water masses are subducted below the surface mixed layer (Figure 1.7). Generally, O_2 is increasingly depleted as the subducted water mass accumulates remineralised nutrients. Assuming O_2 is saturated in surface waters, estimates of how much O_2 is consumed by remineralisation can be made, which is determined using in situ salinity, temperature and O_2 observations. The AOU proxy assumes that nutrient concentrations in intermediate waters are made up of a "preformed" and a "remineralised" component $[N] = [N_{preformed}] + [N_{remineralised}]$ (Ito and Follows, 2005). When intermediate waters are formed in high latitude waters, unutilized nutrients are transported into the interior ocean, this component of the nutrient concentration is the "preformed" nutrients and the nutrients released in the ocean interior due to remineralisation is the "remineralised"

component. The "remineralised" nutrient concentration can be estimated using AOU which integrates remineralisation concentrations over timescales of years to decades (Ito et al., 2004). This proxy is the classical remineralisation proxy and has been used successfully throughout the global ocean, to assess remineralisation.

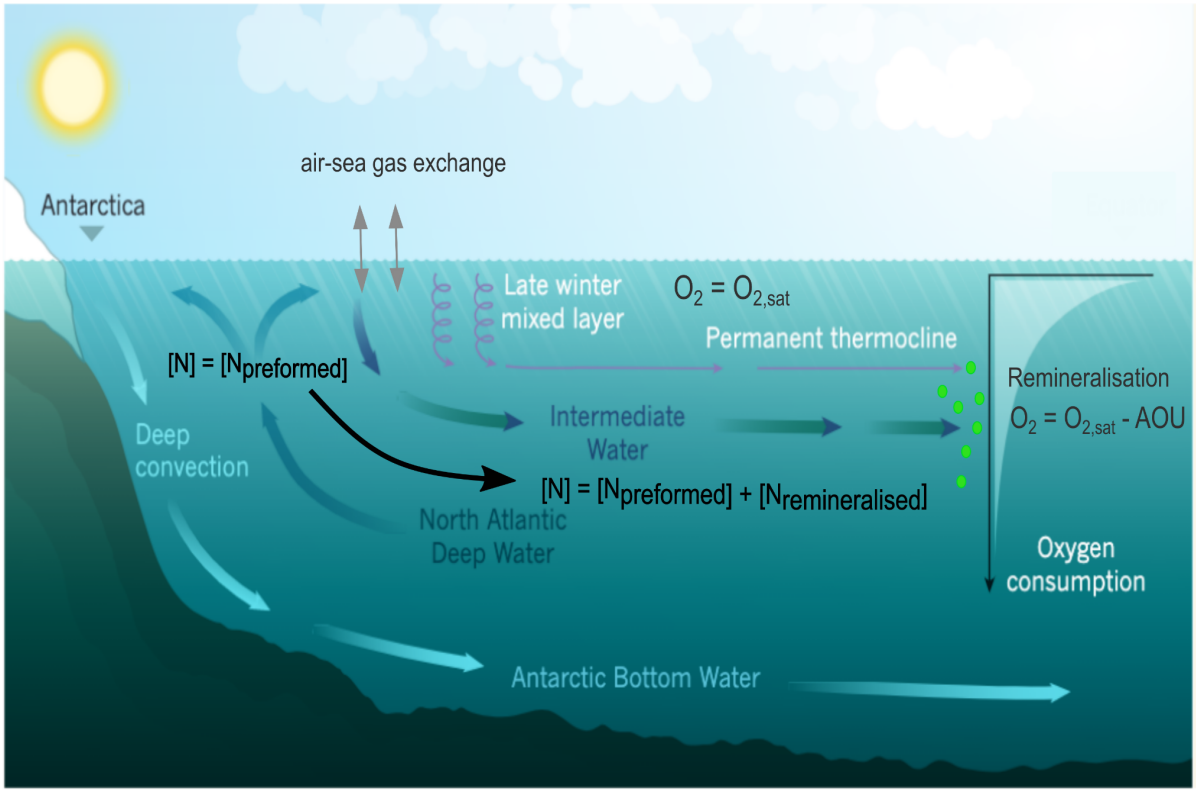

Figure 1.7: A schematic diagram depicting the main processes affecting dissolved O_2 distribution in the SO. Deep convection and the formation of Antarctic Intermediate Water transports O_2-rich surface waters into the deep and interior ocean, respectively. O_2 is removed from subducted surface waters, relative to surface saturation ($_{O2,sat}$), due to biological consumption (AOU). Preformed nutrients ([$N_{preformed}$]) are subducted into the interior ocean. As remineralisation takes up O_2, the observed nutrient concentration ([N]) is made up of [$N_{preformed}$] + remineralised nutrients ([$N_{remineralised}$]), in intermediate waters (modified from Gilbert, 2017).

1.8 Barium excess remineralisation proxy

The Ba_{xs} proxy is used to estimate mesopelagic POC remineralisation fluxes, defined as the "biogenic" portion of particulate barium (pBa) in the form of barite crystals, formed within decaying bio-aggregates at the base of the surface mixed layer as biogenic particles are exported out of the surface mixed layer (Figure 1.8; Bishop, 1988; Dehairs et al., 1997; Lam and Bishop, 2007; Legeleux and Reyss, 1996; van Beek et al., 2007). The Ba_{xs} peak observed

in the mesopelagic zone is due to the release of the barite crystals and has been correlated to primary production, O_2 consumption and POC remineralisation (Dehairs et al., 1997).

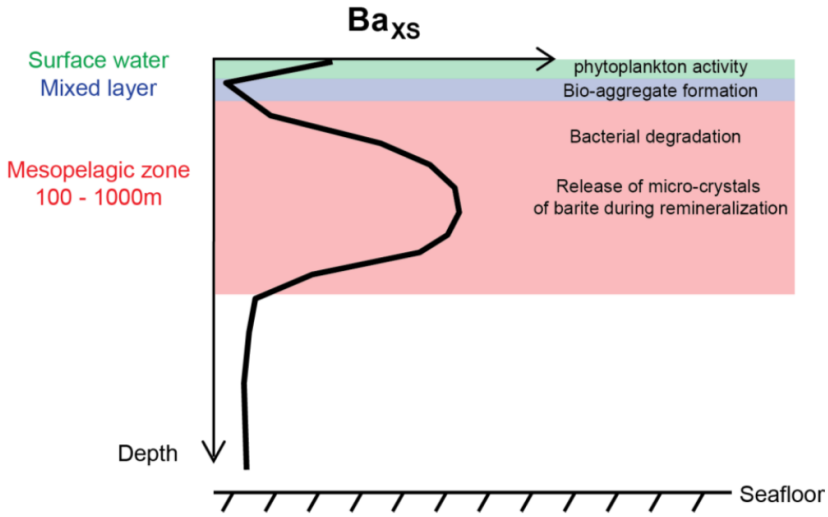

Figure 1.8: A typical marine Baxs profile during spring and summer. Adsorption of Ba onto biogenic particles in high productivity waters give high concentrations of Baxs. A minimum at the MLD, where bioaggregates are formed, creating the environment in which barite crystals are formed. The release of these barite crystals creates a Baxs peak in the mesopelagic zone, as a consequence of remineralisation (Lemaitre, 2017, thesis).

1.9 Objectives of this study

As part of a GEOTRACES process study (GIpr07) of a transect along 30°E in the open waters of the western Southern Indian Ocean (SIO, 58.5°S to 41.0°S), the objectives of this study were formulated.

- Firstly, it was sought to address observational gaps in dFe measurements, identified in the western SIO and during austral winter (Figure 1.5), and how these distributions compared to observations throughout the SO, spatially and temporally
- To assess the controls of winter dFe distributions in the study region, season cycle of these controls and how these factors influence the supply of dFe to the surface mixed layer.
- To gain insight into Ba_{xs} distributions during austral winter and the timescale of this remineralisation proxy.
- To assess the link between mesopelagic Ba_{xs} and integrated remotely sensed PP, on a basin scale.

- Finally, to utilise remineralisation proxies, AOU and Ba_{xs}, to assess remineralisation of dFe in the intermediate waters of the SIO for the replenishment of the subsurface winter reservoir.

In this context, distributions of dFe and Ba_{xs} were measured during early austral winter (July 2017) along the 30°E line, in conjunction with ancillary measurements to assess controls on distributions, internal cycling and supply mechanisms. Compilation datasets were constructed of available dFe and Ba_{xs} data throughout the SO to facilitate comparisons with measurements from this study. To evaluate the link between Ba_{xs} and PP, on a basin scale, all available data was assessed against integrated remotely sensed PP.

To our knowledge there are currently only two published winter dFe studies in the SO one in the Atlantic basin (Mtshali et al., 2019) and another in the Pacific basin (Ellwood et al., 2008), and none for Ba_{xs} during winter. This study will contribute to the emerging understanding of winter trace metal distributions and internal cycling in the SO, giving insight into the replenishment of the winter dFe reservoir, as well as obtaining better estimates of export and remineralisation on annual and basin scales.

1.10 Thesis structure

This thesis is made up of four chapters, one of which is a paper that has been submitted and is currently under review (Chapter 3, van Horsten et al., In review) in Biogeosciences. Chapters 2 and 3 both present data from a winter study conducted in the SIO as part of the GEOTRACES process study (GIpr07).

In Chapter 2 the first reported winter dFe observations in the SIO is presented. A compilation dataset of dFe measurements is also presented, looking at inter- and intra-basins, and seasonal comparisons in the open waters of the SO. Fluxes of dFe into the surface mixed layer are estimated, using the winter distributions from this study, and compared to previously published values, assessing the seasonality and spatial variation of supply mechanisms. Utilising the

AOU remineralisation proxy, an assessment of intermediate water internal cycling was conducted, to determine the significance of Fe remineralisation and how this supports the replenishment of the subsurface winter reservoir.

Chapter 3 is focused on the Ba_{xs} remineralisation proxy, presenting the first distributions during austral winter. The timescale of this proxy is proposed to be longer than previously reported, up to an annual timescale instead of weeks. A SO compilation dataset of Ba_{xs} observations is used to assess the annual accumulation of Ba_{xs} in the mesopelagic zone. The compilation dataset is also used to link mesopelagic Ba_{xs} stock to integrated remotely sensed PP, assessing the timescale of this proxy, and surface export and POC remineralisation fluxes on annual and basin scales.

Chapter 4 is the overarching discussion, conclusions and perspectives, linking the outcomes of Chapters 2 and 3, how these outcomes fit into the current knowledge of the marine dFe biogeochemical cycle and how this research will benefit going forward.

There are three appendices attached to the manuscript. Appendix A contains the supplementary data and figures linked to Chapter 2. Appendix B contains all supplementary data and figures linked to Chapter 3. Appendix C contains all ancillary data, such as physical parameters and macronutrient data used across both Chapters 2 and 3.

References

Akhoudas, C. H., Sallée, J. B., Haumann, F. A., Meredith, M. P., Garabato, A. N., Reverdin, G., Jullion, L., Aloisi, G., Benetti, M., Leng, M. J., & Arrowsmith, C. (2021). Ventilation of the abyss in the Atlantic sector of the Southern Ocean. *Scientific Reports*, *11*(1), 1–13. https://doi.org/10.1038/s41598-021-86043-2

Bishop, J. K. B. (1988). The barite-opal-organic carbon association in oceanic particulate matter. In *Nature* (Vol. 332, Issue 6162, pp. 341–343). https://doi.org/10.1038/332341a0

Boyd, P. W., Ibisanmi, E., Sander, S. G., Hunter, K. A., & Jackson, G. A. (2010). Remineralization of upper ocean particles: Implications for iron biogeochemistry. *Limnology and Oceanography*, *55*(3), 1271–1288. https://doi.org/10.4319/lo.2010.55.3.1271

Boyd, P. W., Arrigo, K. R., Strzepek, R., & Van Dijken, G. L. (2012). Mapping phytoplankton iron utilization: Insights into Southern Ocean supply mechanisms. *Journal of Geophysical Research: Oceans*, *117*(6), 1–18. https://doi.org/10.1029/2011JC007726

Boyd, P. W., Strzepek, R. F., Ellwood, M. J., Hutchins, D. A., Nodder, S. D., Twining, B. S., & Wilhelm, S. W. (2015). Why are biotic iron pools uniform across high- and low-iron pelagic ecosystems? *Global Biogeochemical Cycles*, *29*(7), 1028–1043. https://doi.org/10.1002/2014GB005014

Boyd, P. W., Ellwood, M. J., Tagliabue, A., & Twining, B. S. (2017). Biotic and abiotic retention, recycling and remineralization of metals in the ocean. *Nature Geoscience*, *10*(3), 167–173. https://doi.org/10.1038/ngeo2876

Boyd, P. W., Claustre, H., Levy, M., Siegel, D. A., & Weber, T. (2019). Multi-faceted particle pumps drive carbon sequestration in the ocean. In *Nature* (Vol. 568, Issue 7752, pp. 327–335). https://doi.org/10.1038/s41586-019-1098-2

Boyd, P. W., & Ellwood, M. J. (2010). The biogeochemical cycle of iron in the ocean. *Nature Geoscience*, *3*(10), 675–682. https://doi.org/10.1038/ngeo964

Cutter, G., Casciotti, K., Croot, P., Geibert, W., Heimbürger, L.-E., Lohan, M., Planquette, H., & van de Flierdt, T. (2017). *Sampling and Sample-handling Protocols for GEOTRACES Cruises. Version 3, August 2017.* (Issue August). http://www.geotraces.org/images/stories/documents/intercalibration/Cookbook.pdf

Dehairs, F., Shopova, D., Ober, S., Veth, C., & Goeyens, L. (1997). Particulate barium stocks and oxygen consumption in the Southern Ocean mesopelagic water column during spring and early summer: Relationship with export production. *Deep-Sea Research Part II: Topical Studies in Oceanography*, *44*(1–2), 497–516. https://doi.org/10.1016/S0967-0645(96)00072-0

DeVries, T., & Weber, T. (2017). The export and fate of organic matter in the ocean: New constraints from combining satellite and oceanographic tracer observations. *Global Biogeochemical Cycles*, *31*(3), 535–555. https://doi.org/10.1002/2016GB005551

Ellwood, M. J., Boyd, P. W., & Sutton, P. (2008). Winter-time dissolved iron and nutrient distributions in the Subantarctic Zone from 40-52S; 155-160E. *Geophysical Research Letters*, *35*(11), 2–7. https://doi.org/10.1029/2008GL033699

Ellwood, M. J., Nodder, S. D., King, A. L., Hutchins, D. A., Wilhelm, S. W., & Boyd, P. W. (2014). Pelagic iron cycling during the subtropical spring bloom, east of New Zealand. *Marine Chemistry*, *160*, 18–33. https://doi.org/10.1016/j.marchem.2014.01.004

Frew, R. D., Hutchins, D. A., Nodder, S., Sanudo-Wilhelmy, S., Tovar-Sanchez, A., Leblanc, K., Hare, C. E., & Boyd, P. W. (2006). Particulate iron dynamics during FeCycle in subantarctic waters southeast of New Zealand. *Global Biogeochemical Cycles*, *20*(1), 1–15. https://doi.org/10.1029/2005GB002558

Gilbert, D. (2017). Oceans lose oxygen. In *Nature* (Vol. 542, Issue 7641, pp. 303–304). Nature Publishing Group. https://doi.org/10.1038/542303a

Goldberg, E. D. (1954). Marine Geochemistry 1. Chemical Scavengers of the Sea. *The Journal of Geology*, *62*(3), 249–265. https://doi.org/10.1086/626161

Gottschalk, J., Skinner, L. C., Lippold, J., Vogel, H., Frank, N., Jaccard, S. L., & Waelbroeck, C. (2016). Biological and physical controls in the Southern Ocean on past millennial-scale atmospheric CO2 changes. *Nature Communications*, *7*(May). https://doi.org/10.1038/ncomms11539

Goyet, C., Healy, R. J., & Ryan, J. P. (2000). Global distribution of total inorganic carbon and total alkalinity below the deepest winter mixed layer depths, CDIAC/NDP-076. In *Global distribution of total inorganic carbon and total alkalinity below the deepest winter mixed layer depths, CDIAC/NDP-076*. https://doi.org/10.2172/760546

Grand, M. M., Measures, C. I., Hatta, M., Morton, P. L., Barrett, P., Milne, A., Resing, J. A., & Landing, W. M. (2015). The impact of circulation and dust deposition in controlling the distributions of dissolved Fe and Al in the south Indian subtropical gyre. *Marine Chemistry*, *176*, 110–125. https://doi.org/10.1016/j.marchem.2015.08.002

Hutchins, D. A., & Boyd, P. W. (2016). Marine phytoplankton and the changing ocean iron cycle. *Nature Climate Change*, *6*(12), 1072–1079. https://doi.org/10.1038/nclimate3147

Ito, T., Follows, M. J., & Boyle, E. A. (2004). Is AOU a good measure of respiration in the oceans? *Geophysical Research Letters*, *31*(17), 1–4. https://doi.org/10.1029/2004GL020900

Ito, T., & Follows, M. J. (2005). Preformed phosphate, soft tissue pump and atmospheric CO2. *Journal of Marine Research*, *63*(4), 813–839. https://doi.org/10.1357/0022240054663231

Lam, P. J., & Bishop, J. K. B. (2007). High biomass, low export regimes in the Southern Ocean. *Deep-Sea Research Part II: Topical Studies in Oceanography*, *54*(5–7), 601–638. https://doi.org/10.1016/j.dsr2.2007.01.013

Le Moigne, F. A. C. (2019). Pathways of Organic Carbon Downward Transport by the Oceanic Biological Carbon Pump. In *Frontiers in Marine Science* (Vol. 6). https://doi.org/10.3389/fmars.2019.00634

Legeleux, F., & Reyss, J. L. (1996). 228Ra/226Ra activity ratio in oceanic settling particles: Implications regarding the use of barium as a proxy for paleoproductivity

reconstruction. *Deep-Sea Research Part I: Oceanographic Research Papers*, *43*(11–12), 1857–1863. https://doi.org/10.1016/S0967-0637(96)00086-6

Lemaitre, N., Planquette, H., Planchon, F., Sarthou, G., Jacquet, S., García-Ibáñez, M. I., Gourain, A., Cheize, M., Monin, L., André, L., Laha, P., Terryn, H., & Dehairs, F. (2018). Particulate barium tracing of significant mesopelagic carbon remineralisation in the North Atlantic. *Biogeosciences*, *15*(8), 2289–2307. https://doi.org/10.5194/bg-15-2289-2018

Lemaitre, N. (2017). *Multi-proxy approach (234Th, Baxs) of export and remineralization fluxes of carbon and biogenic elements associated with the oceanic biological pump*. UNIVERSITÉ DE BRETAGNE OCCIDENTALE.

Marsay, C. M., Sanders, R. J., Henson, S. A., Pabortsava, K., Achterberg, E. P., & Lampitt, R. S. (2015). Attenuation of sinking particulate organic carbon flux through the mesopelagic ocean. *Proceedings of the National Academy of Sciences of the United States of America*, *112*(4), 1089–1094. https://doi.org/10.1073/pnas.1415311112

Martin, J. H. (1990). Glacial-Interglacial CO2 change: the iron hypothesis. *Paleoceanography*, *5*(1), 1–13.

Martin, J. H., Fitzwater, S. E., & Gordon, R. M. (1990). Iron deficiency limits phytoplankton growth in Antarctic waters. *Global Biogeochemical Cycles*, *4*(1), 5–12. https://doi.org/10.1029/GB004i001p00005

Meredith, M. (2019, June). The global importance of the Southern Ocean and the key role of its freshwater cycle. *Ocean Challenge*, *23*.

Moore, J. K., Doney, S. C., Glover, D. M., & Fung, I. Y. (2001). Iron cycling and nutrient-limitation patterns in surface waters of the world ocean. *Deep-Sea Research Part II: Topical Studies in Oceanography*, *49*(1–3), 463–507. https://doi.org/10.1016/S0967-0645(01)00109-6

Mtshali, T. N., van Horsten, N. R., Thomalla, S. J., Ryan-Keogh, T. J., Nicholson, S. A., Roychoudhury, A. N., Bucciarelli, E., Sarthou, G., Tagliabue, A., & Monteiro, P. M. S. (2019). Seasonal Depletion of the Dissolved Iron Reservoirs in the Sub-Antarctic Zone of the Southern Atlantic Ocean. *Geophysical Research Letters*, *46*(8), 4386–4395. https://doi.org/10.1029/2018GL081355

Parekh, P., Follows, M. J., & Boyle, E. A. (2005). Decoupling of iron and phosphate in the global ocean. *Global Biogeochemical Cycles*, *19*(2), 1–16. https://doi.org/10.1029/2004GB002280

Planchon, F., Cavagna, A. J., Cardinal, D., André, L., & Dehairs, F. (2013). Late summer particulate organic carbon export and twilight zone remineralisation in the Atlantic sector of the Southern Ocean. *Biogeosciences*, *10*(2), 803–820. https://doi.org/10.5194/bg-10-803-2013

Pope, A., Wagner, P., Johnson, R., Shutler, J. D., Baeseman, J., & Newman, L. (2017). Community review of Southern Ocean satellite data needs. *Antarctic Science*, *29*(2), 97–138. https://doi.org/10.1017/S0954102016000390

Rintoul, S. R., Meredith, M. P., Schofield, O., & Newman, L. (2012). The Southern Ocean observing system. *Oceanography*, *25*(3), 68–69. https://doi.org/10.5670/oceanog.2012.76

Robinson, C., Steinberg, D. K., Anderson, T. R., Arístegui, J., Carlson, C. A., Frost, J. R., Ghiglione, J. F., Hernández-León, S., Jackson, G. A., Koppelmann, R., Quéguiner, B., Ragueneau, O., Rassoulzadegan, F., Robison, B. H., Tamburini, C., Tanaka, T., Wishner, K. F., & Zhang, J. (2010). Mesopelagic zone ecology and biogeochemistry - A synthesis. *Deep-Sea Research Part II: Topical Studies in Oceanography*, *57*(16), 1504–1518. https://doi.org/10.1016/j.dsr2.2010.02.018

Rosengard, S. Z., Lam, P. J., Balch, W. M., Auro, M. E., Pike, S., Drapeau, D., & Bowler, B. (2015). Carbon export and transfer to depth across the Southern Ocean Great Calcite Belt. *Biogeosciences*, *12*(13), 3953–3971. https://doi.org/10.5194/bg-12-3953-2015

Schlitzer, R., Anderson, R. F., Dodas, E. M., Lohan, M., Geibert, W., Tagliabue, A., Bowie, A., Jeandel, C., Maldonado, M. T., Landing, W. M., Cockwell, D., Abadie, C., Abouchami, W., Achterberg, E. P., Agather, A., Aguliar-Islas, A., van Aken, H. M., Andersen, M., Archer, C., … Zurbrick, C. (2018). The GEOTRACES Intermediate Data Product 2017. *Chemical Geology*, *493*, 210–223. https://doi.org/10.1016/j.chemgeo.2018.05.040

Strzepek, R. F., Maldonado, M. T., Higgins, J. L., Hall, J., Safi, K., Wilhelm, S. W., & Boyd, P. W. (2005). Spinning the "ferrous wheel": The importance of the microbial community in an iron budget during the FeCycle experiment. *Global Biogeochemical Cycles*, *19*(4). https://doi.org/10.1029/2005GB002490

Strzepek, R. F., Hunter, K. A., Frew, R. D., Harrison, P. J., & Boyd, P. W. (2012). Iron-light interactions differ in Southern Ocean phytoplankton. *Limnology and Oceanography*, *57*(4), 1182–1200. https://doi.org/10.4319/LO.2012.57.4.1182

Strzepek, R. F., Boyd, P. W., & Sunda, W. G. (2019). Photosynthetic adaptation to low iron, light, and temperature in Southern Ocean phytoplankton. *Proceedings of the National Academy of Sciences*, *116*(10), 4388–4393. https://doi.org/10.1073/PNAS.1810886116

Tagliabue, A., & Arrigo, K. R. (2006). Processes governing the supply of iron to phytoplankton in stratified seas. *Journal of Geophysical Research: Oceans*, *111*(6), 6019. https://doi.org/10.1029/2005JC003363

Tagliabue, A., Bowie, A. R., Boyd, P. W., Buck, K. N., Johnson, K. S., & Saito, M. A. (2017). The integral role of iron in ocean biogeochemistry. In *Nature* (Vol. 543, Issue 7643, pp. 51–59). Nature Publishing Group. https://doi.org/10.1038/nature21058

Tagliabue, A., Bowie, A. R., DeVries, T., Ellwood, M. J., Landing, W. M., Milne, A., Ohnemus, D. C., Twining, B. S., & Boyd, P. W. (2019). The interplay between regeneration and scavenging fluxes drives ocean iron cycling. *Nature Communications*, *10*(1), 1–8. https://doi.org/10.1038/s41467-019-12775-5

Tagliabue, A., Mtshali, T., Aumont, O., Bowie, A. R., Klunder, M. B., Roychoudhury, A. N., & Swart, S. (2012). A global compilation of dissolved iron measurements: Focus on distributions and processes in the Southern Ocean. *Biogeosciences*, *9*(6), 2333–2349. https://doi.org/10.5194/bg-9-2333-2012

Tagliabue, A., Sallée, J. B., Bowie, A. R., Lévy, M., Swart, S., & Boyd, P. W. (2014). Surface-water iron supplies in the Southern Ocean sustained by deep winter mixing. *Nature Geoscience*, *7*(4), 314–320. https://doi.org/10.1038/ngeo2101

Tagliabue, A., & Völker, C. (2011). Towards accounting for dissolved iron speciation in global ocean models. *Biogeosciences*, *8*(10), 3025–3039. https://doi.org/10.5194/bg-8-3025-2011

Thuróczy, C. E., Gerringa, L. J. A., Klunder, M. B., Middag, R., Laan, P., Timmermans, K. R., & de Baar, H. J. W. (2010). Speciation of Fe in the Eastern North Atlantic Ocean. *Deep-Sea Research Part I: Oceanographic Research Papers*, *57*(11), 1444–1453. https://doi.org/10.1016/j.dsr.2010.08.004

Twining, B. S., Nodder, S. D., King, A. L., Hutchins, D. A., LeCleir, G. R., DeBruyn, J. M., Maas, E. W., Vogt, S., Wilhelm, S. W., & Boyd, P. W. (2014). Differential remineralization of major and trace elements in sinking diatoms. *Limnology and Oceanography*, *59*(3), 689–704. https://doi.org/https://doi.org/10.4319/lo.2014.59.3.0689

van Beek, P., François, R., Conte, M., Reyss, J. L., Souhaut, M., & Charette, M. (2007). 228Ra/226Ra and 226Ra/Ba ratios to track barite formation and transport in the water column. *Geochimica et Cosmochimica Acta*, *71*(1), 71–86. https://doi.org/10.1016/j.gca.2006.07.041

Velasquez, I. B., Ibisanmi, E., Maas, E. W., Boyd, P. W., Nodder, S., & Sander, S. G. (2016). Ferrioxamine siderophores detected amongst iron binding ligands produced during the remineralization of marine particles. *Frontiers in Marine Science*, *3*(SEP), 172. https://doi.org/10.3389/fmars.2016.00172

Völker, C., & Tagliabue, A. (2015). Modeling organic iron-binding ligands in a three-dimensional biogeochemical ocean model. *Marine Chemistry*, *173*, 67–77. https://doi.org/10.1016/j.marchem.2014.11.008

Chapter 2: Early winter Southern Indian Ocean dissolved iron distributions and remineralisation (GEOTRACES GIPr07 cruise)

2.1 Introduction

The SO biological carbon pump, the pathway by which phytoplankton consume and release inorganic carbon through photosynthesis and respiration, is of global significance due to the centrality of the SO. It is, however, inefficient due to large areas of iron (Fe) limitation (Martin, 1990; Martin et al., 1990; Moore et al., 2001), known as HNLC regions, where large amounts of macronutrients are left unused due to low (sub-nanomolar) concentrations of Fe, which limit the efficient use of macronutrients by phytoplankton (Martin, 1990; Martin et al., 1990). Better constraining marine Fe biogeochemistry, the seasonal cycle and how processes are linked is crucial to further interpret changes linked to climate change using biogeochemical models (Boyd and Ellwood; 2010; Tagliabue et al., 2014; 2017).

Pathways by which dissolved Fe (dFe) is supplied to surface waters is of particular interest, as this will facilitate CO_2 drawdown by phytoplankton via photosynthesis by the relief of Fe-limitation in the surface waters of HNLC regions of the SO (Tagliabue et al., 2014). Several processes and sources can affect the distribution of dFe throughout the water column, namely, dust deposition, hydrothermal activity, continental margin runoff, sea ice melt, diapycnal diffusion, vertical Ekman pumping, lateral advection, winter entrainment and remineralisation (De Jong et al., 2012; 2015; Tagliabue et al., 2014; 2017). Atmospheric inputs are expected to be minimal in open waters of the SO (Jickells et al., 2005), but episodic high dust inputs may settle and increase deep concentrations (Jickells and Moore; 2015). Recent studies have also linked large phytoplankton blooms to advected hydrothermal dFe supply to surface waters (Ardyna et al., 2019; Schine et al., 2021; Tagliabue & Resing, 2016). Nevertheless, certain sources of Fe are localised, such as sea ice melt and dust deposition, and therefore internal cycling and physical fluxes dominate dFe distributions in the HNLC SO (De Jong et al., 2012; 2015; Tagliabue et al., 2014). It is assumed that there is a subsurface winter reservoir which

will resupply the surface water dFe stock, via multiple pathways, to fuel the spring and summer blooms (Tagliabue et al., 2014). Of these pathways, winter entertainment has been reported to be a dominant flux of the subsurface dFe reservoir to the surface mixed layer (Achterberg et al., 2018; Tagliabue et al., 2014). Remineralisation is thought to be the largest source for replenishment of the winter reservoir in HNLC regions of the SO (Tagliabue et al., 2017).

Apparent oxygen utilisation (AOU) is a well-used proxy to estimate remineralised nutrients based on the assumption that nutrient concentrations are made up of the "pre-formed" and the "remineralised" component ($[P] = [P_{pre}] + [P_{rem}]$: Ito and Follows, 2005). With estimates of cellular Fe:P ratios, we can further estimate remineralised Fe, using this remineralisation proxy and PO_4^{3-} as the benchmark nutrient (Ito and Follows, 2005; Parekh et al., 2005; Tagliabue et al., 2019; Twining et al., 2014). While some inaccuracies have been detected with AOU as a remineralisation proxy, specifically in high latitude areas, due to O_2 undersaturation as a consequence of large temperature gradients (Ito et al., 2004), AOU has still proven to be a reliable remineralisation proxy.

Winter dFe observations within the SO are limited due to harsh conditions and extended sea ice cover during these months of the year, making it a challenge to obtain observations, especially in areas of extended sea ice cover. To our knowledge there are currently only two published studies, one in the Atlantic basin (Mtshali et al., 2019) and another in the Pacific basin (Ellwood et al., 2008), with both studies conducted in the Subantarctic zone (SAZ). There are significant gaps in our knowledge with respect to the sources of dFe during early winter that supply the upper surface mixed layer and the replenishment of the expected winter reservoir (Tagliabue et al., 2014). Winter dFe data is therefore crucial for giving insight into the seasonal cycle of this micronutrient (Tagliabue et al., 2014; 2017). In this context, as part of a GEOTRACES process study (GIpr07) of a transect along 30°E in the Southern Indian Ocean (SIO, 58.5°S to 41.0°S), we studied dFe distributions during early austral winter (July

2017) to better constrain SO dFe distributions and cycling on a basin scale. We also aim to better understand the seasonal cycle and how it affects the supply of dFe to the surface mixed layer. To facilitate obtaining insight into dFe processes and fluxes we investigate the subsurface replenishment of the winter dFe reservoir and how this compares to fluxes, latitudinally in the SIO during winter. We also compare distributions and fluxes of dFe throughout the SO, investigating how they compare seasonally and on a basin scale.

2.2 Materials and Methods

2.2.1 Sampling and hydrography

The GEOTRACES GIpr07 cruise took place onboard the *R/V SA Agulhas II*, during early austral winter of 2017, along 30°E longitude, from 58.5°S to 41.0°S (WOCE I06S, Figure 2.1a). Seawater samples were collected from 25 m down to 1500 m, for shallow stations, and from 25 m down to 4250 m, for deep stations.

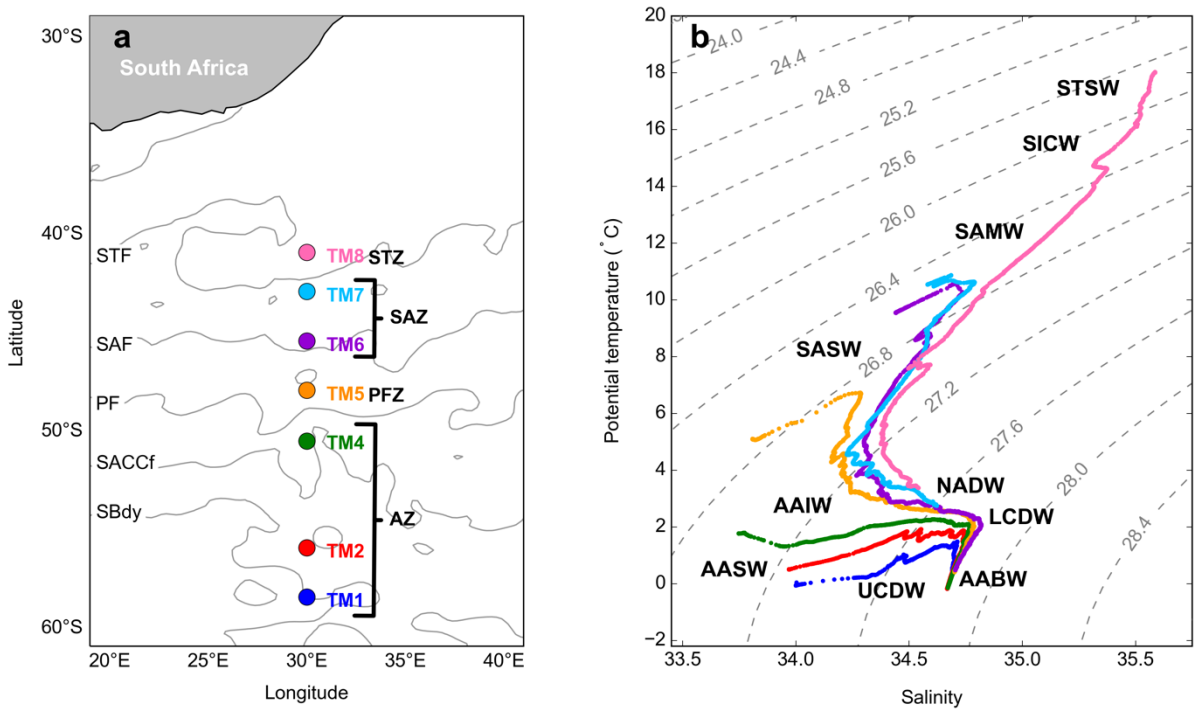

Figure 2.1: (a) GEOTRACES GIPr07 cruise sampling stations overlaid on a map with frontal positions; namely, the Subtropical Front (STF), the Subantarctic Front (SAF), the Polar Front (PF), the Southern Antarctic Circumpolar Front (SACCf) and the Southern Boundary (SBdy), as determined by mean absolute dynamic topography (MADT) and crossing over three zones; namely, the Antarctic zone (AZ), the Polar frontal zone (PFZ), the Subantarctic zone (SAZ) and the Subtropical zone (STZ), (b) Potential temperature plotted against salinity, overlaid on isopycnals and identification of water masses sampled; namely, Subtropical Surface Water (STSW), South Indian Central Water (SICW), Subantarctic Mode Water (SAMW), Subantarctic Surface Water (SASW), Antarctic Intermediate Water (AAIW), Antarctic Surface Water (AASW), North Atlantic Deep Water (NADW), Lower Circumpolar Deep Water (LCDW), Upper Circumpolar Deep Water (UCDW), Antarctic Bottom Water (AABW).

Frontal positions were determined by mean absolute dynamic topography obtained from the CLS/AVISO product (Rio et al., 2011), defining boundaries as reported by Swart et al. (2010). Fronts identified were, the Subtropical Front (STF), the Subantarctic Front (SAF), the Polar

Front (PF), the Southern Antarctic Circumpolar Front (SACCf) and the Southern Boundary (SBdy), from north to south (Figure 2.1a).

2.2.2 Temperature, salinity, dissolved O_2 and chlorophyll α

Temperature (T, °C), salinity (S), dissolved O_2 (µmol L^{-1}) and fluorescence-derived chlorophyll α (Chl-α) measurements were obtained from CTD sensors (SBE 911plus). Discrete samples were collected and analysed onboard for the calibration of sensor measurements of S (8410A Portasal salinometer), dissolved O_2 (Metrohm 848 titrino plus; Ehrhardt et al., 1983) and Chl-α concentrations (Turner Designs Trilogy Fluorometer 7500-000; Welschmeyer, 1994). The detailed Chl-α methodology is described by Weir et al. (2020). Strong correlations were obtained between sensor data and discrete samples with correlation coefficients of R^2 = 0.99 (S), R^2 = 0.83 (dissolved O_2) and R^2 = 0.92 (Chl-α), respectively. Potential density (σ_θ) and potential temperature (θ) were calculated from in situ temperature and salinity measurements along the transect (Gill, 1982), using the python seawater package. These parameters were used to identify water masses and biogeochemical zones sampled along the transect. The mixed layer depth (MLD) was identified as the depth at which there was a change of 0.03 kg m^{-3} in σ_θ from a near-surface value at ~ 10 m depth (de Boyer Montégut, et al., 2004).

2.2.3 Macronutrient analysis

Seawater collected for macronutrient analyses was filtered through a 0.2 µm pore size syringe filter into 50 mL tubes (Falcon®) and stored frozen at -20°C until further analysis on land. Samples were analysed three months after sample collection, for nitrate (NO_3^- (µmol L^{-1})), phosphate (PO_4^{3-} (µmol L^{-1})) and silicic acid ($Si(OH)_4$ (µmol L^{-1})) concentrations, at the Marine Biogeochemistry Laboratory at the University of Cape Town (MBL-UCT). NO_3^- and $Si(OH)_4$ concentrations were measured using a Lachat Quick-Chem flow injection autoanalyzer

(Wolters, 2002; Egan, 2008), with precisions of ± 0.4 µmol L^{-1} and ± 0.2 µmol L^{-1}, and detection limits (the lowest calibration standard) of 0.1 µmol L^{-1} and 0.2 µmol L^{-1}, respectively. PO_4^{3-} concentrations were determined by the manual colorimetric method (Thermo Scientific Genesis 30 Visible spectrophotometer) as described by Ehrhardt et al. (1983), with a precision of ± 0.06 µmol L^{-1} and a detection limit (the lowest calibration standard) of 0.05 µmol L^{-1}. The detailed methodology is described by Weir et al. (2020).

2.2.4 dFe analysis

Seawater samples collected for dissolved Fe (dFe) were analyzed ~ 9 months after collection, using inline pre-concentration (x50) SeaFAST pico (Elemental Scientific Inc., ESI) and sector field inductively coupled plasma mass spectrometry (SF-ICP-MS, Element XR Thermo Scientific) (Lagerström et al. 2013). All sample processing and analyses were conducted under a class 100 HEPA filtered laminar flow hood in a trace metal clean laboratory, following the GEOTRACES protocols (Cutter et al. 2017). A spike of 1 µg L^{-1} indium (In) was used as an internal standard to correct for instrument drift. The detection limit, defined as three times the standard deviation of the blanks (acidified Milli Q water), was 0.042 nmol L^{-1} (n = 7). The mean percentage error of analyses was 19.5 ± 17.8% (mean ± SD, n = 56), which was determined by the repeat analysis of random samples. Analysis of GEOTRACES SAFe S and SAFe D1 reference seawaters was used for the assessment of method accuracy. Concentrations obtained (0.104 ± 0.004 nmol L^{-1}, mean ± SD, n = 2, and 0.975 ± 0.120 nmol L^{-1}, mean ± SD, n = 9, respectively) were in good agreement with consensus values (0.095 ± 0.008 nmol L^{-1}; 0.95 ± 0.02 nmol L^{-1}, respectively). The North Pacific GSP and GSC reference seawaters were also analysed and calibrated against the SAFe reference seawater. These were then used as internal standards, using the calibrated values as the acceptance criteria (0.162 ± 0.033 nmol L^{-1}, n = 9; 1.881 ± 0.238 nmol L^{-1}, n = 7; mean ± SD, for consensus values of 0.155 ± 0.045 nmol L^{-1} and 1.535 ± 0.115 nmol L^{-1}, respectively).

2.2.5 AOU as a proxy for remineralised dFe

Temperature and salinity measurements were used to calculate AOU as described by Weiss (1970), using Eq. 1 (Ito and Follows, 2005).

$$AOU = O_{2,sat}(T,S) - [O_2] \quad (1)$$

Where AOU is expressed in µmol L^{-1}, T is the in situ temperature, S is the in situ salinity and $O_{2,sat}$ is the surface saturated O_2 concentration as calculated for the corresponding in situ temperature and salinity. $[O_2]$ is the in situ dissolved O_2 concentration, expressed in µmol L^{-1}. Using PO_4^{3-} and AOU profiles, the remineralisation depth range was identified as the depth where both parameters start increasing at the base of the MLD down to the depth where the concentrations either stay constant or start decreasing (Figure 2.2, green shaded area). PO_4^{3-} concentrations from within the remineralisation depth range were then plotted against the corresponding AOU concentrations, for each station, and least squares linear regressions were applied to each plot. Using the intercepts of the linear regressions, pre-formed PO_4^{3-} concentrations were estimated. We then estimated the maximum remineralised dFe concentrations attainable without the removal of Fe via scavenging, by multiplying the estimated remineralised $[PO_4^{3-}]$ by a Fe:P (mmol mol^{-1}) ratio of 0.54 (Eq. 2). The Fe:P ratio is an estimate of the stoichiometries of remineralised cellular components from diatoms in the upper 100 m of the water column, from a Southern Pacific Ocean study (Twining et al., 2014). This ratio is also comparable to the Fe:P ratio (0.47) used in a global biogeochemical model by Parekh et al. (2005). The approach used is based on the theory of first-order governing processes as explained by Tagliabue et al. (2017) and references therein, assuming that subducted (pre-formed) and remineralised dFe are the only two forms of dFe present in the mesopelagic zone, which is the case for PO_4^{3-} (Tagliabue et al., 2019).

$$[dFe_{rem}] = ([PO_4^{3-}] - [PO_{4pre}^{3-}]) \times Fe{:}P \quad (2)$$

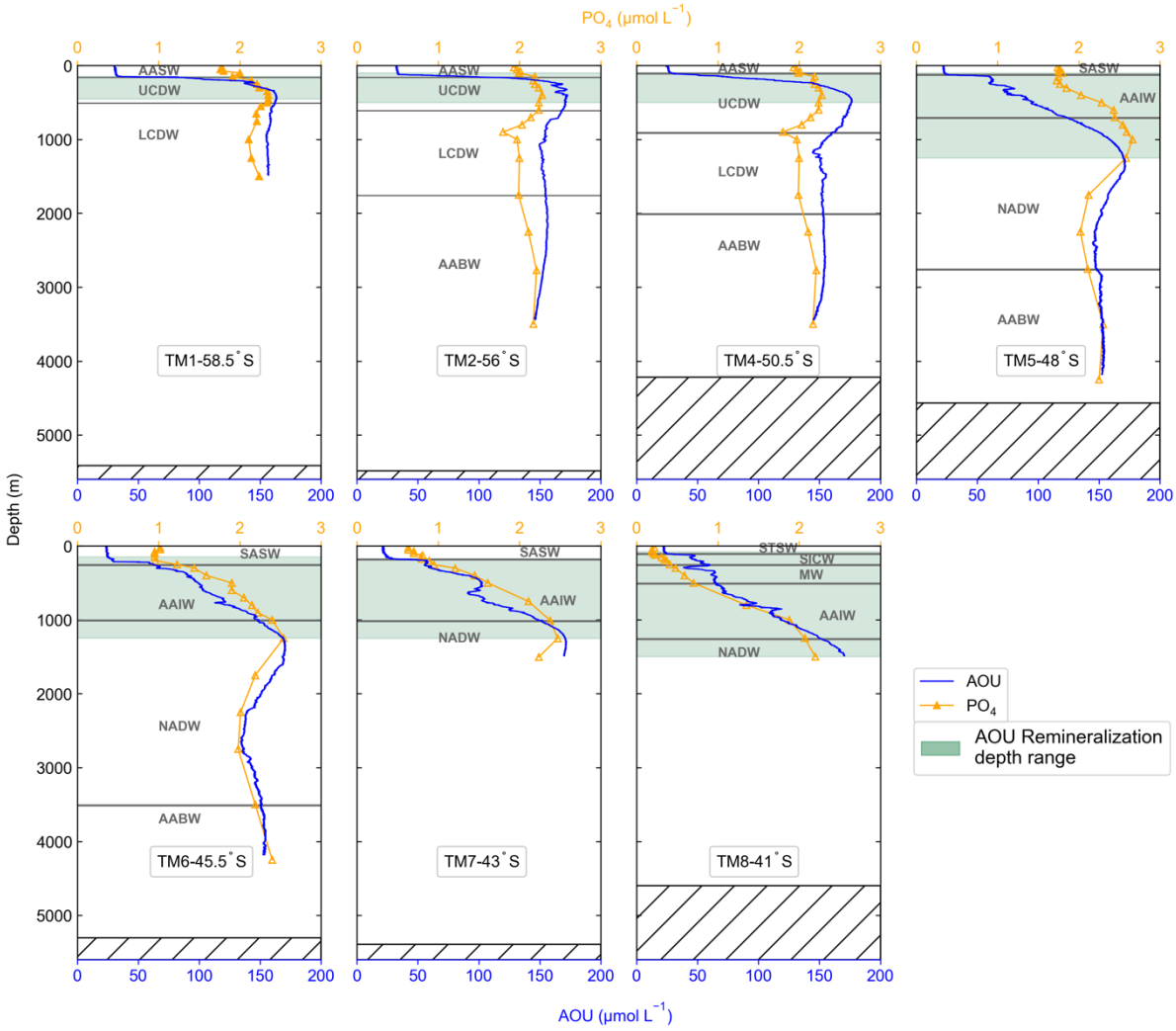

Figure 2.2: Profiles of apparent oxygen utilisation (AOU; blue) and phosphate (PO_4^{3-}; orange) sampled along the transect, plotted against depth, for stations TM1 to TM8, from south to north, with water masses overlaid. The green shaded area is the identified AOU remineralisation depth range, and the hatched area is the ocean floor.

Where [dFe_{rem}] (nmol L^{-1}) is the estimated maximum remineralised dFe concentrations attainable prior to any removal via scavenging, [PO_4^{3-}] (µmol L^{-1}) and [$PO_4^{3-}{}_{pre}$] (µmol L^{-1}) is the in situ PO_4^{3-} concentration and the estimated pre-formed concentration, respectively. The integrated [dFe_{rem}] (µmol m^{-2}) stocks within the remineralisation depth ranges were calculated for each station and the percentage [dFe_{rem}] was estimated against the integrated observed dFe stock of the corresponding depth range.

Although this approach is an overly simplified version of the processes governing the magnitude of observed remineralised dFe in the mesopelagic zone, not taking into account

scavenging and other external sources, as well as assuming a constant Fe:P ratio, we do believe that this does give an acceptable estimate of the maximum remineralised [dFe] attainable in the study area, prior to removal via scavenging, which is yet to be quantified (Tagliabue et al., 2017; 2019; Boyd et al., 2017). It must, however, be acknowledged that the [dFe] observed in the mesopelagic zone is the net remineralised dFe as a result of the balance between remineralisation and scavenging fluxes (Tagliabue et al., 2019), and not the maximum estimated remineralised [dFe].

Significant correlations between dFe and AOU (R^2 = 0.67 up to R^2 = 0.96; p-value < 0.05: Figure A1) and dFe and PO_4^{3-} (R^2 = 0.44 up to R^2 = 0.94; p-value < 0.05: Figure A2), obtained for the study area, supports the assumption that remineralisation is the dominant source of dFe observed in the mesopelagic zone, at the time of sampling. This is further discussed in section 2.4.3.

2.2.6 Quantifying physical supply terms of dFe to the surface mixed layer

Physical supply terms were calculated assuming that the winter dFe distribution measured along the transect was the initial state for the annual supply to the surface mixed layer (see discussion, section 2.4.3). Diapycnal diffusion was estimated as described by Tagliabue et al. (2014), where the change in dFe concentration at the MLD was multiplied with the vertical diffusivity constant (k_z) of 10^{-4} m^2 s^{-1} (Cisewski et al., 2005). Vertical Ekman pumping (downwelling/upwelling) was determined by multiplying the mean wind stress curl of the month of sampling (m d^{-1}; Tsujino et al., 2018) with the concentration directly beneath the MLD (Tagliabue et al., 2014). Lateral advection was estimated as described by De Jong et al. (2012), where the northward surface current velocity (m s^{-1}) was multiplied by the latitudinal gradient in surface dFe concentration ($\delta dFe/\delta x$), where x is the distance from the southernmost station (m) and the current velocity product was processed by SSALTO/DUACS and distributed by AVISO+ (https://www.aviso.altimetry.fr) with support from CNES. Winter

entrainment was estimated as the integrated dFe concentration of the maximum MLD (Table A1), obtained from ARGO data for the year of sampling (Achterberg et al., 2018; Tagliabue et al., 2014). The ARGO data were collected and made freely available by the International Argo Program and the national programs that contribute to it (https://argo.ucsd.edu, https://www.ocean-ops.org). The Argo Program is part of the Global Ocean Observing System.

2.2.7 Statistical analysis

The least squares regression method was used for the assessment of correlation significance (Barbur et al., 1994). Significant differences between zones and between regression slopes were tested using Welch's t-test, with an alpha of 0.05 (95% confidence level) (Kokoska and Zwillinger, 2000).

2.3 Results

2.3.1 Study area hydrography

Potential temperature and salinity measurements along the transect ranged from -0.06 to 18.03 °C and from 33.77 to 35.59, respectively. The surface water ranges define three biogeochemical zones sampled; namely, the Antarctic zone (AZ; $\theta < 2$ °C; $S < 34$) between 50°S and 58°S, the Subantarctic zone (SAZ; $5 < \theta < 11$ °C; $33.8 < S < 34.7$) between 43°S and 48°S, and the Subtropical zone (STZ; $\theta \geq 17.9$ °C; $S \cong 35.6$) at 41°S (Figure 2.1b; Anilkumar and Sabu, 2017; Orsi et al., 1995). The MLDs along the transect ranged between 97 and 215 m (144 ± 39 m; mean ± SD, n = 7; Table A2), shoaling towards the PF. The potential temperature-salinity (θ-S) plot of the water masses sampled during this study is shown in Figure 2.1b. In total, ten water masses were identified along the transect, throughout the water column, using potential density (σ_θ) ranges. South of the PF (≳50°S; TM1, 2 & 4), from surface to depth, Antarctic Surface Water (AASW; $27 < \sigma_\theta < 27.4$ kg.m^{-3}), Upper and Lower Circumpolar Deep Water (UCDW; $27.2 < \sigma_\theta < 27.75$ kg.m^{-3} and LCDW; $27.75 < \sigma_\theta < 27.85$ kg.m^{-3}, respectively), and Antarctic Bottom Water (AABW; $27.8 < \sigma_\theta < 27.85$ kg.m^{-3}) were identified. North of the PF (≲50°S) up to 43°S (TM5, 6 & 7), from surface to depth, Subantarctic Surface Water (SASW; $26.5 < \sigma_\theta < 26.75$ kg.m^{-3}), Antarctic Intermediate Water (AAIW; $26.7 < \sigma_\theta < 27.4$ kg.m^{-3}), North Atlantic Deep Water (NADW; $27 < \sigma_\theta < 27.85$ kg.m^{-3}) and, as far as 45.5°S, AABW was sampled close to the ocean floor. At the northernmost station at 41°S (TM8), in the STZ, we sampled Subtropical Surface Water (STSW; $\sigma_\theta \cong 25.7$ kg.m^{-3}), South Indian Central Water (SICW; $25.8 < \sigma_\theta < 26.2$ kg.m^{-3}), SAMW ($26.2 < \sigma_\theta < 26.6$ kg.m^{-3}), AAIW and NADW.

2.3.2 Macronutrients and Chl-α distributions

NO_3^- and PO_4^{3-} concentrations ranged from 2.4 to 37.4 µmol L^{-1} and 0.19 to 2.6 µmol L^{-1}, respectively (Weir et al., 2020) (Figure 2.3a & b; Table A3). Profiles exhibited the expected nutrient distributions with a surface minimum, increasing with depth. In general, concentrations were higher south of the PF, decreasing northwards, at corresponding depths. Surface water NO_3^- and PO_4^{3-} concentrations decreased tenfold from 28.5 ± 1.6 µmol L^{-1} and 1.91 ± 0.11 µmol L^{-1} (median ± SD, n = 13), respectively, in the AZ, down to 2.80 ± 0.41 µmol L^{-1} and 0.20 ± 0.02 µmol L^{-1} (median ± SD, n = 4), respectively, in the STZ (Figure 2.4a & b; Table A3).

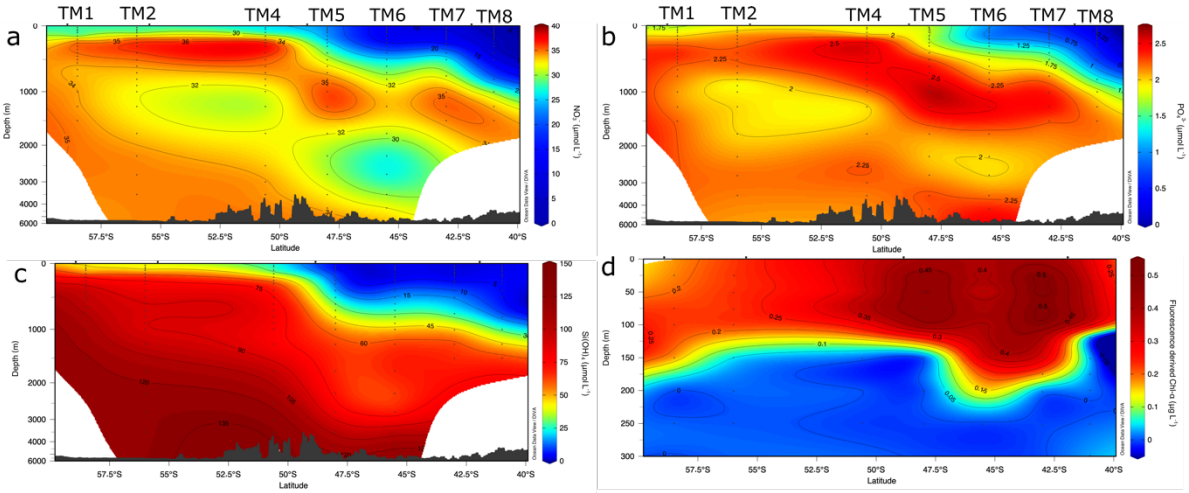

Figure 2.3: Gridded section plots of (a) nitrate (NO_3^-), (b) phosphate (PO_4^{3-}), (c) silicic acid ($Si(OH)_4$) (Weir et al., 2020) and (d) in-situ fluorescence derived Chl-α concentrations along the transect sampled.

$Si(OH)_4$ concentrations ranged from 1.7 to 132.2 µmol L^{-1}, also displaying the typical nutrient distribution, with a surface minimum and an increase with depth (Weir et al., 2020) (Figure 2.3c; Table A3). A sharp decrease was observed in surface water concentrations across the PF, with concentrations of 44.73 ± 10.05 µmol L^{-1} (median ± SD, n = 13) in the AZ, decreasing down to 2.91 ± 0.02 µmol L^{-1} (median ± SD, n = 4) at the northernmost station, in the STZ. Concentrations increased with depth, the highest concentrations being measured in AABW, at 124.07 ± 9.45 µmol L^{-1} (median ± SD, n = 9; Figure 2.4c; Table A3).

To determine if significant changes occurred in nutrient concentrations across water masses, statistical tests were run on data split between water masses (Figure 2.4a-c, Table A3 and A4).

NO_3^- and PO_4^{3-} concentrations (Weir et al., 2020) decreased significantly northwards, in surface and intermediate water masses, whereas concentrations in AABW and NADW were not significantly different (Table A4). For both NO_3^- and PO_4^{3-} concentrations (Weir et al., 2020) a significant increase was observed between surface and intermediate water masses. In the AZ, NO_3^- and PO_4^{3-} concentrations increased to a maximum in UCDW and remained relatively constant down to AABW. Concentrations in the SAZ increased from AAIW, up to a maximum in NADW.

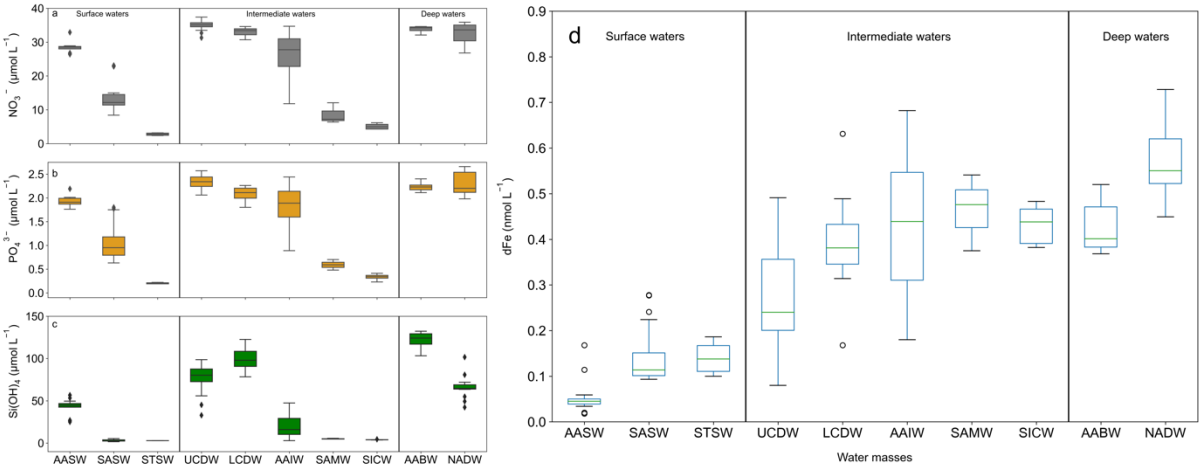

Figure 2.4: Boxplot of macronutrients, NO_3^-, PO_4^{3-} and $Si(OH)_4$, (Weir et al., 2020), (a-c) and dFe (d) concentrations split into water masses along the transect sampled. From left to right water masses are split into surface, intermediate and deep water masses, from the AZ up to the STZ. Diamonds (a-c) and open circles (d) are outliers.

$Si(OH)_4$ concentrations (Weir et al., 2020) were significantly lower in SASW and STSW when compared to AASW concentrations (Table A4), as is the general latitudinal distribution of this macronutrient throughout the SO during summer months (Janssen et al., 2020). $Si(OH)_4$ concentrations (Weir et al., 2020) also increased significantly across water masses with depth and southwards, increasing 10-fold southwards and with depth, from AAIW, in the SAZ, to maximum concentrations in AABW, in the AZ (Figure 2.4c, Table A3 and A4). In the STZ, all macronutrients were depleted in STSW, characteristic of this oligotrophic region (Sedwick et al., 2002), increasing significantly with depth from SICW up to a maximum in NADW (Figure 2.4a-c; Table A3 and A4).

Chl-α concentrations were low along the transect, ranging from values close to zero up to 0.52 µg L^{-1}, in the upper 200 m of the water column (Weir et al., 2020) (Figure 2.3d). The lowest concentrations were observed in the AZ at 0.18 ± 0.11 µg L^{-1} (mean ± SD, n = 16), increasing northwards up to 0.32 ± 0.17 µg L^{-1} (mean ± SD, n = 26) in the SAZ and STZ.

2.3.3 dFe distributions

Dissolved Fe concentrations along the transect ranged from 0.018 to 0.728 nmol L^{-1}, increasing northwards and with depth (Figure 2.5). Profiles exhibited the expected hybrid distribution of depletion in surface waters, a subsurface increase and then reaching relatively constant values in deep waters (Bruland and Lohan 2003).

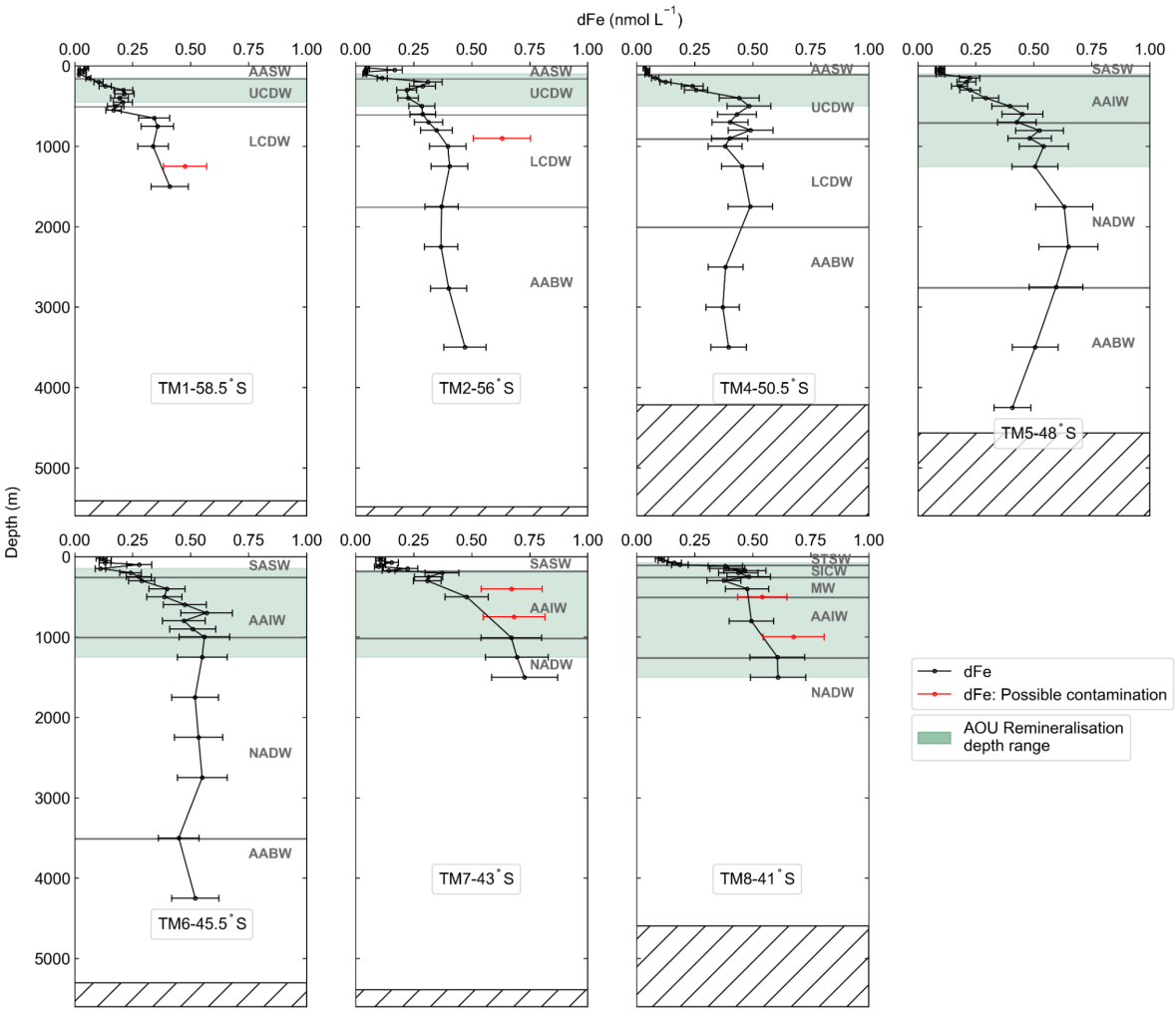

Figure 2.5: Profiles of dissolved Fe (dFe; black) with error bars sampled along the transect, plotted against depth, for stations TM1 to TM8, from south to north, with water masses overlaid. Data points detached from the profile (red) are dFe measurements which might have been high due to possible contamination and have therefore been excluded from further analysis of the data. The green shaded area is the identified AOU remineralisation depth range, and the hatched area is the ocean floor.

When dividing dFe concentrations into their respective water masses, median concentrations increased significantly northwards, across zones within each water mass type, namely, surface, intermediate and deep water masses (Figure 2.4d, Table A3 and A4). Surface water concentrations increased significantly from 0.05 ± 0.04 nmol L^{-1} (median ± SD, n = 13) in the AZ up to 0.11 ± 0.06 nmol L^{-1} (median ± SD, n = 18), in the SAZ, and 0.14 ± 0.04 nmol L^{-1} (median ± SD, n = 4), in the STZ. In intermediate waters there was a significant increase northward from 0.24 ± 0.12 nmol L^{-1} (median ± SD, n = 23) in the AZ to 0.44 ± 0.15 nmol L^{-1} (median ± SD, n = 26) in the SAZ and 0.44 ± 0.05 nmol L^{-1} (median ± SD, n = 5) in the STZ. Deep water concentrations also increased significantly northwards from 0.40 ± 0.06 nmol L^{-1} (median ± SD, n = 9) in the AZ up to 0.55 ± 0.08 nmol L^{-1} (medium ± SD, n = 15) in the SAZ and STZ. Concentrations also increased significantly with depth, from surface to intermediate waters, in agreement with the expected remineralisation signal (Figure 2.4d; Table A3 and A4), reaching maximum values in deep waters, along the transect A subsurface increase, below the MLD, was observed at each station, becoming more pronounced and spanned wider depth ranges northwards along the transect (Figure 2.5).

The Fe-limitation tracer Fe* (Fe* = [dFe] - $r_{Fe:P}[PO_4^{3-}]$) was calculated for the observations made during this study, where $r_{Fe:P}$ is the Fe:P (0.54 mmol mol^{-1}) molar ratio for SO phytoplankton (Twinning et al., 2014), and [dFe] and $[PO_4^{-3}]$ are the in situ concentrations. The Fe* tracer can give insight into the degree of Fe limitation of pytoplankton and any latitudinal trend in limitation, if one is present (Parekh et al., 2005). Along the transect Fe* was mostly negative in surface water masses, increasing northwards from -1.07 up to 0.07 (-0.58 ± 0.39; mean ± SD, n = 35), indicating Fe limitation with respect to PO_4^{3-}. Fe* was close to zero in the STZ, at TM8 (41°S), at 0.03 ± 0.04 (mean ± SD, n = 4; Figure 2.6), indicating that phytoplankton in these waters were about equally limited by PO_4^{3-} as they were Fe limited.

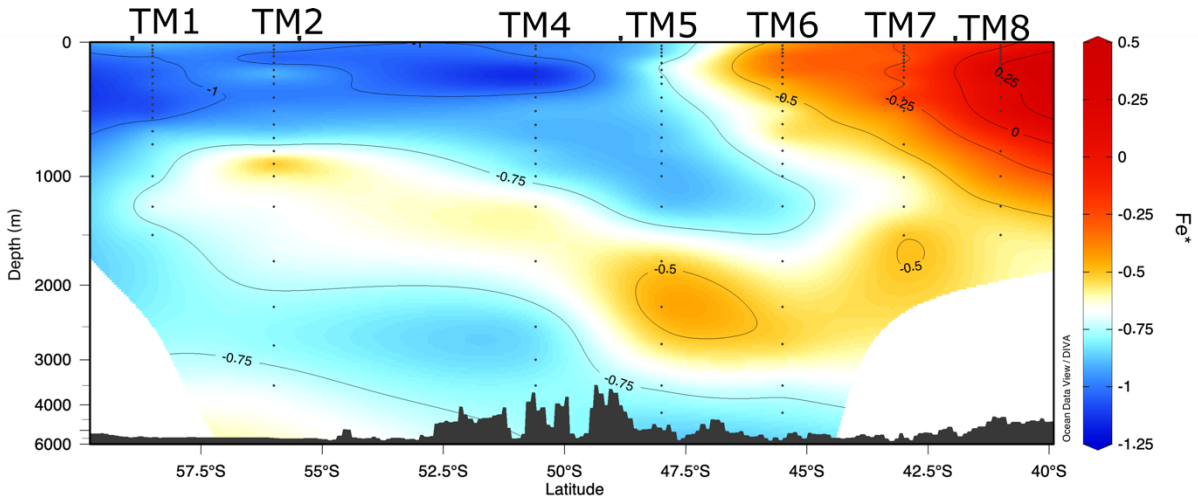

Figure 2.6: Gridded section plot of Fe-limitation tracer, Fe* (Fe* = [dFe] - rFe:P[PO_4^{3-}]), along the transect.

2.3.4 AOU and remineralised Fe estimates

AOU profiles along the transect were very similar to PO_4^{3-} profiles (Figure 2.2). They all exhibited a surface minimum increasing sharply at the MLD up to a maximum in the AOU remineralisation depth range, then decreased slightly to relative constant values in deep waters. AOU values ranged from 21 to 177 µmol L^{-1} along the transect. The upper surface water (≤ 200 m) values south of the PF were 52 ± 34 µmol L^{-1} (mean ± SD, n = 603), decreasing significantly northwards in the SAZ and STZ to 30 ± 12 µmol L^{-1} (mean ± SD, n = 804; t-statistic = 15.35; p-value < 0.05). The AOU remineralisation depth range was shallow south of the PF (~ 200 m down to ≤ 500 m) and deepened in the SAZ and STZ (~200 m down to ≤ 1500 m). In general, AOU values within the remineralisation depth ranges were 161 ± 13 µmol L^{-1} (mean ± SD, n = 911) south of the PF and decreased northwards to 123 ± 39 µmol L^{-1} (mean ± SD, n = 5239; t-statistic = 56.57; p-value < 0.05) in the SAZ and STZ. Below the remineralisation depth ranges AOU values were similar along the transect at 155 ± 6 µmol L^{-1} (mean ± SD, n = 6988) south of the PF and 150 ± 7 µmol L^{-1} (mean ± SD, n = 5478) northwards. Strong statistically significant correlations (R^2 = 0.78 up to R^2 = 0.98; p-value < 0.05) were obtained for all regressions of PO_4^{3-} against AOU for all stations along the transect (Figure 2.7). Pre-formed PO_4^{3-} concentrations, identified as the intercept of each regression, ranged

from 1.97 µmol L^{-1} in the AZ down to zero in the STZ (assuming that a negative intercept indicates zero pre-formed PO_4^{3-}).

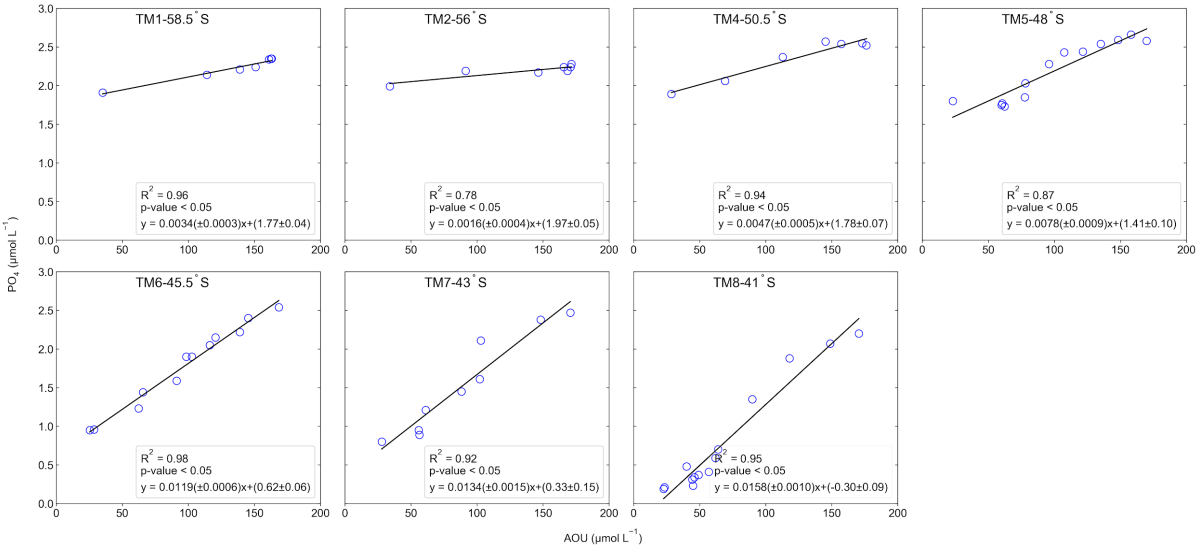

Figure 2.7: Least squares linear regression of PO_4^{3-} concentrations within the AOU remineralisation depth range plotted against AOU, for each station along the transect, from TM1 to TM8, from south to north.

Estimates of mesopelagic integrated [dFe_{rem}] stock increased northwards along the transect, with a sharp increase across the PF (Figure 2.8a). Values ranged from 52.7 ± 0.6 µmol m^{-2} in the AZ up to 796.9 ± 8.0 µmol m^{-2} in the SAZ. Estimates in the AZ (TM1 - TM4) were an order of magnitude lower at 89.1 ± 44.7 µmol m^{-2} (mean ± SD, n = 3) than values northwards of the PF (TM5 - TM8) at 679.2 ± 110.8 µmol m^{-2} (mean ± SD, n = 4). From the AZ to the SAZ an increase in the estimated integrated [dFe_{rem}] stock from 139.0 ± 2.2 µmol m^{-2} at 50.5°S up to 796.9 ± 8.0 µmol m^{-2} at 45.5°S was observed. Thereafter a slight decrease to 607.3 ± 7.7 µmol m^{-2} at 43°S and then an increase up to 747.8 ± 12.2 µmol m^{-2} in the STZ at 41°S.

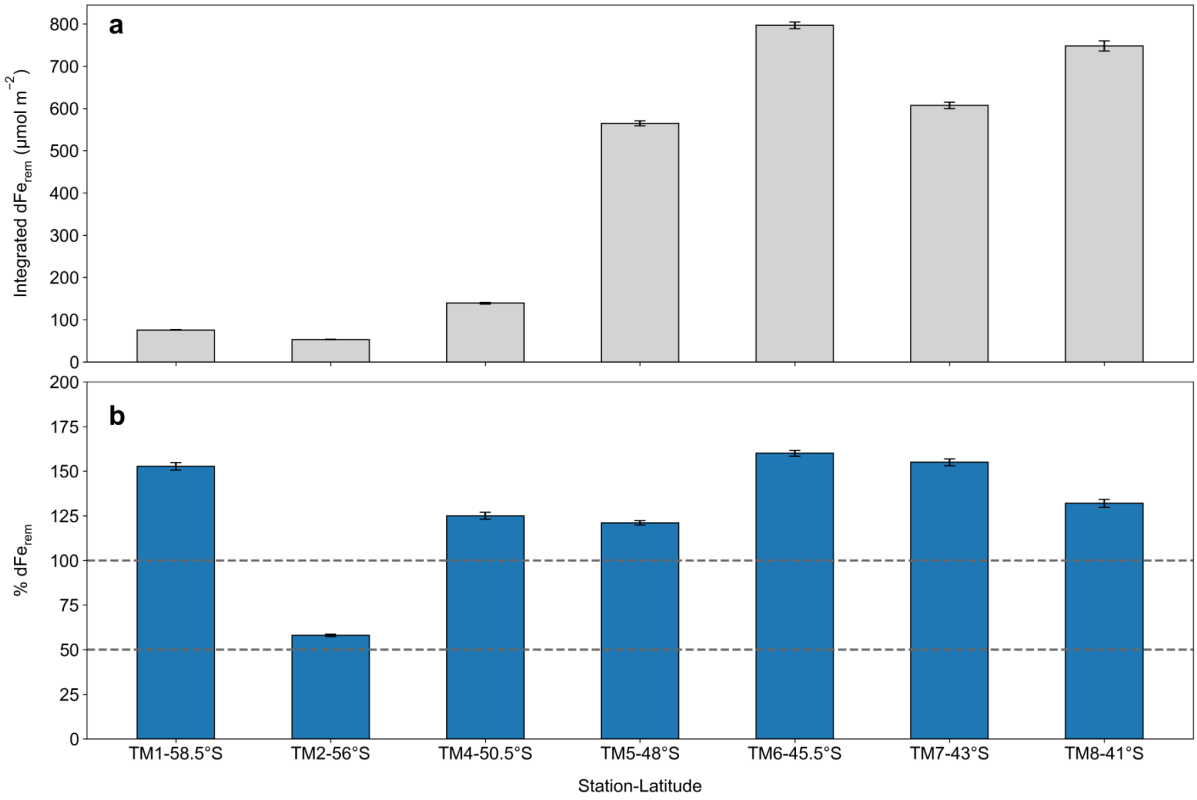

Figure 2.8: The latitudinal trend, south to north, left to right, of (a) the integrated subsurface remineralised dFe stock, as estimated by AOU, with weighted standard deviation as error bars, and (b) the % remineralised dFe of the integrated dFe stock, with dashed line indicating 50% and 100%, with percentage weighted standard deviation as error bars.

The percentage [dFe$_{rem}$] was above 50% at all stations along the transect and also above 100% at all stations, except TM2 (Figure 2.8b). The percentage [dFe$_{rem}$] values ranged from 58 ± 0.7% in the AZ up to 160 ± 1.6% in the SAZ, with no particular latitudinal trend.

2.4 Discussion

2.4.1 SO dFe compilation - open ocean observation comparisons

Data from this study adds to both spatial and temporal gaps highlighted in SO dFe observations, being conducted during winter and in the open waters of the western HNLC SIO, along a transect of the 30°E line from 41°S down to 58.5°S (Figure 2.9). A previous compilation study conducted by Tagliabue et al. (2012) highlighted that better spatial coverage of dFe observations in the SIO will assist in the inter-basin characterisation of dFe fluxes, sources and sinks. Observations in the Indian sector of the SO have mostly been concentrated around the Kerguelen Plateau with very few observations in the western SIO, upstream of the Kerguelen Plateau, which can skew our perception of the general distribution of dFe in the SIO with higher concentrations downstream of the Kerguelen Plateau due to natural fertilisation from the plateau (Blain et al., 2001; 2008; Bowie et al., 2015; Bucciarelli et al., 2001; Tagliabue et al., 2012). Furthermore, observations have been concentrated during austral spring and summer, leaving questions unanswered with regard to the seasonal cycle of dFe distributions (Figure 2.9).

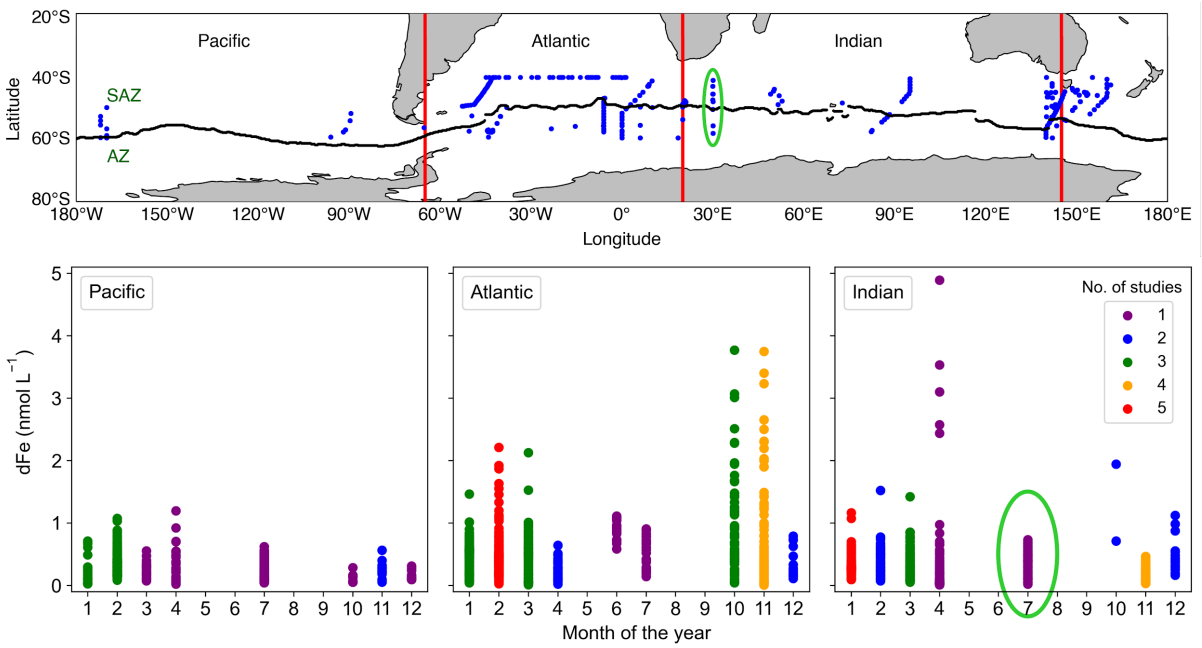

Figure 2.9: A compilation of SO open ocean dFe observations, obtained from Tagliabue et al. (2012), Schlitzer et al. (2018; GEOTRACES IDP2017), Grand et al. (2015), Mtshali et al. (2019), and data from this study (highlighted in the green circle) are displayed as positions (blue) on a cylindrical equal-area projection of the SO, with the three basin cut offs indicated by the red lines, from left to right, Pacific, Atlantic and Indian, and the black line is the mean northern branch of the PF (Tagliabue et al., 2012), acting as the cut off between the SAZ and the AZ (top panel). Using the same compilation data, the plots on the bottom panel indicate the monthly frequency of dFe observations within each SO basin. Observations obtained during this study is highlighted in green circles on both panels.

To facilitate seasonal, zonal and basin comparisons of dFe concentrations in the open waters of the SO, a compilation dataset was constructed (Figure 2.9). The dataset was constructed to only include open ocean observations best suited to the criteria of our study and is not a complete SO dFe compilation. Data from studies done in areas with an immediate continental dFe input were excluded, as were observations within 50 m of the ocean floor to remove any high values due to sediment resuspension and nepheloid layers, as our study did not include these types of measurements. Shelf regions, areas with a bathymetry of < 2000 m (Tagliabue et al., 2012), were also excluded from the compilation. Data was obtained from Tagliabue et al. (2012), the GEOTRACES IDP2017 (Schlitzer et al., 2018), Grand et al. (2015), Mtshali et al. (2019) and this study.

We divided the data into the three SO basins, two zones and depth bins as done by Tagliabue et al. (2012), with modifications. The SO latitudinal cut off was set at 40°S to 60°S, and was divided into the three ocean basins, namely, the Atlantic from 65°W to 20°E, the Indian from

20°E to 145°E and the Pacific from 145°E to 65°W. It was further divided into the AZ and SAZ which were delimited by the northern branch of the PF as determined by Tagliabue et al. (2012). Three depth bins were identified, namely, surface (< 200 m), intermediate (200 - 1000 m) and deep waters (> 1000 m).

Spatially, measurements are concentrated in the Atlantic basin and the Australian sector of the SO, leaving large areas of the Indian and Pacific basins unknown with regard to the biogeochemical cycling of dFe (Figure 2.9). Temporally, observations have been focused on spring and summer months, missing crucial data for the understanding of the winter dFe replenishment dynamics that is hypothesised to initiate spring and summer blooms (Tagliabue et al., 2014), and thereby the seasonal cycle of this micronutrient. Recent winter studies, including this one, have started addressing these observational gaps, however, there is still a long way to go to understand the seasonal distributions and fluxes.

Intra-basin comparisons between the SAZ and AZ dFe concentrations revealed no significant differences in the Indian basin (Figure 2.10; Table A5 and A6). Surface and deep water dFe concentrations in the Pacific basin increased from significantly lower concentrations in the AZ to higher concentrations in the SAZ. In the Atlantic basin surface water dFe concentrations exhibited an opposite trend than observed in the Pacific basin, with significantly higher concentrations in the AZ than in the SAZ. The higher dFe concentrations observed in the AZ versus the SAZ, in the Atlantic basin, is in agreement with the Tagliabue et al. (2012) compilation study; this trend was, however, not observed in the Pacific or Indian basins.

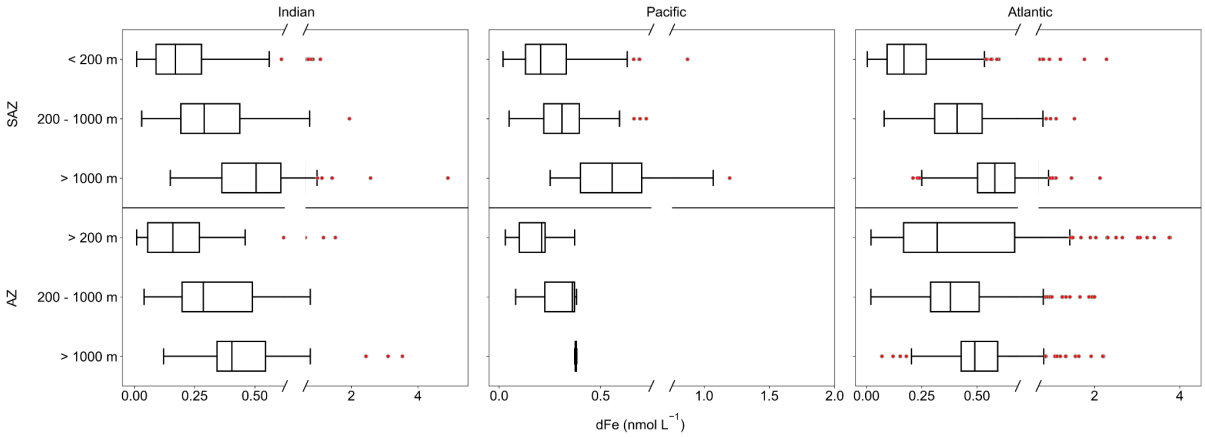

Figure 2.10: Boxplots of the zonal comparison of dFe concentrations from all available dFe data in each of the SO basins, left to right, Indian, Pacific and Atlantic basins. The top panel is the SAZ measurements, and the bottom panel is the AZ measurements, split into surface, intermediate and deep water measurements. Red points are outliers.

When conducting an inter-basin comparison, we observed that SAZ surface waters were only significantly higher in the Pacific when compared to the Indian basin, with no significant differences in these water masses between the Atlantic and the Indian or Pacific basin (Figure 2.10; Table A5 and A6). Median dFe concentrations in SAZ intermediate waters, and AZ surface and intermediate waters increased significantly across basins from the lowest in the Indian basin to the highest in the Atlantic basin. Deep water concentrations were only significantly different between basins in the AZ, increasing from the lowest in the Pacific up to the highest in the Atlantic basin. It must, however, be noted that there are only two observations in the AZ deep waters of the Pacific basin, and this low number of observations could be causing a skewed comparison. In general, dFe concentrations increased with depth and across basins, from the lowest in the Indian basin to the highest in the Atlantic basin (Figure 2.10). The inter-basin trend of higher dFe concentrations in the Atlantic basin was also observed in the compilation study by Tagliabue et al. (2012).

In order to assess if these trends change during austral winter, an inter-basin comparison was done between the three winter studies (Figure 2.11; Ellwood et al., 2008; Mtshali et al., 2019; This study). Winter observations in the Pacific and Atlantic basins were limited to the SAZ, therefore only SAZ data from this study was included in the comparison (Table A5). A

significant increase in dFe concentrations, for all depth bins, was observed from the Pacific to the Atlantic basin (Table A5 and A6), whereas concentrations in surface and intermediate waters of the Indian and Atlantic basins were not significantly different (Table A6). Concentrations in Atlantic deep waters were significantly higher than in deep waters of the Pacific and Indian basins, whereas deep waters in the Indian and Pacific basins were not significantly different during winter (Table A6).

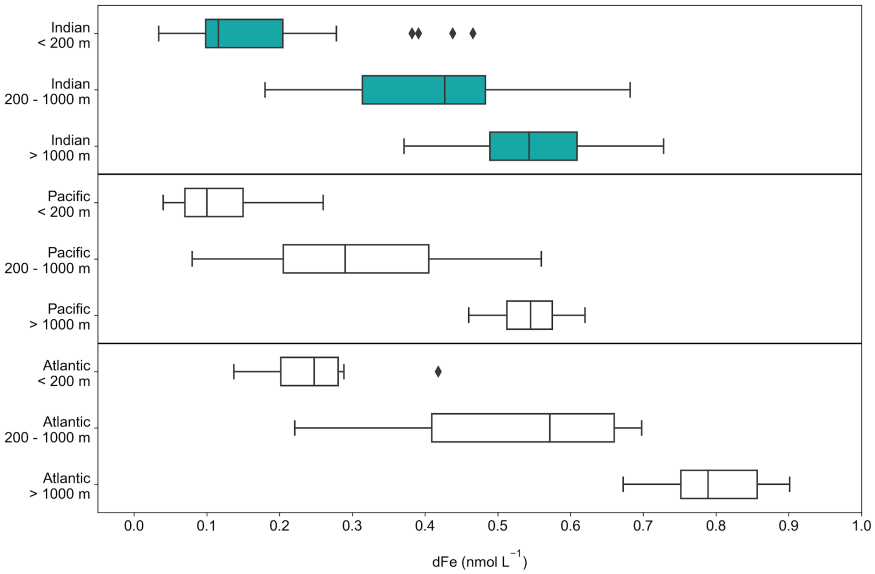

Figure 2.11: Boxplots of dFe concentrations from the winter studies conducted in each of the SO basins, top to bottom, Indian (this study), Pacific (Ellwood et al., 2008) and Atlantic (Mtshali et al., 2019) basins, split into surface, intermediate and deep water concentrations. Data from this study are the filled boxes. Black diamonds are outliers.

Overall, the inter-basin comparison of the three winter studies also exhibited the highest dFe concentrations in the Atlantic basin, as was observed when comparing all available data which is made up of mostly spring and summer observations. During winter, dFe concentrations in the Pacific basin were, however, lower than in the Indian basin, whereas the Pacific basin concentrations were higher in the Indian basin when comparing all available data.

A further seasonal comparison was conducted for each winter study by comparing the winter median dFe concentrations to co-located summer concentrations (Figure 2.12). Data from this study was compared to a study by Grand et al. (2015), conducted during the austral summer of 2008, observations were, however, limited to the upper 1000 m of the water column. The study

conducted in the Pacific basin during winter of 2006 (Ellwood et al., 2008) was compared to studies by Bowie et al. (2009) and Hassler et al. (2014) conducted during the summers of 2007 and 2010, respectively. The study in the Atlantic basin by Mtshali et al. (2019), conducted during winter of 2015, was compared to data from the same study during summer of 2015, and studies by Chever et al. (2010) and Klunder et al. (2011), conducted during the summer of 2008.

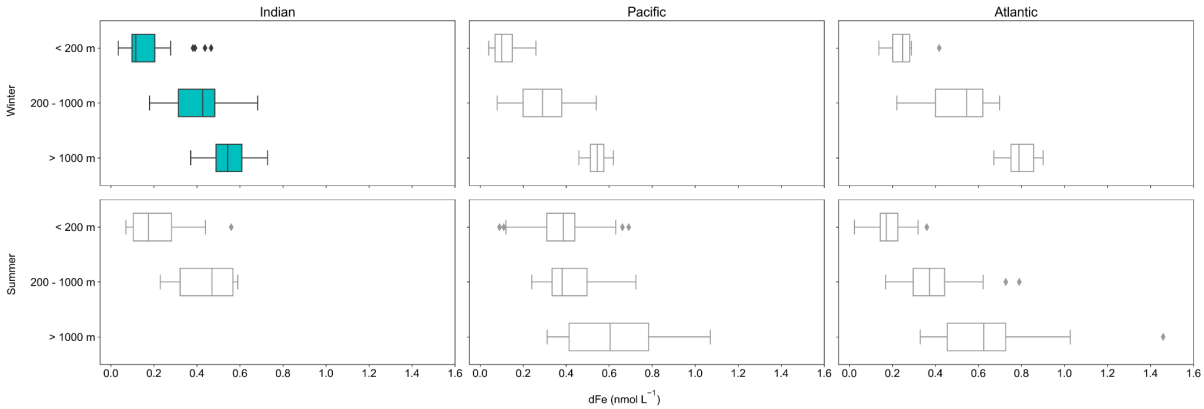

Figure 2.12: Boxplots of the seasonal comparison of dFe concentrations from the winter studies conducted in each of the SO basins, left to right, Indian (this study; Grand et al., 2015), Pacific (Ellwood et al., 2008; Bowie et al., 2009; Hassler et al., 2014) and Atlantic (Mtshali et al., 2019; Chever et al., 2010; Klunder et al., 2011) basins. The top panels show winter measurements, split into surface, intermediate and deep water measurements, the bottom ones show summer measurements at the same location. Data from this study are the filled boxes in the top right-hand plot. Grey diamonds are outliers.

Median concentrations of dFe increased with depth in all three basins for winter and summer observations, except for the summer Pacific values, where the surface and intermediate water median values were nearly identical (Table A5). Median dFe concentrations in the Indian basin were not significantly different between winter and summer observations, in surface or intermediate waters (Table A6). Pacific basin surface and intermediate water median dFe concentrations were surprisingly significantly higher during summer than in winter, whereas deep water median concentrations were not significantly different (Table A6). Although median dFe concentrations in the Atlantic basin were higher in winter than in summer, for all depth bins, only deep waters were significantly higher (Table A6). The seasonal comparison of available data did not reveal any significant surface or intermediate water replenishment at the three winter study locations, during July.

Seasonal, intra- and inter-basin trends in dFe concentrations can be linked to variable magnitudes of fluxes, biological uptake, internal cycling and sources of dFe, as well as water mass age (Table 2.1; De Jong et al., 2012, 2015; Ellwood et al., 2008, Tagliabue et al., 2012). The generally higher dFe concentrations in the Atlantic basin could be explained by relatively larger inputs of dFe via zonal lateral advection (De Jong et al., 2012; Tagliabue et al., 2012) from the Antarctic Peninsula and the islands east thereof (Bowie et al., 2009; Boyd et al., 2005), in conjunction with the hydrodynamics of the Drake passage and the mid-Atlantic ridge facilitating the vertical mixing of dFe-enriched deep waters. The general trend of dFe concentrations across SO basins also suggests that the distribution of dFe concentrations within the SO may be linked to water mass age (Ellwood et al., 2008), where a decrease in dFe concentrations is observed as water masses age from the youngest in the Atlantic basin to the oldest in the Pacific, due to the relatively short residence time of dFe in the marine environment (Croot et al., 2004; Sarthou et al., 2003).

Overall, we did not observe higher dFe concentrations in the AZ when compared to the SAZ, as was observed in the compilation study by Tagliabue et al. (2012). It has also been speculated that biological activity can influence trends in dFe distributions, resulting in higher unused dFe in the AZ due to higher PP in the SAZ than in the AZ (Arrigo et al., 2008; Tagliabue et al., 2012). This theory would align with the intra-basin trend observed in the Atlantic basin, but not in the Pacific or Indian basins. The link to PP was also not observed for the inter-basin comparisons, which was also the case in the study by Tagliabue et al. (2012), showing higher dFe concentrations in the Atlantic basin, a region characterized by higher PP when compared to the Pacific and Indian basins. Variables such as inter-basin hydrothermal inputs and ligand concentration differences can also contribute to the trends we observe in the open waters of the SO (Tagliabue et al., 2012; Thuróczy et al., 2011), there are, however, currently not enough

observations of these variables throughout the open waters of the SO to identify them as driving factors.

The absence of significant differences in the seasonal comparison for the winter studies highlights the lack of surface water dFe replenishment during July, within the open waters of the SO. The expected winter dFe replenishment of surface and intermediate waters might only take place during the transition between winter and spring, closer to bloom initiation, if it occurs at all. Although significant differences were observed between certain data bins of this compilation, there is overlap across all data bins due to the variance within data bins. The question comes to mind that even when there are statistically significant differences, will these differences necessarily result in biogeochemical differences across zones, basins or seasons. It does appear that this is only apparent in the Atlantic basin where PP is notably higher than in the Indian and Pacific basins (Arrigo et al., 2008).

2.4.2 Early winter dFe and macronutrients distributions along 30°E

Early winter dFe concentrations in the HNLC SIO exhibited no surface water replenishment, with strong upper surface water depletion along the transect (Figure 2.5). The depleted dFe concentrations in surface waters observed along the transect resembled end of summer conditions, prior to the expected winter mixing replenishment to surface waters (Mtshali et al., 2019; Tagliabue et al., 2014). Indeed, the negative Fe* values along the transect (Figure 2.6) indicate that during early winter this section of the SO is still strongly Fe limited, in agreement with our seasonal comparisons, which also revealed no surface water dFe replenishment during July. The dominant processes driving the shape of the dFe profiles along the transect are surface depletion due to biological uptake, remineralisation causing an increase in intermediate waters and relatively constant values in deep waters due to scavenging (Figure 1.6) (Boyd and Ellwood, 2010; Bruland and Lohan, 2003; Achterberg et al., 2018). Throughout the water

column, dFe concentrations were subnanomolar, accompanied by high concentrations of macronutrients, characteristic of HNLC open water regions of the SO, throughout the year. Macronutrient (NO_3^-, PO_4^{3-} and $Si(OH)_4$) profiles exhibited the typical SO nutrient distribution, with surface depletion due to biological uptake, increasing with depth due to continuous remineralisation as water masses are subducted (Figure 2.3). Macronutrient distributions exhibited an opposite latitudinal trend to dFe concentration distributions in surface waters, increasing southwards, whereas dFe concentrations increased northwards. In the AZ, NO_3^- and PO_4^{3-} concentrations increased to a maximum in UCDW, due to remineralisation, and decreased slightly in AABW, as this water mass is relatively new, formed by subduction of surface waters and mixing with deep waters along the Antarctic shelf. As continuous remineralisation takes place due to surface export and the subduction of water masses, NO_3^- and PO_4^{3-} concentrations in the SAZ increased up to maximum concentrations in NADW (Figure 2.4a-b, Table A3). $Si(OH)_4$ concentrations increased 10-fold southwards and with depth to maximum concentrations in AABW, due to continental margin inputs along the Antarctic shelf (Figure 2.4c; Table A3). In the STZ, all macronutrient and dFe concentrations were depleted in STSW, characteristic of this oligotrophic region (Sedwick et al., 2002). A subsurface increase in dFe concentrations in the STZ might have been due to a continental margin input from the Mozambique channel via the Agulhas Return Current (ARC) (Figure 2.4; Table A3) (Grand et al., 2015, Pollard and Read, 2001). During a summer study conducted by Grand et al. (2015), along the same transect, similar trends in dissolved and particulate Fe close to the Madagascar continental shelf, an area influenced by the ARC, gave evidence of a sedimentary influence on dFe distributions. In addition to remineralisation, upwelling of nutrient-rich NADW can also contribute to the increase in dFe concentrations observed in intermediate water masses, along the rest of the transect, south of the STF.

A data comparison at crossover stations in the SAZ, between this study and the summer study conducted by Grand et al. (2015), reveals a good agreement for PO_4^{3-} and dFe concentrations between the two studies, within the AAIW density range (Figure 2.13). The deviation in salinity measurements in surface waters, between the two studies, could be due to freshwater inputs from summer rains, resulting in lower salinities during summer when compared to winter. The similarity observed for PO_4^{3-} and dFe concentrations in the mesopelagic zone, between the two studies, conducted nine years apart, supports the hypothesis that remineralisation is the dominant process driving the distribution of these nutrients in intermediate waters of this SO region.

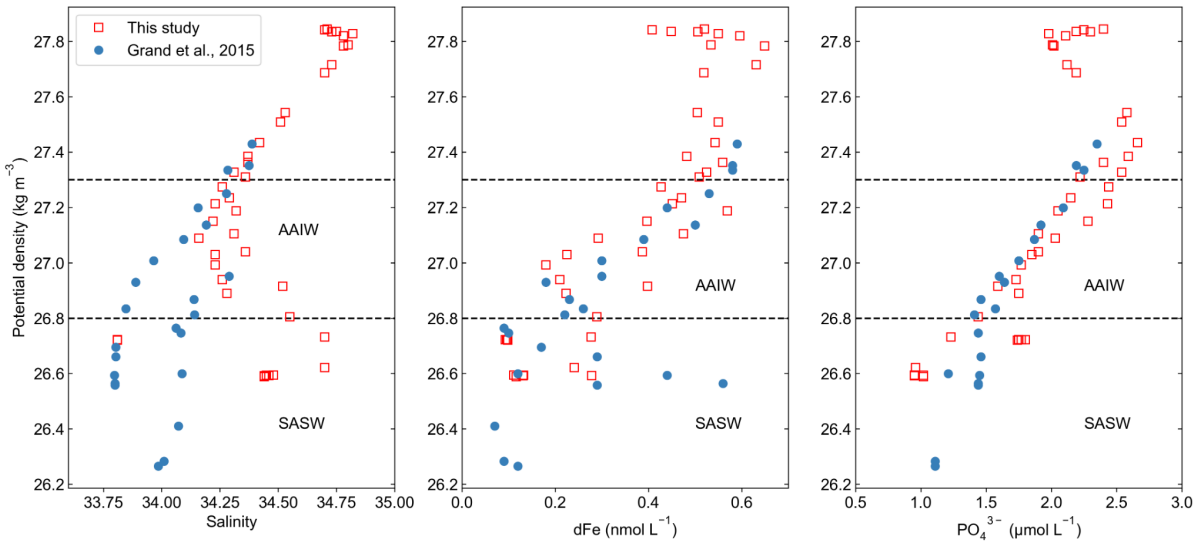

Figure 2.13: Data comparison of crossover stations at 45.5°S and 48°S, from this study (open red squares) and the Grand et al. (2015; filled blue circles), from left to right, salinity, dFe and PO_4^{3-} plotted against potential density. Dashed lines indicate the density ranges for SASW and AAIW water masses.

Profiles of dFe and macronutrient concentrations exhibited peaks within the mesopelagic zone, indicative of subsurface remineralisation, forming the subsurface reservoir which is expected to be accessed via deep winter mixing for the replenishment of the surface mixed layer to initiate the upcoming spring bloom (Tagliabue et al., 2014). In open water HNLC regions of the SO, remineralisation appears to be the dominant process driving the distribution of dFe in intermediate waters, throughout the year (Boyd and Ellwood, 2010; Tagliabue et al., 2019).

2.4.3 Sources, fluxes and remineralisation of dFe during winter

Several sources and processes can affect the distribution of dFe throughout the water column, namely, dust deposition, hydrothermal activity, continental margin runoff, sea ice melt, scavenging and remineralisation. Further physical transport mechanisms such as diapycnal diffusion, vertical Ekman pumping, lateral advection and winter entrainment also affect dFe distributions by supplying or removing dFe from the surface mixed layer (De Jong et al., 2015; Tagliabue et al., 2014; 2017).

We are however not able to discuss all sources and processes with the data from this study and there are a few that can be disregarded due to minimal impact within the area sampled, or a lack of evidence thereof. Other than the subsurface input of dFe by the ARC, there was no further evidence of continental margin dFe inputs along the transect. Sea ice melt can also be disregarded along the transect as our southernmost station was more than 3° (356 km) north of the MIZ (de Jong et al., 2018). It has been previously observed that this localized source dominates as a dFe source within the MIZ but not in the open ocean (De Jong et al., 2015). The lack of spatial variability in surface water dFe concentrations along the transect, except the slight increase from the PF northwards, excludes any obvious evidence of sub-mesoscale features such as eddies or significant atmospheric deposition, along the transect (Lévy et al., 2012); however, the relatively low resolution of sampling could have resulted in the inability to identify these features in our dataset. Dust deposition has previously been thought to be a major source of Fe to surface waters but the vastness of the SO and scarcity of land masses make it a very localized source within the SO (Jickells and Moore, 2015). Recently there have, however, been studies highlighting the significance of soluble anthropogenic Fe aerosols (fossil fuel, biofuel, fire, etc.) which are more soluble than mineral Fe dust, possibly making this a dominant soluble aerosol Fe source to surface waters over large areas of the SO (Conway et al., 2019). A study conducted along the 30°E line during summer, however, found no evidence of significant dust deposition (Grand et al., 2015).

Hydrothermal Fe inputs have previously been thought to be mostly lost close to the source and were therefore not considered as a source of Fe to surface waters (Bruland and Lohan, 2003). This is however no longer the consensus with regard to this source as it has been uncovered that Fe from hydrothermal sources can be transported over large distances due to the stabilisation of dFe by organic ligands (Bennett et al., 2008, Hawkes et al., 2013) and/or the formation of small inorganic nanoparticles in the colloidal size fraction (Yücel et al., 2011; Fitzsimmons et al., 2017), and is therefore a significant component of the oceanic Fe budget (Tagliabue et al., 2010; 2017). The 30°E line crosses over the Southwest Indian Ridge (SWIR), an ultraslow spreading ridge at ~ 14 mm yr^{-1} (Sauter and Cannat, 2010). The spreading rate of a ridge has been linked to the dispersion of hydrothermal inputs (Tagliabue et al., 2010), it would therefore seem unlikely that there would be significant hydrothermal influence along the 30°E line. However, the topography of the SWIR enhances the flow and mixing of deep waters up to the surface and a recent study has found evidence of large phytoplankton blooms fuelled by Fe inputs from hydrothermal vents in this region (Ardyna et al., 2019). Although we did not observe any obvious evidence of hydrothermal inputs in our dFe dataset, inputs from vents along the SWIR could have influenced the preceding spring and summer bloom, thereby impacting the intermediate water remineralisation signal.

To assess the possible pathways of surface mixed layer dFe replenishment, the ferricline depth was determined for each station (Table A2). The ferricline is defined as the subsurface depth (< 1000 m) at which the largest change in dFe concentration is observed with depth (Tagliabue et al., 2014). The replenishment of dFe in intermediate waters via remineralisation in conjunction with the position of the ferricline in relation to the MLD would influence the magnitude of dFe fluxes into the surface mixed layer. During this study the mean ferricline depth along the transect was 314 ± 170 m (mean ± SD, n = 7), whereas the mean MLD was 144 ± 39 m (mean ± SD, n = 7), resulting in a mean separation of 170 ± 144 m (mean ± SD, n

= 7) between the MLD and the ferricline (Figure 2.14). The mean separation between the ferricline and MLD during this study was similar to a previously reported mean separation of 245 m by Tagliabue et al. (2014), representative of observations throughout the SO, in agreement with the finding that there is no seasonal bias on this separation value. The MLD and ferricline were at similar depths at TM2 (56°S), in the AZ, and TM8 (41°S), in the STZ, influencing the relative magnitude of diapycnal diffusion as a surface mixed layer dFe supply mechanism at these stations.

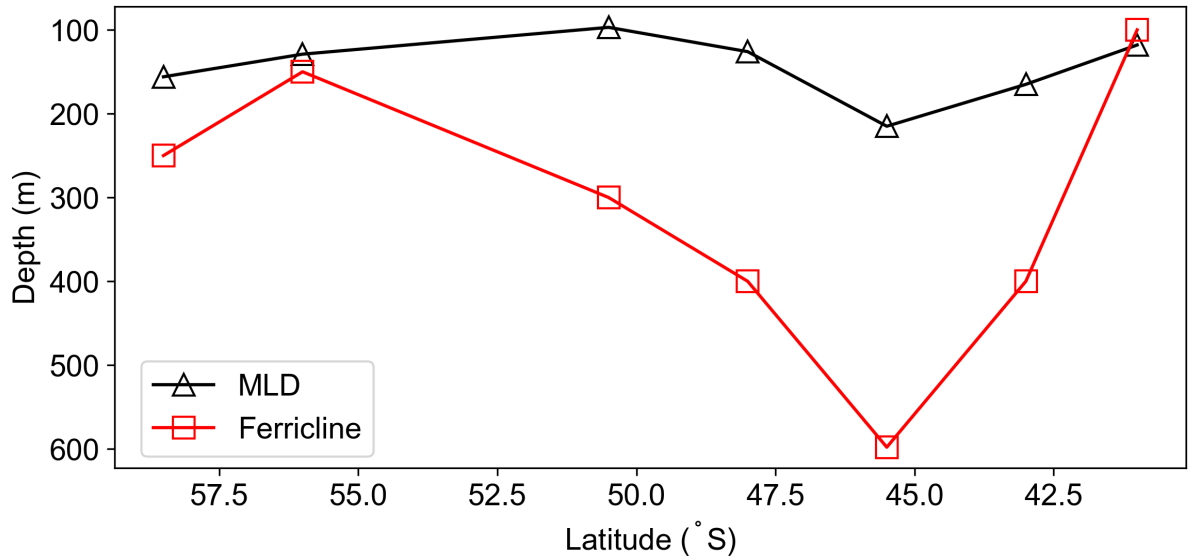

Figure 2.14: A plot of the MLD (black triangles) and the ferricline (red squares) depths at each station sampled along 30°E during this study.

When compiling maximum winter MLD data using ARGO data from 2006 to 2019 along the transect sampled it can be seen that the highest frequency of maximum MLDs occur between July and October (Figure 2.15a). During this study the maximum winter MLD for 2017 occurred either shortly before or after sampling, at the stations along the transect (Figure 2.15b). It was therefore assumed that the dFe distribution observed during this study is the initial state for the annual resupply of dFe to the surface mixed layer. Based on this assumption annual dFe supply fluxes were estimated along the transect, considering several physical pathways.

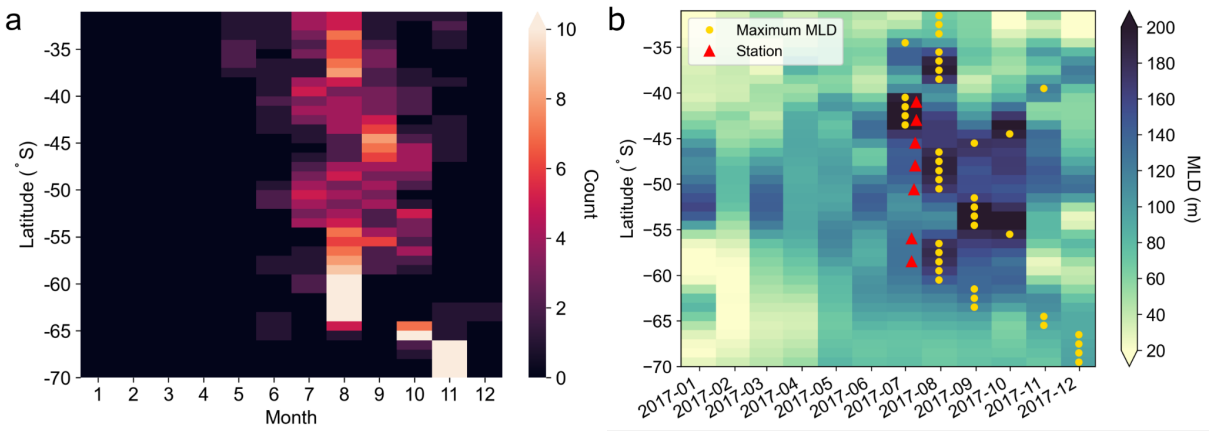

Figure 2.15: Hovmöller plots depicting the distribution of the maximum MLDs along 30°E estimated from ARGO data from 2006 to 2019, (a) the frequency the maximum MLD occurred during each month of the year, spanning the full dataset time frame; and (b) the maximum MLD depth, overlaid with the time of sampling and the month during which the maximum MLD occurred during the year of sampling.

Annual dFe fluxes to the surface mixed layer via winter entrainment, diapycnal diffusion, vertical Ekman pumping and lateral advection into the surface mixed layer were estimated, as described by De Jong et al. (2012) and Tagliabue et al. (2014). The relative magnitudes of fluxes were variable with latitude along the transect (Figure 2.16). Diapycnal diffusion estimates ranged from -10.34 ± 5.70 up to 30.91 ± 11.36 µmol m^{-2} yr^{-1}, with negative values at 50.5°S and 43°S of -0.13 ± 0.71 and -10.34 ± 5.70 µmol m^{-2} yr^{-1}, respectively, making it a loss term at these latitudes. At all other stations diffusion estimates ranged between ~ 2 and 8 µmol m^{-2} yr^{-1}, making diapycnal diffusion a source of dFe to surface waters at these stations. Vertical Ekman pumping fluxes ranged from -4.85 ± 0.94 to 21.75 ± 4.29 µmol m^{-2} yr^{-1}, with negative values in the AZ and at the two northernmost stations, just south of the STF and in the STZ. The estimates in the PFZ and the SAZ were positive, with the highest flux at 48°S. Mixed layer dFe fluxes by lateral advection ranged from -20.89 ± 7.69 up to 0.78 ± 0.29 µmol m^{-2} yr^{-1}, with negative values at all stations except TM2 (56°S) and TM4 (50.5°S), in the AZ. Winter entrainment estimates increased northwards from 4.36 ± 0.04 µmol m^{-2} yr^{-1} at TM1 (58.5°S), in the AZ, up to a maximum of 73.11 ± 2.11 µmol m^{-2} yr^{-1} at TM8 (41°S), in the STZ. The total surface mixed layer dFe fluxes, when summing the estimated fluxes, increased from -1.17 ± 3.50 µmol m^{-2} yr^{-1} at the southernmost station up to 80.76 ± 21.63 µmol m^{-2} yr^{-1} in the STZ.

Total flux estimates increased ~ 3-fold from the AZ up to the SAZ, then dropped down to 13.77 ± 7.40 µmol m^{-2} yr^{-1} at 43°S and increased to the maximum total flux in the STZ.

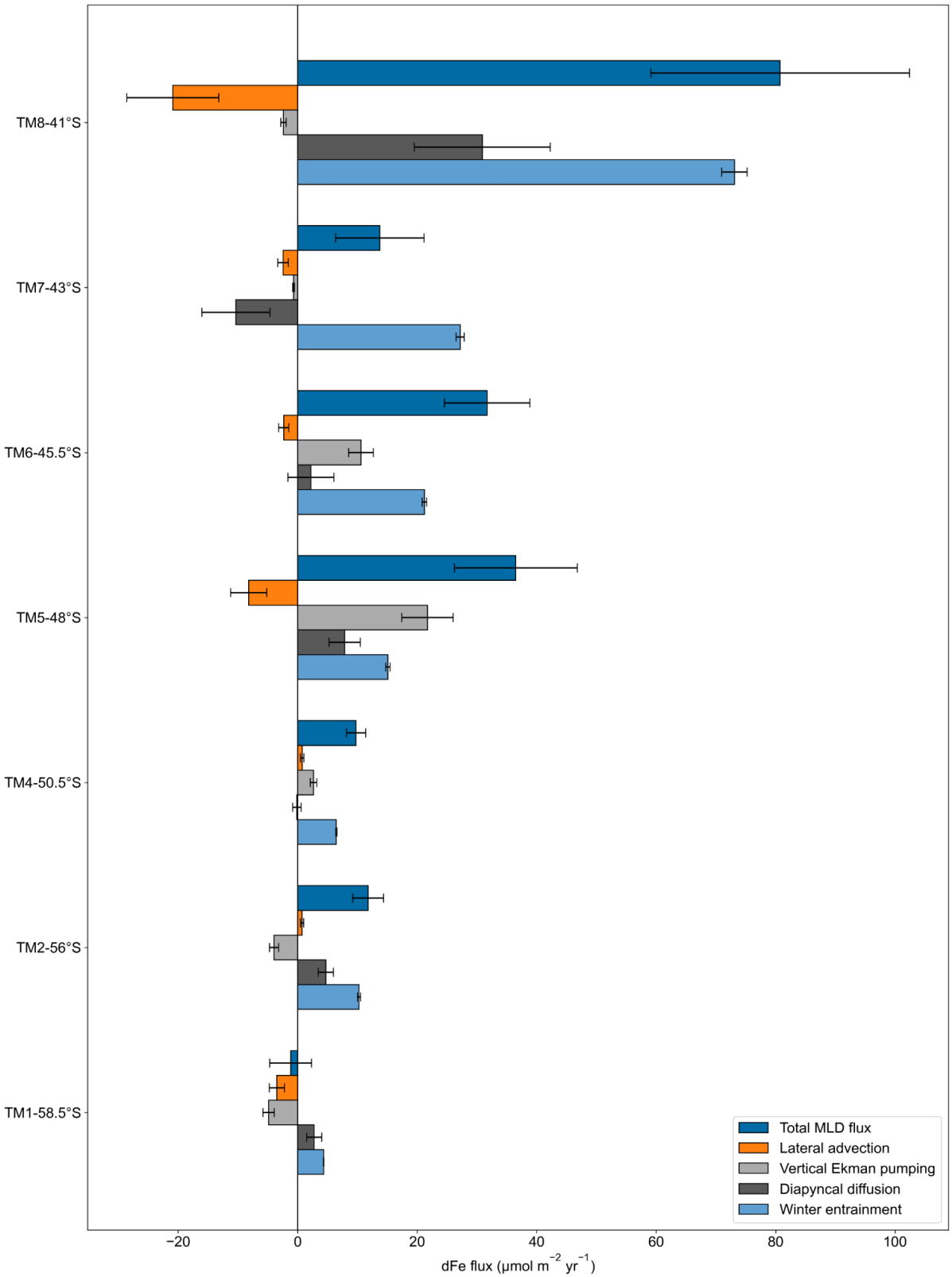

Figure 2.16: Annual fluxes of dFe into the surface mixed layer via winter entrainment (light blue), diapycnal diffusion (dark grey), vertical Ekman pumping (light grey) and lateral advection (orange), and the total MLD fluxes (dark blue) for each station, with standard deviation as error bars.

Winter entrainment was the largest positive flux at most stations along the transect, as has been observed in previous studies (Achterberg et al., 2018, Tagliabue et al., 2014). The northward increase of the winter entrainment flux into the surface mixed layer was consistent with the increase in subsurface dFe concentrations, which would be accessed by the deepening of the winter MLD. The only station where winter entrainment was not the largest flux was TM5 (48°S), where vertical Ekman pumping surpassed winter entrainment. The relatively larger input of dFe by vertical Ekman pumping estimated at 48°S can be linked to the upwelling of NADW. At stations where the separation between the MLD and the ferricline was relatively small (TM1, TM2 and TM8; Figure 2.14), diapycnal diffusion was a relatively larger dFe flux when compared to other fluxes. Diapycnal diffusion was highest at the STZ station (41°S), which can be expected as this was the station at which the ferricline was at the same depth as the MLD and the subsurface waters were dFe-enriched due to the continental margin input via the ARC (Grand et al., 2015). Equatorward lateral advection fluxes were either low or negative at all other stations, making it mostly a loss term along the transect. Vertical Ekman pumping dFe fluxes had a distinct latitudinal trend, increasing from negative values in the AZ to positive (upwelling) values in the PFZ and SAZ, with a maximum value at 48°S, decreasing down to negative values in the STZ, indicating a loss of dFe from the surface mixed layer via downwelling.

Due to the lack of SO winter dFe observations, previous dFe flux estimates have been biased to summer observations. With that being said, our estimates were generally within the same range as previously published fluxes throughout the SO (Table 2.1), with the exception of our STZ station where entrainment and diffusion fluxes were notably higher. The similarity in fluxes across seasons, throughout the SO, and the lack of significant differences in dFe concentrations detected in the seasonal comparison, suggests a weak seasonal cycle with regard to the distributions and vertical fluxes of dFe in the western SIO.

Table 2.1: Fluxes of dFe into the surface mixed layer from this study and various other studies conducted throughout the SO (μmol m^{-2} yr^{-1})

Reference	This study	Tagliabue et al., 2014	De Jong et al., 2015	Bowie et al., 2009	Boyd et al., 2005	Croot et al., 2004	Coale et al., 2005	De Jong et al., 2012
Location/ dFe fluxes	Indian sector	Southern Ocean	Bellingshausen sea	SAZ New Zealand	SAZ New Zealand	Atlantic sector	Ross Sea	Antarctic Peninsula and Atlantic sector
Winter entrainment	4.4 - 73.1	9.1 - 33	-	-	-	-	-	-
Diapycnal diffusion	-10.3 - 30.9	1.2 - 3.6	0 - 1.1	-11.3 - 2.6	5.5	12.8	-	0.1 - 2.9
Vertical pumping	-4.9 - 21.7	-1.9 - 0.4	3.3 - 33.6	0 - 17.2	-	11.3	9.9	1.1 - 47.1
Lateral advection	-20.9 - 0.8	-	1.8 - 177.4	8.8 - 45.3	0.0	-	1.8	3.3 - 131.4

All dFe fluxes into the surface mixed layer are dependent on the subsurface dFe concentrations and a dominant process in these intermediate waters of the SO is remineralisation, which is believed to replenish the winter reservoir in HNLC regions (Tagliabue et al., 2014). In situ integrated subsurface dFe concentrations exhibited the same latitudinal trend but all significantly lower than the corresponding maximum attainable remineralised dFe estimates, with the exception of the station at 56°S. All percentages of remineralised dFe were well above 100%, indicating the presence of a significant sink, which can be assumed to be scavenging. The lowest percentage remineralised Fe at 56°S can be an indication of a subsurface source other than remineralisation at this latitude. These estimates of remineralised dFe support the hypothesis that phytoplankton are heavily reliant on remineralisation and as the bloom season progresses remineralisation becomes increasingly crucial in Fe-limited regions of the open SO (Tagliabue et al., 2014). The determination of remineralised dFe concentrations is, however, dependent on Fe:P:O_2 cellular ratios, which were assumed to be constant along the transect (Ito

and Follow, 2005; Twining et al., 2014). It cannot, however, be disregarded that deviations in cellular ratios can introduce errors in the estimates of remineralised dFe. Aside from the deviations of cellular ratios, scavenging is also a significant process which does not influence PO_4^{3-} distributions but does affect dFe (see section 2.2.5). A study in the Southern Pacific Ocean by Tagliabue et al. (2019) has, however, identified that over half of the dFe concentration measured in intermediate waters is set by internal cycling (remineralisation and scavenging), with the remainder being controlled by physical transport (subduction/lateral advection). Due to dFe being drawn down to very low levels in regions of intermediate water formation in the SO, internal cycling has a larger imprint on the interior dFe concentrations than physical transport (Tagliabue et al., 2019). It can therefore be assumed that our estimates of maximum attainable remineralised Fe are acceptable estimates, prior to the correction for scavenging, which has yet to be accurately quantified within the SO (Tagliabue et al., 2019). Assuming 100% remineralisation of Fe in the mesopelagic zone along the transect of this study, it can be assumed that a minimum of 20 to 60% of subsurface remineralised Fe has been lost via scavenging (Figure 2.8).

Considering the strong correlations obtained from the linear regressions of subsurface dFe to AOU, these regressions can be used to estimate the Fe:C (μmol mol^{-1}) ratios of remineralised particles (Achterberg et al., 2018). The slopes of dFe:AOU ranged from 0.0012 ± 0.0003 to 0.0037 ± 0.0003 nmol μmol^{-1} (Figure A1). Using the AOU:C ratio of 1.39 (Anderson, 1995), we estimated a range of Fe:C ratios of 1.7 ± 0.4 to 5.1 ± 0.4 μmol mol^{-1} (3.55 ± 1.21 μmol mol^{-1}, n = 7; mean ± SD), in agreement with reported SO Fe:C ratios of 1.5 - 8.0 μmol mol^{-1} (Abraham et al., 2000; Fung et al., 2000; Sunda, 1997; Sarthou et al., 2008; Tagliabue et al., 2019). The mean dFe:PO_4^{3-} (0.37 ± 0.19 mmol mol^{-1}, n = 7; mean ± SD) from linear regressions from this study (Figure A2) is also similar to the literature value of cellular Fe:P (0.54 mmol mol^{-1}; Twining et al., 2014), which is evidence that remineralisation was in fact the dominant

process, in the mesopelagic zone of this region at the time this study, especially since this ratio can also be affected by many other environmental factors.

2.5 Conclusion

The compilation dataset of open water SO dFe observations revealed spatial and temporal gaps, of which recent winter studies, including this study, have started addressing (Figure 2.9). A comparison of all available dFe data exhibits a general increase in concentrations from surface to depth, and from the Indian and Pacific basins to the highest concentrations in the Atlantic basin. Significant differences between the SAZ and the AZ were only detected in data from the Pacific and Atlantic basins. In the Pacific basin surface and deep water concentrations were significantly higher in the SAZ than the AZ, and in the Atlantic basin surface water concentrations were higher in the AZ than in the SAZ (Figure 2.10). Winter observations in the SAZ also revealed an increase in dFe concentrations from the Pacific basin to the highest concentrations in the Atlantic basin (Figure 2.11). Seasonal comparisons of dFe concentrations did not reveal any significant surface water replenishment during July, at the sites of the three SO winter studies, on the contrary winter dFe concentrations in the Pacific and Indian basins were lower than co-located summer observations (Figure 2.12). The general basin scale trend in dFe concentrations is in agreement with higher inputs in the Atlantic basin via large zonal lateral advection from the Western Antarctic Peninsula, and also that dFe concentrations can be linked to water mass age (Table 2.1; De Jong et al., 2012, 2015; Ellwood et al., 2008). The biogeochemical significance of these differences can, however, only be observed by the higher PP in the Atlantic basin, when compared to the rest of the SO (Arrigo et al., 2008).

Early winter dFe distributions in the open waters of the Southern Indian Ocean resembled end of summer distributions with pronounced surface depletion, indicative of end of bloom limiting conditions. There was no obvious evidence of dust deposition, hydrothermal, sea ice or continental margin inputs along the transect, except for a subsurface input in the STZ (41°S) from the Mozambique channel via the ARC. Median dFe concentrations increased significantly

northwards and with depth, across water masses, whereas macronutrients increased southwards (Figure 2.4a-d). The observations in the STZ were slightly different compared to the rest of the transect, south of the STF. In the STZ surface macronutrient and dFe concentrations were depleted, making this region macronutrient and Fe-limited. In general, the ferricline was deeper than the MLD at most stations, with the largest separation in the SAZ. In the AZ and STZ the separation between the ferricline and MLD was less pronounced, and in the STZ the ferricline MLD were at similar depths (Figure 2.14). The latitudinal change in the position of the ferricline in relation to the MLD influenced the magnitude of surface mixed layer dFe flux estimates along the transect.

Various dFe fluxes into the surface mixed layer were estimated, namely, winter entrainment, diapycnal diffusion, vertical Ekman pumping and lateral advection (Figure 2.16). As has been observed in previous studies (Achterberg et al., 2018; Tagliabue et al., 2014), winter entrainment was generally the largest surface mixed layer dFe input pathway along the transect, increasing northwards to a maximum in the STZ. Fluxes in the STZ were noticeably higher than the rest of the transect, which was not unexpected because of the continental margin influence in the subsurface waters at this latitude. Diapycnal diffusion, previously thought to be a rather insignificant vertical supply of dFe (Achterberg., 2018; De Jong et al., 2015; Tagliabue et al., 2014), was relatively larger than other fluxes at stations in the AZ and STZ, where the separation between the ferricline and the MLD was relatively small. In the PFZ vertical Ekman pumping overtook winter entrainment as the largest flux of dFe into the surface mixed layer, which could be due to the upwelling of NADW in this region. Overall, fluxes were generally in the same range as previous studies in the SO (Table 2.1), which were mostly determined using summer observations, indicating that the supply of dFe to the surface mixed layer could lack a distinct pulse of resupply but rather be a somewhat steady-state of year-round supply and removal.

Remineralisation has previously been identified as a dominant source of subsurface dFe replenishment in open waters of the SO, where external inputs are minimal (Tagliabue et al., 2014; 2019). Our estimates exhibit a steady increase in subsurface remineralised dFe stocks northwards from the AZ, and that up to 100% of subsurface dFe is possibly remineralised, with the exception of the station at 56°S where there could be an unaccounted for subsurface input. These estimates also indicate that a possible loss of at least 20 to 60% of subsurface dFe via scavenging is detected during winter. Estimates of Fe:C (3.55 ± 1.21 μmol mol^{-1}, n = 7; mean ± SD) and Fe:P (0.37 ± 0.19 mmol mol^{-1}, n = 7; mean ± SD) ratios determined during this study, from subsurface dissolved phase observations, are in good agreement with published SO phytoplankton cellular ratios. These ratios give further evidence that remineralisation is the dominant process in the mesopelagic zone of the open waters of the SIO during winter. It can be proposed that the magnitude of subsurface replenishment of dFe via remineralisation influences dFe fluxes into the surface mixed layer, which in turn will sustain primary production in the coming bloom season.

References

Abraham, E. R., Law, C. S., Boyd, P. W., Lavender, S. J., Maldonado, M. T., & Bowie, A. R. (2000). Importance of stirring in the development of an iron-fertilized phytoplankton bloom. *Nature 2000 407:6805*, *407*(6805), 727–730. https://doi.org/10.1038/35037555

Achterberg, E. P., Steigenberger, S., Marsay, C. M., Lemoigne, F. A. C., Painter, S. C., Baker, A. R., Connelly, D. P., Moore, C. M., Tagliabue, A., & Tanhua, T. (2018). Iron Biogeochemistry in the High Latitude North Atlantic Ocean. *Scientific Reports*, *8*(1), 1–15. https://doi.org/10.1038/s41598-018-19472-1

Anderson L, A. (1995). On the hydrogen and oxygen content of marine phytoplankton. *Deep Sea Research, Part I*, *42*(9), 1675–1680.

Anilkumar, N., & Sabu, P. (2017). Physical process influencing the ecosystem of the indian sector of southern ocean-An overview. *Proceedings of the Indian National Science Academy*, *83*(2), 363–376. https://doi.org/10.16943/ptinsa/2017/48960

Ardyna, M., Lacour, L., Sergi, S., d'Ovidio, F., Sallée, J. B., Rembauville, M., Blain, S., Tagliabue, A., Schlitzer, R., Jeandel, C., Arrigo, K. R., & Claustre, H. (2019). Hydrothermal vents trigger massive phytoplankton blooms in the Southern Ocean. *Nature Communications*, *10*(1), 1–8. https://doi.org/10.1038/s41467-019-09973-6

Argo (2000). Argo float data and metadata from Global Data Assembly Centre (Argo GDAC). *SEANOE*. https://doi.org/10.17882/42182

Arrigo, K. R., Dijken, G. L. van, & Bushinsky, S. (2008). Primary production in the Southern Ocean, 1997–2006. *Journal of Geophysical Research: Oceans*, *113*(C8), 8004. https://doi.org/10.1029/2007JC004551

Barbur, V. A., Montgomery, D. C., & Peck, E. A. (1994). Introduction to Linear Regression Analysis. *The Statistician*, *43*(2), 339. https://doi.org/10.2307/2348362

Bennett, S. A., Achterberg, E. P., Connelly, D. P., Statham, P. J., Fones, G. R., & German, C. R. (2008). The distribution and stabilisation of dissolved Fe in deep-sea hydrothermal plumes. *Earth and Planetary Science Letters*, *270*(3–4), 157–167. https://doi.org/10.1016/j.epsl.2008.01.048

Blain, S., Sarthou, G., & Laan, P. (2008). Distribution of dissolved iron during the natural iron-fertilization experiment KEOPS (Kerguelen Plateau, Southern Ocean). *Deep-Sea Research Part II: Topical Studies in Oceanography*, *55*(5–7), 594–605. https://doi.org/10.1016/j.dsr2.2007.12.028

Blain, S., Tréguer, P., Belviso, S., Bucciarelli, E., Denis, M., Desabre, S., Fiala, M., Martin Jézéquel, V., Le Fèvre, J., Mayzaud, P., Marty, J. C., & Razouls, S. (2001). A biogeochemical study of the island mass effect in the context of the iron hypothesis: Kerguelen Islands, Southern Ocean. *Deep Sea Research Part I: Oceanographic Research Papers*, *48*(1), 163–187. https://doi.org/10.1016/S0967-0637(00)00047-9

Bowie, A. R., Lannuzel, D., Remenyi, T. A., Wagener, T., Lam, P. J., Boyd, P. W., Guieu, C., Townsend, A. T., & Trull, T. W. (2009). Biogeochemical iron budgets of the Southern Ocean south of Australia: Decoupling of iron and nutrient cycles in the subantarctic zone by the summertime supply. *Global Biogeochemical Cycles*, *23*(4), 1–14. https://doi.org/10.1029/2009GB003500

Bowie, A. R., Van Der Merwe, P., Quéroué, F., Trull, T., Fourquez, M., Planchon, F., Sarthou, G., Chever, F., Townsend, A. T., Obernosterer, I., Sallée, J. B., & Blain, S. (2015). Iron budgets for three distinct biogeochemical sites around the Kerguelen Archipelago (Southern Ocean) during the natural fertilisation study, KEOPS-2. *Biogeosciences*, *12*(14), 4421–4445. https://doi.org/10.5194/bg-12-4421-2015

Boyd, P. W., & Ellwood, M. J. (2010). The biogeochemical cycle of iron in the ocean. *Nature Geoscience*, *3*(10), 675–682. https://doi.org/10.1038/ngeo964

Boyd, P. W., Ellwood, M. J., Tagliabue, A., & Twining, B. S. (2017). Biotic and abiotic retention, recycling and remineralization of metals in the ocean. *Nature Geoscience*, *10*(3), 167–173. https://doi.org/10.1038/ngeo2876

Boyd, P. W., Law, C. S., Hutchins, D. A., Abraham, E. R., Croot, P. L., Ellwood, M., Frew, R. D., Hadfield, M., Hall, J., Handy, S., Hare, C., Higgins, J., Hill, P., Hunter, K. A., LeBlanc, K., Maldonado, M. T., McKay, R. M., Mioni, C., Oliver, M., … Wilhelm, S. W. (2005). FeCycle: Attempting an iron biogeochemical budget from a mesoscale SF6 tracer experiment in unperturbed low iron waters. *Global Biogeochemical Cycles*, *19*(4), 1–13. https://doi.org/10.1029/2005GB002494

Bruland, K. W., & Lohan, M. C. (2003). Controls of Trace Metals in Seawater. *Treatise on Geochemistry*, *6–9*, 23–47. https://doi.org/10.1016/B0-08-043751-6/06105-3

Bucciarelli, E., Blain, S., & Tréguer, P. (2001). Iron and Manganese in the wake of the Kerguelen Islands (Southern Ocean). *Marine Chemistry*, *73*(1), 21–36. https://doi.org/10.1016/S0304-4203(00)00070-0

Chever, F., Bucciarelli, E., Sarthou, G., Speich, S., Arhan, M., Penven, P., & Tagliabue, A. (2010). Physical speciation of iron in the Atlantic sector of the Southern Ocean

along a transect from the subtropical domain to the Weddell Sea Gyre. *Journal of Geophysical Research: Oceans*, *115*(10), 1–15. https://doi.org/10.1029/2009JC005880

Cisewski, B., Strass, V. H., & Prandke, H. (2005). Upper-ocean vertical mixing in the Antarctic Polar Front Zone. *Deep-Sea Research Part II: Topical Studies in Oceanography*, *52*(9-10 SPEC. ISS.), 1087–1108. https://doi.org/10.1016/j.dsr2.2005.01.010

Coale, K. H., Gordon, R. M., & Wang, X. (2005). The distribution and behavior of dissolved and particulate iron and zinc in the Ross Sea and Antarctic circumpolar current along 170°W. *Deep-Sea Research Part I: Oceanographic Research Papers*, *52*(2), 295–318. https://doi.org/10.1016/j.dsr.2004.09.008

Conway, T. M., Hamilton, D. S., Shelley, R. U., Aguilar-Islas, A. M., Landing, W. M., Mahowald, N. M., & John, S. G. (2019). Tracing and constraining anthropogenic aerosol iron fluxes to the North Atlantic Ocean using iron isotopes. *Nature Communications*, *10*(1), 1–10. https://doi.org/10.1038/s41467-019-10457-w

Croot, P. L., Andersson, K., Öztürk, M., & Turner, D. R. (2004). The distribution and speciation of iron along 6°E in the Southern Ocean. *Deep-Sea Research Part II: Topical Studies in Oceanography*, *51*(22–24), 2857–2879. https://doi.org/10.1016/j.dsr2.2003.10.012

Cutter, G., Casciotti, K., Croot, P., Geibert, W., Heimbürger, L.-E., Lohan, M., Planquette, H., & van de Flierdt, T. (2017). *Sampling and Sample-handling Protocols for GEOTRACES Cruises. Version 3, August 2017.* http://www.geotraces.org/images/stories/documents/intercalibration/Cookbook.pdf

de Boyer Montégut, C., Madec, G., Fischer, A. S., Lazar, A., & Iudicone, D. (2004). Mixed layer depth over the global ocean: An examination of profile data and a profile-based climatology. *Journal of Geophysical Research C: Oceans*, *109*(12), 1–20. https://doi.org/10.1029/2004JC002378

De Jong, J., Schoemann, V., Lannuzel, D., Croot, P., De Baar, H., & Tison, J. L. (2012). Natural iron fertilization of the Atlantic sector of the Southern Ocean by continental shelf sources of the Antarctic Peninsula. *Journal of Geophysical Research: Biogeosciences*, *117*(1). https://doi.org/10.1029/2011JG001679

De Jong, J. T. M., Stammerjohn, S. E., Ackley, S. F., Tison, J. L., Mattielli, N., & Schoemann, V. (2015). Sources and fluxes of dissolved iron in the Bellingshausen Sea (West Antarctica): The importance of sea ice, icebergs and the continental margin. *Marine Chemistry*, *177*, 518–535. https://doi.org/10.1016/j.marchem.2015.08.004

de Jong, E., Vichi, M., Mehlmann, C. B., Eayrs, C., De Kock, W., Moldenhauer, M., & Audh, R. R. (2018). Sea Ice conditions within the Antarctic Marginal Ice Zone in winter 2017, onboard the SA Agulhas II. *University of Cape Town, PANGAEA*. https://doi.org/https://doi.org/10.1594/PANGAEA.885211

Egan, L. (2008). Determination of nitrate and/or nitrite in brackish or seawater by flow injection analysis. *Quickchem Method® 31-107-04-1-C. Lachat Instruments, USA.* https://doi.org/10.4319/lo.1983.28.6.1260.

Ehrhardt, M. (Manfred), Grasshoff, K., Kremling, K. (Klaus), & Almgren, T. (Eds.). (1983). *Methods of seawater analysis / edited by K. Grasshoff, M. Ehrhardt, K. Kremling ; with contributions by T. Almgren ... [et al.]*. Verlag Chemie.

Ellwood, M. J., Boyd, P. W., & Sutton, P. (2008). Winter-time dissolved iron and nutrient distributions in the Subantarctic Zone from 40-52S; 155-160E. *Geophysical Research Letters*, *35*(11), 2–7. https://doi.org/10.1029/2008GL033699

Fitzsimmons, J. N., John, S. G., Marsay, C. M., Hoffman, C. L., Nicholas, S. L., Toner, B. M., German, C. R., & Sherrell, R. M. (2017). Iron persistence in a distal hydrothermal plume supported by dissolved-particulate exchange. *Nature Geoscience*, *10*(3), 195–201. https://doi.org/10.1038/ngeo2900

Fung, I. Y., Meyn, S. K., Tegen, I., Doney, S. C., John, J. G., & Bishop, J. K. B. (2000). Iron supply and demand in the upper ocean. *Global Biogeochemical Cycles*, *14*(1), 281–295. https://doi.org/10.1029/1999GB900059

Gill, A. E. (1982). *Atmosphere-ocean dynamics*. NEW YORK, U.S.A., ACADEMIC PRESS INC. https://doi.org/https://doi.org/10.1016/0141-1187(83)90039-1

Grand, M. M., Measures, C. I., Hatta, M., Morton, P. L., Barrett, P., Milne, A., Resing, J. A., & Landing, W. M. (2015). The impact of circulation and dust deposition in controlling the distributions of dissolved Fe and Al in the south Indian subtropical gyre. *Marine Chemistry*, *176*, 110–125. https://doi.org/10.1016/j.marchem.2015.08.002

Hassler, C. S., Ridgway, K. R., Bowie, A. R., Butler, E. C. V., Clementson, L. A., Doblin, M. A., Davies, D. M., Law, C., Ralph, P. J., Van Der Merwe, P., Watson, R., & Ellwood, M. J. (2014). Primary productivity induced by iron and nitrogen in the Tasman Sea: An overview of the PINTS expedition. *Marine and Freshwater Research*, *65*(6), 517–537. https://doi.org/10.1071/MF13137

Hawkes, J. A., Connelly, D. P., Gledhill, M., & Achterberg, E. P. (2013). The stabilisation and transportation of dissolved iron from high temperature hydrothermal vent systems. *Earth and Planetary Science Letters*, *375*, 280–290. https://doi.org/10.1016/J.EPSL.2013.05.047

Ito, T., & Follows, M. J. (2005). Preformed phosphate, soft tissue pump and atmospheric CO2. *Journal of Marine Research*, *63*(4), 813–839. https://doi.org/10.1357/0022240054663231

Ito, T., Follows, M. J., & Boyle, E. A. (2004). Is AOU a good measure of respiration in the oceans? *Geophysical Research Letters*, *31*(17), 1–4. https://doi.org/10.1029/2004GL020900

Janssen, D. J., Sieber, M., Ellwood, M. J., Conway, T. M., Barrett, P. M., Chen, X., de Souza, G. F., Hassler, C. S., & Jaccard, S. L. (2020). Trace metal and nutrient dynamics across broad biogeochemical gradients in the Indian and Pacific sectors of the Southern Ocean. *Marine Chemistry*, *221*(August 2019), 103773. https://doi.org/10.1016/j.marchem.2020.103773

Jickells, T. D., An, Z. S., Andersen, K. K., Baker, A. R., Bergametti, C., Brooks, N., Cao, J. J., Boyd, P. W., Duce, R. A., Hunter, K. A., Kawahata, H., Kubilay, N., LaRoche, J., Liss, P. S., Mahowald, N., Prospero, J. M., Ridgwell, A. J., Tegen, I., & Torres, R. (2005). Global iron connections between desert dust, ocean biogeochemistry, and climate. In *Science* (Vol. 308, Issue 5718, pp. 67–71). American Association for the Advancement of Science. https://doi.org/10.1126/science.1105959

Jickells, T., & Moore, C. M. (2015). The Importance of Atmospheric Deposition for Ocean Productivity. *Annual Review of Ecology, Evolution, and Systematics*, *46*, 481–501. https://doi.org/10.1146/annurev-ecolsys-112414-054118

Klunder, M. B., Laan, P., Middag, R., De Baar, H. J. W., & van Ooijen, J. C. (2011). Dissolved iron in the Southern Ocean (Atlantic sector). *Deep-Sea Research Part II: Topical Studies in Oceanography*, *58*(25–26), 2678–2694. https://doi.org/10.1016/j.dsr2.2010.10.042

Kokoska, S., & Zwillinger, D. (2000). CRC Standard Probability and Statistics Tables and Formulae, Student Edition. In *CRC Standard Probability and Statistics Tables and Formulae, Student Edition*. https://doi.org/10.1201/b16923

Lagerström, M. E., Field, M. P., Séguret, M., Fischer, L., Hann, S., & Sherrell, R. M. (2013). Automated on-line flow-injection ICP-MS determination of trace metals (Mn, Fe, Co, Ni, Cu and Zn) in open ocean seawater: Application to the GEOTRACES program. *Marine Chemistry*, *155*, 71–80. https://doi.org/10.1016/j.marchem.2013.06.001

Lévy, M., Ferrari, R., Franks, P. J. S., Martin, A. P., & Rivière, P. (2012). Bringing physics to life at the submesoscale. *Geophysical Research Letters*, *39*(14). https://doi.org/10.1029/2012GL052756

Martin, J. H. (1990). GLACIAL-INTERGLACIAL CO 2 CHANGE: THE IRON HYPOTHESIS. In *PALEOCEANOGRAPHY* (Vol. 5, Issue 1).

Martin, J. H., Fitzwater, S. E., & Gordon, R. M. (1990). Iron deficiency limits phytoplankton growth in Antarctic waters. *Global Biogeochemical Cycles*, *4*(1), 5–12. https://doi.org/10.1029/GB004i001p00005

Moore, J. K., Doney, S. C., Glover, D. M., & Fung, I. Y. (2001). Iron cycling and nutrient-limitation patterns in surface waters of the world ocean. *Deep-Sea Research Part II: Topical Studies in Oceanography*, *49*(1–3), 463–507. https://doi.org/10.1016/S0967-0645(01)00109-6

Mtshali, T. N., van Horsten, N. R., Thomalla, S. J., Ryan-Keogh, T. J., Nicholson, S. A., Roychoudhury, A. N., Bucciarelli, E., Sarthou, G., Tagliabue, A., & Monteiro, P. M. S. (2019). Seasonal Depletion of the Dissolved Iron Reservoirs in the Sub-Antarctic Zone of the Southern Atlantic Ocean. *Geophysical Research Letters*, *46*(8), 4386–4395. https://doi.org/10.1029/2018GL081355

Orsi, A. H., Whitworth, T., & Nowlin, W. D. (1995). On the meridional extent and fronts of the Antarctic Circumpolar Current. *Deep-Sea Research Part I*, *42*(5), 641–673. https://doi.org/10.1016/0967-0637(95)00021-W

Parekh, P., Follows, M. J., & Boyle, E. A. (2005). Decoupling of iron and phosphate in the global ocean. *Global Biogeochemical Cycles*, *19*(2), 1–16. https://doi.org/10.1029/2004GB002280

Pollard, R. T., & Read, J. F. (2001). Circulation pathways and transports of the Southern Ocean in the vicinity of the Southwest Indian Ridge. *Journal of Geophysical Research: Oceans*, *106*(C2), 2881–2898. https://doi.org/10.1029/2000jc900090

Rio, M. H., Guinehut, S., & Larnicol, G. (2011). New CNES-CLS09 global mean dynamic topography computed from the combination of GRACE data, altimetry, and in situ measurements. *Journal of Geophysical Research: Oceans*, *116*(7), 1–25. https://doi.org/10.1029/2010JC006505

Sarthou, G., Baker, A. R., Blain, S., Achterberg, E. P., Boye, M., Bowie, A. R., Croot, P., Laan, P., De Baar, H. J. W., Jickells, T. D., & Worsfold, P. J. (2003). Atmospheric iron deposition and sea-surface dissolved iron concentrations in the eastern Atlantic Ocean. *Deep-Sea Research Part I: Oceanographic Research Papers*, *50*(10–11), 1339–1352. https://doi.org/10.1016/S0967-0637(03)00126-2

Sarthou, G., Vincent, D., Christaki, U., Obernosterer, I., Timmermans, K. R., & Brussaard, C. P. D. (2008). The fate of biogenic iron during a phytoplankton bloom induced by natural fertilisation: Impact of copepod grazing. *Deep Sea Research Part II: Topical Studies in Oceanography*, *55*(5–7), 734–751. https://doi.org/10.1016/J.DSR2.2007.12.033

Sauter, D., & Cannat, M. (2013). The Ultraslow Spreading Southwest Indian Ridge. *Diversity of Hydrothermal Systems on Slow Spreading Ocean Ridges*, *May 2014*, 153–173. https://doi.org/10.1029/2008GM000843

Schine, C. M. S., Alderkamp, A. C., van Dijken, G., Gerringa, L. J. A., Sergi, S., Laan, P., van Haren, H., van de Poll, W. H., & Arrigo, K. R. (2021). Massive Southern Ocean phytoplankton bloom fed by iron of possible hydrothermal origin. *Nature Communications*, *12*(1), 1–12. https://doi.org/10.1038/s41467-021-21339-5

Schlitzer, R., Anderson, R. F., Dodas, E. M., Lohan, M., Geibert, W., Tagliabue, A., Bowie, A., Jeandel, C., Maldonado, M. T., Landing, W. M., Cockwell, D., Abadie, C., Abouchami, W., Achterberg, E. P., Agather, A., Aguliar-Islas, A., van Aken, H. M., Andersen, M., Archer, C., … Zurbrick, C. (2018). The GEOTRACES Intermediate Data Product 2017. *Chemical Geology*, *493*, 210–223. https://doi.org/10.1016/j.chemgeo.2018.05.040

Sedwick, P. N., Blain, S., Quéguiner, B., Griffiths, F. B., Fiala, M., Bucciarelli, E., & Denis, M. (2002). Resource limitation of phytoplankton growth in the Crozet Basin, Subantarctic Southern Ocean. *Deep Sea Research Part II: Topical Studies in Oceanography*, *49*(16), 3327–3349. https://doi.org/10.1016/S0967-0645(02)00086-3

Sunda, W. G. (1997). Control of dissolved iron concentrations in the world ocean: A comment. In *Marine Chemistry* (Vol. 57, Issues 3–4, pp. 169–172). Elsevier. https://doi.org/10.1016/S0304-4203(97)00045-5

Swart, S., Speich, S., Ansorge, I. J., & Lutjeharms, J. R. E. (2010). An altimetry-based gravest empirical mode south of Africa: 1. Development and validation. *Journal of Geophysical Research: Oceans*, *115*(3), 1–19. https://doi.org/10.1029/2009JC005299

Tagliabue, A., Bopp, L., Dutay, J. C., Bowie, A. R., Chever, F., Jean-Baptiste, P., Bucciarelli, E., Lannuzel, D., Remenyi, T., Sarthou, G., Aumont, O., Gehlen, M., & Jeandel, C. (2010). Hydrothermal contribution to the oceanic dissolved iron inventory. *Nature Geoscience*, *3*(4), 252–256. https://doi.org/10.1038/ngeo818

Tagliabue, A., Bowie, A. R., DeVries, T., Ellwood, M. J., Landing, W. M., Milne, A., Ohnemus, D. C., Twining, B. S., & Boyd, P. W. (2019). The interplay between regeneration and scavenging fluxes drives ocean iron cycling. *Nature Communications*, *10*(1), 1–8. https://doi.org/10.1038/s41467-019-12775-5

Tagliabue, A., Mtshali, T., Aumont, O., Bowie, A. R., Klunder, M. B., Roychoudhury, A. N., & Swart, S. (2012). A global compilation of dissolved iron measurements: Focus

on distributions and processes in the Southern Ocean. *Biogeosciences*, *9*(6), 2333–2349. https://doi.org/10.5194/bg-9-2333-2012

Tagliabue, A., Sallée, J. B., Bowie, A. R., Lévy, M., Swart, S., & Boyd, P. W. (2014). Surface-water iron supplies in the Southern Ocean sustained by deep winter mixing. *Nature Geoscience*, *7*(4), 314–320. https://doi.org/10.1038/ngeo2101

Tagliabue, A., Bowie, A. R., Boyd, P. W., Buck, K. N., Johnson, K. S., & Saito, M. A. (2017). The integral role of iron in ocean biogeochemistry. In *Nature* (Vol. 543, Issue 7643, pp. 51–59). Nature Publishing Group. https://doi.org/10.1038/nature21058

Tagliabue, A., & Resing, J. (2016). Impact of hydrothermalism on the ocean iron cycle. *Philosophical Transactions of the Royal Society A: Mathematical, Physical and Engineering Sciences*, *374*(2081). https://doi.org/10.1098/rsta.2015.0291

Thuróczy, C. E., Gerringa, L. J. A., Klunder, M. B., Laan, P., & de Baar, H. J. W. (2011). Observation of consistent trends in the organic complexation of dissolved iron in the Atlantic sector of the Southern Ocean. *Deep Sea Research Part II: Topical Studies in Oceanography*, *58*(25–26), 2695–2706. https://doi.org/10.1016/J.DSR2.2011.01.002

Tsujino, H., Urakawa, S., Nakano, H., Small, R. J., Kim, W. M., Yeager, S. G., Danabasoglu, G., Suzuki, T., Bamber, J. L., Bentsen, M., Böning, C. W., Bozec, A., Chassignet, E. P., Curchitser, E., Boeira Dias, F., Durack, P. J., Griffies, S. M., Harada, Y., Ilicak, M., … Yamazaki, D. (2018). JRA-55 based surface dataset for driving ocean–sea-ice models (JRA55-do). *Ocean Modelling*, *130*, 79–139. https://doi.org/10.1016/j.ocemod.2018.07.002

Twining, B. S., Nodder, S. D., King, A. L., Hutchins, D. A., LeCleir, G. R., DeBruyn, J. M., Maas, E. W., Vogt, S., Wilhelm, S. W., & Boyd, P. W. (2014). Differential remineralization of major and trace elements in sinking diatoms. *Limnology and Oceanography*, *59*(3), 689–704. https://doi.org/https://doi.org/10.4319/lo.2014.59.3.0689

Weir, I., Fawcett, S., Smith, S., Walker, D., Bornman, T., & Fietz, S. (2020). Winter biogenic silica and diatom distributions in the Indian sector of the Southern Ocean. *Deep-Sea Research Part I: Oceanographic Research Papers*, *166*, 103421. https://doi.org/10.1016/j.dsr.2020.103421

Weiss, R. F. (1970). The solubility of nitrogen, oxygen and argon in water and seawater. *Deep-Sea Research and Oceanographic Abstracts*, *17*(4), 721–735. https://doi.org/10.1016/0011-7471(70)90037-9

Welschmeyer, N. A. (1994). Fluorometric analysis of chlorophyll a in the presence of chlorophyll b and pheopigments. *Limnology and Oceanography*, *39*(8), 1985–1992. https://doi.org/10.4319/LO.1994.39.8.1985

Wolters, M., 2002. Determination of Silicate in Brackish or Seawater by Flow Injection Analysis. QuikChem® Method 31-114-27-1-D. Lachat Instruments, USA.

Yücel, M., Gartman, A., Chan, C. S., & Luther, G. W. (2011). Hydrothermal vents as a kinetically stable source of iron-sulphide-bearing nanoparticles to the ocean. *Nature Geoscience*, *4*(6), 367–371. https://doi.org/10.1038/ngeo1148

Chapter 3: Early winter barium excess in the Southern Indian Ocean as an annual remineralisation proxy (GEOTRACES GIPr07 cruise)

Natasha René van Horsten[1,2,3], Hélène Planquette[1], Géraldine Sarthou[1], Thomas James Ryan-Keogh[2], Nolwenn Lemaitre[5], Thato Nicholas Mtshali[4], Alakendra Roychoudhury[3], and Eva Bucciarelli[1]

[1]Univ Brest, CNRS, IRD, Ifremer, LEMAR, F-29280 Plouzane, France.

[2]SOCCO, CSIR, Lower Hope road, Cape Town, South Africa, 7700.

[3]TracEx, Department of Earth Sciences, Stellenbosch University, Stellenbosch, South Africa, 7600.

[4]Department of Environment, Forestry and Fisheries, Oceans and Coast, Foretrust Building, Martin Hammerschlag Way, Cape Town, South Africa, 8001

[5]Department of Earth Sciences, Institute of Geochemistry and Petrology, ETH Zurich, Zurich, Switzerland.

Correspondence to: Natasha van Horsten (nvhorsten@csir.co.za), Eva Bucciarelli (Eva.Bucciarelli@univ-brest.fr)

Abstract. The Southern Ocean (SO) is of global importance to the carbon cycle, and processes such as mesopelagic remineralisation that impact the efficiency of the biological carbon pump in this region need to be better constrained. During this study early austral winter barium excess (Ba_{xs}) concentrations were measured for the first time, along 30°E in the Southern Indian Ocean. Winter Ba_{xs} concentrations of 59 to 684 pmol L^{-1} were comparable to those observed throughout other seasons. The expected decline of the mesopelagic Ba_{xs} signal to background values during winter was not observed, supporting the hypothesis that this remineralisation proxy likely has a longer timescale than previously reported. A compilation of available SO mesopelagic Ba_{xs} data, including data from this study, shows an accumulation rate of ~ 0.9 µmol m^{-2} d^{-1} from September to July that correlates with temporally integrated remotely sensed

primary productivity (PP), throughout the SO from data spanning ~ 20 years, advocating for a possible annual timescale of this proxy. The percentage of mesopelagic POC remineralisation as calculated from estimated POC remineralisation fluxes over integrated remotely sensed PP was ~ 2 fold higher south of the polar front (19 ± 15 %, n = 39) than north of the polar front (10 ± 10 %, n = 29), revealing the higher surface carbon export efficiency further south. By linking integrated remotely sensed PP to mesopelagic Ba_{xs} stock we could obtain better estimates of carbon export and remineralisation signals within the SO on annual and basin scales.

3.1 Introduction

The Southern Ocean (SO) is a carbon sink of global significance responsible for 40 – 50 % of the global oceans' carbon uptake (Friedlingstein et al., 2019; Gregor et al., 2019; Gruber et al., 2019). Oceanic carbon uptake is regulated by various processes, including the biological carbon pump (BCP). Inorganic carbon is consumed and released by photosynthetic organisms through photosynthesis and respiration (Sarmiento and Gruber, 2006), thereby regulating the earth's carbon cycle by partially sequestering photosynthetically fixed CO_2 in the ocean interior (Honjo et al., 2014). In particular, the SO BCP is a crucial contributor to the earth's carbon cycle by exporting, from surface waters, ~ 3 Pg C yr^{-1} of the ~ 10 Pg C yr^{-1} global export production (Schlitzer, 2002). The efficiency of the BCP is linked to the export and preservation of surface particulate matter and is directly linked to atmospheric CO_2 levels, on glacial-interglacial timescales (Honjo et al., 2014; Sigman et al., 2010).

Sedimentation out of the surface layer (~100 m) is defined as surface export and out of the mesopelagic zone (~1000 m) as deep export (Passow and Carlow, 2012). There are large gaps in our knowledge with regard to deep carbon export, internal cycling and the seasonality of these processes (Takahashi et al., 2012). The magnitude of deep carbon export is dependent on the efficiency of mesopelagic remineralisation (Jacquet et al., 2015) which can balance or even

exceed particulate organic carbon (POC) surface export, especially later in the growing season, thereby limiting deep export (Buesseler and Boyd, 2009; Cardinal et al., 2005; Jacquet et al., 2011, 2015; Lemaitre et al., 2018; Planchon et al., 2013). A possible explanation for imbalances between surface export and mesopelagic processes can be lateral advection of surface waters with lower particle export relative to the mesopelagic signal (Planchon et al., 2013). It is also possible that continued remineralisation of earlier larger export fluxes is detected in the mesopelagic signal but not in the export fluxes of in situ observations (Planchon et al., 2013). In addition to this, the efficiency of remineralisation is influenced by the size and composition of exported particles (Rosengard et al., 2015; Twining et al., 2014) as well as the pathway by which these particles are transported downwards (e.g., eddy-subduction, active migration, sinking or mixing) from the surface mixed layer to the mesopelagic zone (Boyd et al., 2019; Le Moigne, 2019), creating an intricate web of processes to disentangle. Mesopelagic remineralisation has also been shown to be influenced by environmental factors, such as temperature, phytoplankton community structure and nutrient availability (Bopp et al., 2013; Buesseler and Boyd, 2009). Indeed, nutrient limitation in surface waters limits export and consequently mesopelagic remineralisation by promoting the shift to smaller phytoplankton assemblages that preferentially take up recycled nutrients in the surface mixed layer (Planchon et al., 2013). Phytoplankton community composition exerts an important control where diatoms are more efficiently exported, due to their large size and ballasting by biogenic silica, compared to smaller non-diatom phytoplankton (Armstrong et al., 2009; Buesseler, 1998; Ducklow et al., 2001). Latitudinal trends in remineralisation efficiency can also be linked to temperature-dependent heterotrophs that are responsible for remineralisation (DeVries and Weber, 2017; Marsay et al., 2015). The mesopelagic layer is under-studied, especially in the high latitudes, and therefore these processes are poorly constrained, despite their importance to global elemental cycles, including that of carbon (Le Moigne, 2019; Robinson et al., 2010).

Export and remineralisation tracers, such as $^{234}Th/^{238}U$ and apparent oxygen utilization (AOU), have been used to study mesopelagic POC remineralisation fluxes (Buesseler et al., 2005; Planchon et al., 2013; Lemaitre et al., 2018). Surface export is set by the deficit of ^{234}Th activities over ^{238}U activities, while remineralisation processes are reflected by $^{234}Th/^{238}U$ ratios larger than 1 below the surface mixed layer integrating processes over a 2 to 3 week period (Buesseler et al., 2005; Planchon et al., 2013). AOU is the depletion of oxygen (O_2) in the ocean interior relative to surface saturation, due to biological respiration, when surface water masses are subducted. AOU is dependent on salinity and temperature and integrates remineralisation on timescales of years to decades (Ito et al., 2004). Inaccuracies have, however, been detected with AOU as a remineralisation proxy, specifically in high latitude areas, due to O_2 undersaturation as a consequence of large temperature gradients (Ito et al., 2004).

Barium excess (Ba_{xs}) is another proxy utilized to yield estimates of mesopelagic POC remineralisation fluxes. It is defined as the "biogenic" portion of particulate Barium (pBa) as barite crystals, formed by the decay of bio-aggregates below the surface mixed layer (Bishop, 1988; Dehairs et al., 1980; Lam and Bishop, 2007; Legeleux and Reyss, 1996; van Beek et al., 2007). As these crystals are released, a Ba_{xs} peak is formed within the mesopelagic zone which has been found to correlate to primary production (PP), O_2 consumption and POC remineralisation (Dehairs et al., 1997). Depth-integrated rates of O_2 consumption between the base of the mixed layer and 1000 m were estimated using an inverse 1-D advection-diffusion-consumption model (Shopova et al., 1995) to develop a transfer function between the Ba_{xs} signal and the rate of surface POC export for subsequent mesopelagic remineralisation (Dehairs et al., 1997). Strong correlations have been obtained between the well-established export/remineralisation flux proxy ^{234}Th and Ba_{xs}, during studies conducted in the SO and the North Atlantic, confirming the validity of Ba_{xs} as a remineralisation proxy (Cardinal et al.,

2005; Lemaitre et al., 2018; Planchon et al., 2013). Estimates of POC remineralisation fluxes, using the Ba_{xs} proxy, are directly influenced by the background signal of $Ba_{xs,}$ after partial dissolution and sedimentation from the previous bloom season. It can be thought of as "pre-formed Ba_{xs}", defined as the $Ba_{residual}$ signal at zero O_2 consumption (Jacquet et al., 2015). Because studies conducted in spring and summer suggest that the mesopelagic Ba_{xs} signal lasts between a few days to a few weeks (Dehairs et al., 1997; Cardinal et al., 2005; Jacquet et al., 2007, 2008a), it is postulated that winter measurements should give the true SO $Ba_{residual}$ value (Jacquet et al., 2008b, 2011). In this context, as part of a GEOTRACES process study (GIpr07) of a transect along 30°E in the Southern Indian Ocean (58.5°S to 41.0°S), we studied Ba_{xs} distributions during early austral winter (July 2017) to better constrain the SO $Ba_{residual}$ concentrations and the timescale of this proxy. To our knowledge these are the first reported wintertime values for this proxy in the SO.

3.2 Materials and Methods

3.2.1 Sampling and hydrography

During the GEOTRACES GIpr07 cruise, which took place in early austral winter (28 June - 13 July 2017) onboard the R/V *SA Agulhas II*, seven stations were sampled along 30°E, from 58.5°S to 41.0°S (WOCE I06S, Figure 3.1a). At each station between 15 and 21 samples were collected from 25 m down to 1500 m, for shallow stations, and down to 4250 m, for deep stations, to be analysed for multiple parameters.

Positions of the fronts during the cruise were determined using the July monthly mean absolute dynamic topography data from the CLS/AVISO product (Rio et al., 2011), with boundary definitions from Swart et al. (2010). From north to south the identified fronts are, the Subtropical Front (STF), the Subantarctic Front (SAF), the Polar Front (PF), the Southern Antarctic Circumpolar Current Front (SACCf) and the Southern Boundary (SBdy) (Figure 3.1a). The marginal ice zone, identified as the position of 30 % ice cover, was positioned at

61.7°S, approximately 3° (356 km) south of the southernmost station (de Jong et al., 2018). Therefore, a potential sea ice influence on our study area can be disregarded.

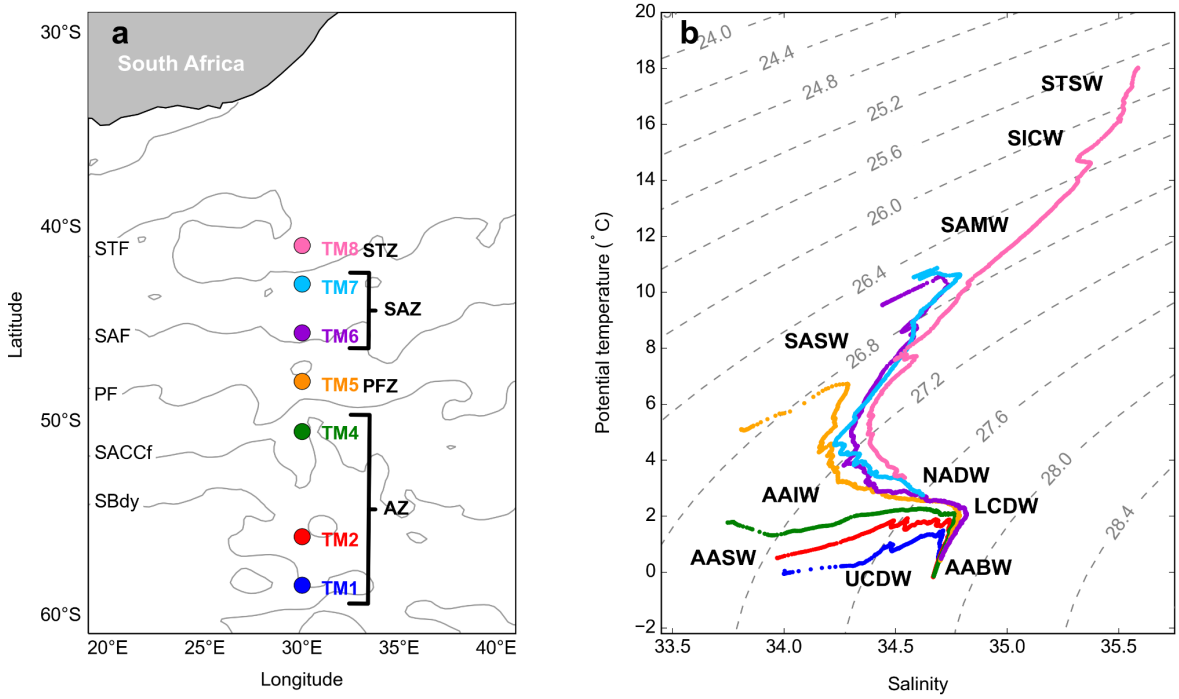

Figure 3.1: (a) GEOTRACES GIPr07 cruise sampling stations overlaid on a map with frontal positions; namely, the Subtropical Front (STF), the Subantarctic Front (SAF), the Polar Front (PF), the Southern Antarctic Circumpolar Current Front (SACCf) and the Southern Boundary (SBdy), as determined by mean absolute dynamic topography (MADT) and crossing over four zones; namely, the Antarctic zone (AZ), the Polar frontal zone (PFZ), the Subantarctic zone (SAZ) and the Subtropical zone (STZ). (b) Potential temperature plotted against salinity, overlaid on isopycnals and identification of water masses sampled; namely, Subtropical Surface Water (STSW), South Indian Central Water (SICW), Subantarctic Mode Water (SAMW), Subantarctic Surface Water (SASW), Antarctic Intermediate Water (AAIW), Antarctic Surface Water (AASW), North Atlantic Deep Water (NADW), Lower Circumpolar Deep Water (LCDW), Upper Circumpolar Deep Water (UCDW), and Antarctic Bottom Water (AABW).

3.2.2 Temperature, salinity and dissolved O_2

Temperature (°C), salinity and dissolved O_2 (µmol L^{-1}) profiles were measured by sensors (SBE 911plus) which were calibrated by the manufacturer within a year prior to the cruise. At each cast, discrete seawater samples were collected and analysed onboard for in situ calibration of sensor data for salinity (8410A Portasal salinometer, R^2 = 0.99) and dissolved O_2 concentrations (Metrohm 848 titrino plus, R^2 = 0.83; Ehrhardt et al., 1983). Temperature and salinity measurements were used to calculate potential density (σ_θ; Gill, 1982) to characterise water masses sampled and to identify the mixed layer depth (MLD). The MLD is the depth at which there is a change of 0.03 kg m^{-3} in σ_θ from a near-surface value at ~ 10 m (de Boyer

Montégut, et al., 2004). Decreases in dissolved O_2 concentrations at intermediate depths, together with Ba_{xs} concentrations, were used to define the mesopelagic remineralisation layer.

3.2.3 pBa and pAl

Profile sampling of the water column was conducted with a GEOTRACES compliant trace metal clean CTD housed on an epoxy coated aluminium frame with titanium bolts equipped with 24 x 12 L trace metal clean Teflon coated GO-FLO bottles (General Oceanics). All sampling and analyses were conducted following the GEOTRACES clean sampling and analysis protocols (Cutter et al., 2017). Volumes of 2 to 7 L seawater were filtered from the GO-FLO bottles onto acid-washed polyethersulfone filters (25 mm diameter, Supor, 0.45 µm pore size), for pBa and pAl analyses. Filters were mounted in-line on the side spigot of each Go-Flo bottle, on swinnex filter holders. Furthermore, bottles were mixed 3 times before filtration, as recommended by the GEOTRACES protocols (Cutter et al., 2017), to ensure homogenous sampling. Although the large fast-sinking fraction of particles may be undersampled by using bottles (Bishop and Edmond, 1976; Planquette and Sherrell, 2012), comparing data that were generated using the same, internationally validated sampling systems and protocols (Cutter et al. 2017), as we do in this study, minimises potential bias. After filtration, filters were placed in trace metal clean petri slides (Pall) and kept frozen at -20°C until further processing on land. Sample processing was conducted under a class 100 HEPA filtered laminar flow and extraction hood in a clean laboratory.

The pBa and pAl samples were processed and analysed 6 months after sample collection, at LEMAR (France). Unused blank filters and filters containing the samples were acid reflux digested at 130°C in acid-cleaned savillex vials using a mixture of HF and HNO_3 (both Ultrapure grade, Merck) solutions (Planquette and Sherrell, 2012). Archive solutions were stored in 3 ml of 0.12 M HNO_3 (Ultrapur grade), of which 250 µL was diluted up to 2 mL for analysis by sector field inductively coupled plasma mass spectrometry (SF-ICP-MS, Element

XR Thermo Scientific). Samples were spiked with 1 µg L^{-1} indium as an internal standard to correct for instrument drift. The detection limits, defined as three times the standard deviation of the blanks (unused filter blanks), were 0.39 pmol L^{-1} and 0.03 nmol L^{-1} (n = 5) for pBa and pAl, respectively. Mean amounts (in nmol) of a given element determined in unused filter blanks were subtracted from the amounts in the sample filter then divided by the volume filtered. Three certified reference materials (BCR 414, MESS 4 and PACS 3) were processed and analysed with the samples to assess the accuracy of the methodology. Our values were in good agreement with the certified values of the reference materials (Table 3.1) (Jochum et al., 2005). Percentage error of analyses was determined by the repeat analysis of random samples during each run, the mean percentage error of sample analysis for pBa and pAl was 9.2 ± 2.5 % and 11.1 ± 4.6 % (mean ± SD, n = 6), respectively.

Table 3.1: Certified Reference Material recovery data for accuracy determination of pBa and pAl analyses
N/A: refers to instances where there is no certified values available to check for accuracy

	pBa (mg/kg)	pAl (mg/kg)
PACS 3 certified (mean ± SD)	N/A	65800 ± 1700
PACS 3 measured (mean ± SD)	N/A	73156 ± 15416
PACS 3 mean % recovery	N/A	111 ± 23
MESS 4 certified	920	79000 ± 2000
MESS 4 (mean ± SD)	1033 ± 28	100048 ± 26870
MESS 4 mean % recovery ± SD	112 ± 3	127 ± 34
BCR 414 indicative values	32 ± 5	2384 ± 652
BCR 414 (mean ± SD)	34 ± 4	2651 ± 317
BCR 414 mean % recovery ± SD	105 ± 12	111 ± 13

3.2.4 Ba_{xs} as a proxy for mesopelagic POC remineralisation

The non-lithogenic fraction of pBa, Ba_{xs}, was calculated by subtracting the lithogenic fraction of pBa from the total pBa measured using Eq. 1. The lithogenic contribution to pBa was

calculated by multiplying the pAl concentration with the Ba/Al upper continental crust (UCC) ratio, 0.00135, as determined by Taylor and McLennan (1985).

$$Ba_{xs} = [pBa] - ([pAl] \times (Ba/Al)_{UCC}) \quad (1)$$

Total pBa and Ba_{xs} profiles were nearly identical with a mean percentage Ba_{xs} to total pBa of 99 ± 1 % (mean ± SD, n = 124; Table B2), indicating that pBa from lithogenic sources was negligible. This ensures the accurate estimation of Ba_{xs}, which requires that less than 50 % of pBa should be associated with lithogenic inputs (Dymond et al., 1992).

The mesopelagic POC remineralisation flux was estimated using Eq. 2 (Dehairs et al., 1997; Shopova et al., 1995).

$$Mesopelagic\ POC\ remineralisation = Z \times JO_2 \times (C{:}O_2)_{Redfield\ Ratio} \times 12.01 \quad (2)$$

Where the mesopelagic POC remineralisation flux is expressed in mg C m^{-2} d^{-1}, Z is the depth range of the mesopelagic Ba_{xs} layer (100 - 1000 m), C:O_2 is the stoichiometric molar ratio of carbon to O_2 consumption by remineralisation as per the Redfield Ratio (127/175, Broecker et al., 1985), 12.01 is the molar mass of carbon (g mol^{-1}) and JO_2 is the rate of O_2 consumption (µmol L^{-1} d^{-1}) as estimated using Eq. 3 (Dehairs et al., 1997; Shopova et al., 1995).

$$JO_2 = (Mesopelagic\ Ba_{xs} - Ba_{residual})/17200 \quad (3)$$

Where mesopelagic Ba_{xs} is the depth-weighted average Ba_{xs} of the mesopelagic zone (pmol L^{-1}), the constant value of 17200 is the slope of the linear regression of depth-weighted average Ba_{xs} (pmol L^{-1}) versus O_2 consumption rate (µmol L^{-1} d^{-1}) using the Southern Ocean transfer

function by Dehairs et al. (1997) and $Ba_{residual}$ is the deep ocean background value of Ba_{xs} at zero oxygen consumption. The literature value of 180 pmol L^{-1} was used as the $Ba_{residual}$ value (Dehairs et al., 1997) in our calculations.

The integrated mesopelagic Ba_{xs} stock (µmol m^{-2}) over the mesopelagic layer (100 - 1000 m) was calculated from the depth-weighted average Ba_{xs} in order to investigate the link between the accumulated mesopelagic signal and the corresponding integrated remotely sensed primary productivity (PP).

3.2.5 Integrated remotely sensed PP

The integrated remotely sensed PP (mg C m^{-2} d^{-1}) within the surface mixed layer was calculated using the CbPM algorithm (Behrenfeld et al., 2005), which requires chlorophyll concentration (mg m^{-3}), particulate backscatter (λ 443 nm, m^{-1}), photosynthetically active radiation (PAR; µmol photons m^{-2} d^{-1}) and the MLD (m). Ocean Colour-Climate Change Initiative (OC-CCI) data (https://esa-oceancolour-cci.org/), which blends existing data streams into a coherent record, meeting the quality requirements for climate assessment (Sathyendranath et al., 2019), were used for chlorophyll and particulate backscatter. PAR was taken from GLOB colour (http://www.globcolour.info/), and the MLD was taken from the climatology of de Boyer Montegut et al. (2004). The integrated remotely sensed PP data were regridded to 0.25° spatially, using bilinear interpolation using the Python programming package xESMF (Zhuang, 2018), and averaged monthly. The area-averaged PP was averaged over a 6 x 1° rectangular sample area, positioned 6° upstream longitudinally, and 1° latitudinally centred around each sampled station (see discussion for details). In order to assess the validity of the remotely sensed PP data and demonstrate no meridional bias across the SO, the percentage valid pixels was calculated for data north (90 ± 20 %; mean ± SD, n = 370) and south (82 ± 29 % mean ± SD, n = 488) of the PF, revealing no bias.

3.2.6 Integrated % POC remineralised

The integrated remineralised POC (mg C m^{-2}) was estimated by multiplying the POC remineralisation flux (mg C m^{-2} d^{-1}), as estimated using the Ba_{xs} proxy method, by the number of days over which the corresponding remotely sensed PP (mg C m^{-2} d^{-1}) was subsampled. The % POC remineralised was then estimated as the percentage of integrated remotely sensed PP (mg C m^{-2}) remineralised, assuming that the mesopelagic Ba_{xs} stock signal observed is due to the remineralisation of the integrated surface PP signal.

3.2.7 Statistical analysis

For statistical analysis, the least squares regression method was applied for assessment of significant correlations (Barbur et al., 1994). Significant differences between regions and regressions were tested using Welch's t-test, with an alpha of 0.05 (95 % confidence level) (Kokoska and Zwillinger, 2000).

3.3 Results

3.3.1 Hydrography

The potential temperature (θ) and salinity (S) along the transect ranged from -0.06 to 18.03 °C and from 33.77 to 35.59, respectively. Where surface θ and S define four hydrographic zones; namely, the Antarctic zone (AZ; $\theta < 2.5$ °C; $S \leq 34$) from ~ 50°S to 58.5°S, the polar frontal zone (PFZ; $\theta \cong 5$ °C; $S \cong 33.8$) at ~ 48°S, the subantarctic zone (SAZ; $5 < \theta < 11$ °C; $33.8 < S < 34.7$) between 43°S and 45.5°S, and the subtropical zone (STZ; $\theta \geq 17.9$ °C; $S \cong 35.6$) at 41°S (Figure 3.1a; Anilkumar and Sabu, 2017; Orsi et al., 1995; Pollard et al., 2002). The MLDs along the transect ranged between 97 and 215 m (144 ± 39 m; mean ± SD, n = 7), shoaling towards the PF (Table B1).

As can be observed on the T-S plot of stations sampled (Figure 3.1b), different water masses were sampled along the transect throughout the water column. South of the polar front (SPF; ≳ 50°S; TM1, 2 and 4), from surface to depth, Antarctic Surface Water (AASW; $27 < \sigma_\theta <$

27.4 kg.m^{-3}), Upper and Lower Circumpolar Deep Water (UCDW; 27.2 < σ_θ < 27.75 kg.m^{-3} and LCDW; 27.75 < σ_θ < 27.85 kg.m^{-3}, respectively), and Antarctic Bottom Water (AABW; 27.8 < σ_θ < 27.85 kg.m^{-3}) were characterised. North of the polar front (NPF) and south of the STF (< 50°S; TM5, 6 and 7), from surface to depth, Subantarctic Surface Water (SASW; 26.5 < σ_θ < 26.75 kg.m^{-3}), Antarctic Intermediate Water (AAIW; 26.7 < σ_θ < 27.4 kg.m^{-3}), North Atlantic Deep Water (NADW; 27 < σ_θ < 27.85 kg.m^{-3}) and, as far north as 45.5°S, AABW close to the ocean floor, were identified. At the northernmost station (TM8; 41°S), in the STZ, the water masses sampled include Subtropical Surface Water (STSW; $\sigma_\theta \cong$ 25.7 kg.m^{-3}), South Indian Central Water (SICW; 25.8 < σ_θ < 26.2 kg.m^{-3}), Subantarctic Mode Water (SAMW; 26.2 < σ_θ < 26.6 kg.m^{-3}), AAIW and NADW.

3.3.2 Dissolved O_2

The water column dissolved O_2 concentrations ranged from 159 to 333 µmol L^{-1} (Figure 3.2). Maximum concentrations were observed in the surface mixed layer, increasing southwards along the transect, with a mean value of 287 ± 40 µmol L^{-1} (mean ± SD, n = 700). A decrease in concentrations below the MLD coincided with an increase in σ_θ. South of the PF, the decrease in dissolved O_2 concentrations at the MLD was sharp and relatively shallow when compared to profiles NPF, which were more gradual, spanning a wider depth range. Within the mesopelagic zone concentrations decreased down to 204 ± 29 µmol L^{-1} (mean ± SD, n = 6373), then remained relatively uniform below 1000 m at 192 ± 113 µmol L^{-1} (mean ± SD, n = 12950).

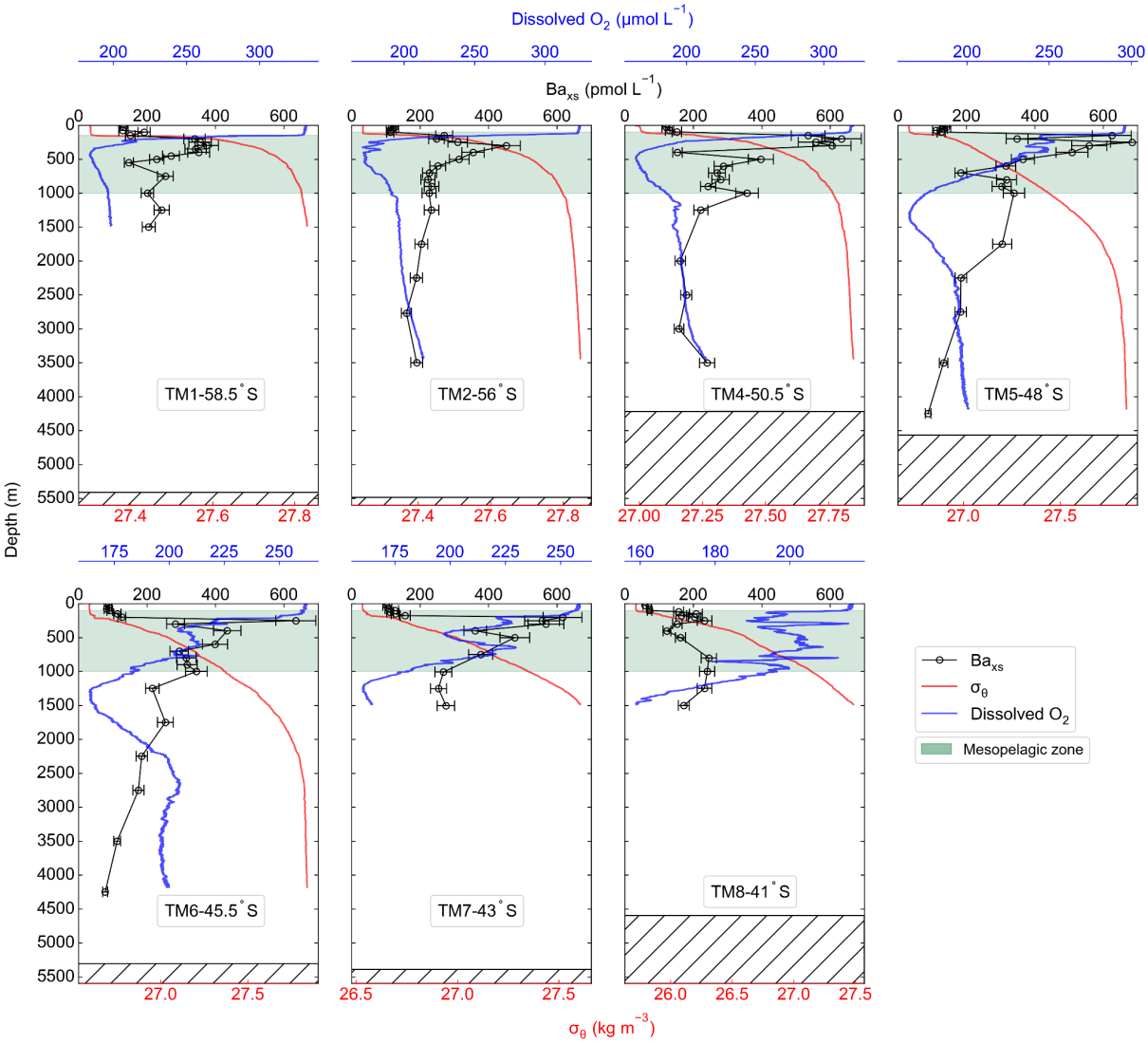

Figure 3.2: Ba_{xs} (black circles) with error bars, potential density (σ_θ; red) and dissolved O_2 (blue) profiles sampled along the transect, plotted against depth, for stations TM1 to TM8, from south to north. The green shaded area is the mesopelagic zone, and the hatched area is the ocean floor.

3.3.3 Ba_{xs} and estimated POC remineralisation fluxes

Along the transect, Ba_{xs} concentrations ranged from 59 to 684 pmol L^{-1}. All profiles exhibited a depletion of Ba_{xs} in the upper surface waters (59 - 152 pmol L^{-1}), then a rapid increase below the MLD (~150 m), with concentrations ranging between 113 and 684 pmol L^{-1} in the mesopelagic zone (100 - 1000 m, Figure 3.2). At the two southernmost stations (TM1 and TM2), mesopelagic Ba_{xs} peaks spanned a narrower depth range (100 - 600 m) than stations further north, with concentrations reaching values of ~ 400 pmol L^{-1}. Concentrations were higher in the PFZ and SAZ with a maximum of 684 pmol L^{-1} in the PFZ, at 48°S (TM5). The subsurface increase of Ba_{xs} started at slightly deeper depths (150 - 200 m) and spanned wider

depth ranges down to 1000 m, at stations north of the PF. The STZ station, at 41°S (TM8), had the lowest concentrations, only increasing up to ~ 200 pmol L^{-1}. Double peaks were observed at all stations north of the PF, with a shallow and more substantial peak occurring in the upper mesopelagic zone and a second peak in the lower mesopelagic zone. Below the mesopelagic zone, Ba_{xs} concentrations decreased down to ~ 180 pmol L^{-1} and remained relatively uniform. The mean $Ba_{residual}$ concentration south of PF was 183 ± 29 pmol L^{-1} (mean ± SD, n = 7), whereas it was 142 ± 45 pmol L^{-1} (mean ± SD, n = 8) between the PF and the STF. The two regions were however not significantly different to each other when conducting a Welch's t-test (t-statistic = 2.10; p-value = 0.06) and when averaging all concentrations below 2000 m along the transect, the $Ba_{residual}$ concentration was 161 ± 43 pmol L^{-1} (mean ± SD, n = 15). This concentration is not statistically different from the literature value of 180 pmol L^{-1} (Dehairs et al., 1997), which is widely used for estimates of POC remineralisation fluxes. For a better comparison with these previous estimates, we used 180 pmol L^{-1} for the $Ba_{residual}$ concentration in our calculations.

The estimated POC remineralisation fluxes for the study area ranged from 6 to 96 mg C m^{-2} d^{-1} (Table B3), increasing northwards from the southernmost station up to the PFZ from 32 to 92 mg C m^{-2} d^{-1}, then decreasing down to 70 mg C m^{-2} d^{-1} at the SAF. The highest flux was estimated in the SAZ and the lowest flux was estimated in the STZ.

3.4 Discussion

3.4.1 Early wintertime Ba_{xs} and $Ba_{residual}$ concentrations

A noticeable difference between profiles sampled early in the bloom season (Dehairs et al., 1997; Jacquet et al., 2015) versus those sampled later (Cardinal et al., 2001; Planchon et al., 2013) is the contrasted Ba_{xs} concentrations in the surface mixed layer. Dehairs et al. (1997) has shown that these concentrations of Ba_{xs} can be as high as 9000 pmol L^{-1} in areas of high productivity during spring, which then become depleted to concentrations below the SO

$Ba_{residual}$ value of ~ 180 pmol L^{-1}, as productivity declines and surface POC export increases (Planchon et al., 2013). These high surface concentrations are, however, not due to the same process as the one that controls the Ba_{xs} concentrations within the mesopelagic zone (Jacquet et al., 2011). Surface water concentrations are associated with Ba adsorbed onto particles whereas the mesopelagic Ba_{xs} signal is due to barite crystals formed within decaying bio-aggregates (Cardinal et al., 2005; Lam and Bishop, 2007; Lemaitre et al., 2018; Sternberg et al., 2005). In this study, we observed surface depletion of Ba_{xs} at all stations, in line with the assumption that the bulk surface export from the preceding bloom had been achieved at the time of sampling and, the majority of the Ba_{xs} had been transferred to the mesopelagic zone.

A sharp increase in σ_θ observed at the MLD has previously been identified as the depth at which decaying bio-aggregates are formed (Lam and Bishop, 2007). These increases coincided with an increase in Ba_{xs} (Figure 3.2), linking the subsurface Ba_{xs} signal to decaying bio-aggregates as per previous studies (Cardinal et al., 2005; Dehairs et al., 1997; Jacquet et al., 2011). Additionally, decreases observed in dissolved O_2 profiles along the transect were also accompanied by coinciding increases in Ba_{xs}, in line with O_2 consumption due to remineralisation within the mesopelagic zone (Figure 3.2) (Cardinal et al., 2005; Jacquet et al., 2005, 2011). The observed range of mesopelagic Ba_{xs} concentrations (113 - 684 pmol L^{-1}) were comparable to those previously reported in SO open waters (~ 200 - 1000 pmol L^{-1}; Cardinal et al., 2001, 2005; Jacquet et al., 2005, 2008a, 2008b, 2011, 2015; Planchon et al., 2013).

Ba_{xs} profiles exhibited similar distributions to those reported throughout bloom seasons in the SO, with distinct peaks observed within the mesopelagic zone at all stations. Earlier in the bloom season, peaks mostly occur within the upper half of the mesopelagic zone (100 - 500 m: Cardinal et al., 2001, 2005; Jacquet et al., 2005, 2008a, 2011, 2015), but as the season progresses, they deepen down towards the bottom half of the mesopelagic zone (500 - >1000 m: Jacquet et al., 2008b, Planchon et al., 2013). Deepening and widening of the

remineralisation depth range can be expected as the season progresses, due to continued remineralisation taking place as particles sink to the bottom of the mesopelagic zone (Lemaitre et al., 2018; Planchon et al., 2013). This is also what we observed during early winter at stations NPF, with a second peak in deeper waters, as observed by Jacquet et al. (2008b) during the iron (Fe) fertilisation experiment (EIFEX). The deeper peak could also be linked to relatively larger cells that sink faster as they remineralise, possibly a large bloom earlier in the season.

A distinct latitudinal trend in mesopelagic depth-weighted average Ba_{xs} has generally been observed in the SO with the highest values in the PFZ, decreasing north and southwards from the PF. These latitudinal trends tend to be accompanied by a coinciding trend in in situ surface biomass measurements (Cardinal et al., 2005; Dehairs et al., 1997, Jacquet et al., 2011; Planchon et al., 2013). During our early winter study, we observed a similar latitudinal trend in mesopelagic Ba_{xs} stock (μmol m^{-2}), with an increase from the southernmost station up to the PF, then varying around a maximum in the SAZ, down to the lowest value in the STZ, whereas temporally integrated remotely sensed PP increased progressively northwards to a maximum in the STZ (Figure B1). Time of sampling and extended blooms, which are characteristic of the SAZ (Thomalla et al., 2011), could be contributing factors to the higher values observed in PP and mesopelagic Ba_{xs} distributions at stations north of the PF (Figure B1). Contrary to what was expected, the profiles observed during our early winter study still show a significant mesopelagic remineralisation signal, well after the summer bloom termination, which occurred between April and May (Figure 3.3), as defined by the point in time when community losses outweigh the growth rate (Thomalla et al., 2011).

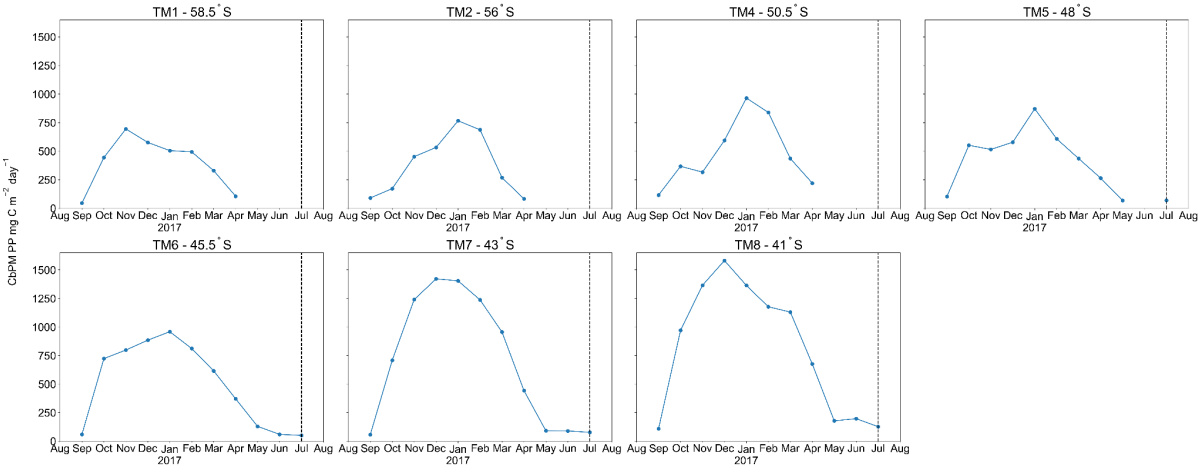

Figure 3.3: Time series, area-averaged (6 x 1° rectangular sample area, positioned 6° upstream longitudinally, and 1° latitudinally centred around each station) remotely sensed CbPM-PP (mg C m^{-2} day^{-1}), monthly average from 08/2016 to 08/2017, dashed vertical lines indicate sampling date.

In deeper waters along the transect, south of the STF, (below 2000 m) where remineralisation is minimal compared to the mesopelagic zone, our Ba_{xs} concentration of 161 ± 43 pmol L^{-1} (mean ± SD, n = 15) is not significantly different from the widely used $Ba_{residual}$ concentration of 180 pmol L^{-1}, measured during early Spring to late Summer (e.g., Dehairs et al. 1997; Jacquet et al., 2015; Planchon et al., 2013). We thus did not observe a wintertime decline to an expected "true" SO background value, when PP and bacterial activity are suspected to be minimal (Jacquet et al., 2011). There are two possible explanations for this; firstly, the decline to a winter background signal might never be achieved due to ongoing barite precipitation and remineralisation, as well as the release of labile Ba attached to phytoplankton as they decay, precipitating into barite crystals, which could possibly continue throughout winter (Cardinal et al., 2005). Secondly, the low sinking speed of suspended barite (~ 0.3 m d^{-1}, Sternberg et al., 2008), once produced in the mesopelagic layer, implies that it would take ~ 6 years (not considering reaggregation and redissolution) to sink from 300 m (~ peak of production) to the bottom of the mesopelagic layer (1000 m depth). The "true" background value may thus have to be measured at the very end of winter just before the initiation of the spring bloom. This also suggests that the Ba_{xs} signal in the mesopelagic layer may represent remineralisation activity over more than a few days to weeks, per previous reports (e.g. Dehairs et al., 1997; Jacquet et al., 2015; Planchon et al., 2013).

3.4.2 Timescale of the mesopelagic Ba_{xs} signal

The Ba_{xs} signal that we observed in winter is in agreement with the suggestion by Dehairs et al. (1997), that there can be significant carry over between bloom seasons. Other studies have also pointed out that the timescale of this proxy is longer than a snapshot view (Cardinal et al., 2005) and have highlighted a seasonal increase in mesopelagic Ba_{xs} (Jacquet et al., 2011). This strongly suggests that the Ba_{xs} signal is not directly linked to synoptic measurements of PP at the time of sampling. In order to investigate this hypothesis, for the first time, we compiled a SO mesopelagic Ba_{xs} stock dataset with all available literature data including data from this study (Figure 3.4a, Table B3). The mesopelagic Ba_{xs} stock was integrated over the Ba_{xs} peak depth range (as identified in each study). As can be seen on the map of the compilation dataset (Figure 3.4a), these data points were collected across the three basins of the SO, over ~ 20 years. Despite this diversity in observations, a statistically significant accumulation of mesopelagic Ba_{xs} with time is still observed, SPF (Figures 3.4b) and NPF (Figures 3.4c). Mesopelagic Ba_{xs} accumulates at a rate of 0.86 (±0.15) µmol m^{-2} d^{-1} SPF ($R^2 = 0.43$, p-value < 0.05, n = 43; Figure 3.4b), and at 0.88 (±0.20) µmol m^{-2} d^{-1} NPF ($R^2 = 0.41$, p-value < 0.05, n = 31; Figure 3.4c), with no statistically significant difference between the two regions (Welch's t-test = 0.24; p-value = 0.80).

A possible link between the integrated mesopelagic Ba_{xs} stock and the corresponding integrated remotely sensed PP was assessed for all studies conducted after September 1997, when remotely sensed PP data became available. To do so, we first estimated that sub millimetre sized aggregates would take ~ 20 days to sink down to 1000 m (considered as the bottom of the mesopelagic zone in this study), using a sinking speed of 50 m d^{-1}, that corresponds to an average literature value (50 - 100 m d^{-1}: Riebesell et al., 1991; 50 - 430 m d^{-1} around South Georgia: Cavan et al. 2015; mean of ~ 100 m d^{-1} in the Southern Ocean as reviewed in Laurenceau-Cornec et al., 2015; Marguerite Bay: 10 - 150 m d^{-1}: McDonnell and Buesseler, 2010). Assuming a maximum surface current speed of 0.2 m s^{-1} (Ferrari and Nikurashin, 2010),

it was estimated that these aggregates would have originated, 346 km west from the station that was sampled for mesopelagic Ba_{xs}, ~ 20 days prior. Using this distance, the dimensions of the sample area were set with the southernmost station (TM1) of this study, where degrees of longitude cover the smallest area. For the sake of consistency this sample area was applied to all sampling locations of the considered dataset. The integrated remotely sensed PP (see section 2.5) was then averaged spatially, positioned 6° upstream longitudinally, and 1° latitudinally centred around each station, in order to capture the surface PP that is assumed to translate to the mesopelagic remineralisation and measured Ba_{xs} stock.

The monthly averaged remotely sensed PP, at the time of sampling, was compiled for the considered dataset, and we found that the PP over the growing season (Figure 3.4d & e) reaches highest values between January and February (day 125 to 175 of the year), thereafter, steadily decreasing to minimal values in July (~ day 310 of the year, i.e., during our study). The mesopelagic Ba_{xs} accumulation over time can, therefore, not be matched with the remotely sensed PP measured during the month of sampling. A possible relationship between mesopelagic Ba_{xs} stock and temporally integrated remotely sensed PP was further investigated by considering longer timescales. Remotely sensed PP of the preceding bloom was temporally integrated from the preceding September, prior to sampling, as the start of the bloom, in general agreement with previous bloom phenology studies (Thomalla et al., 2011), up to one month prior to the sampling date of the study, taking into consideration time needed for export, aggregate formation and barite crystal release through remineralisation (~ 1 month).

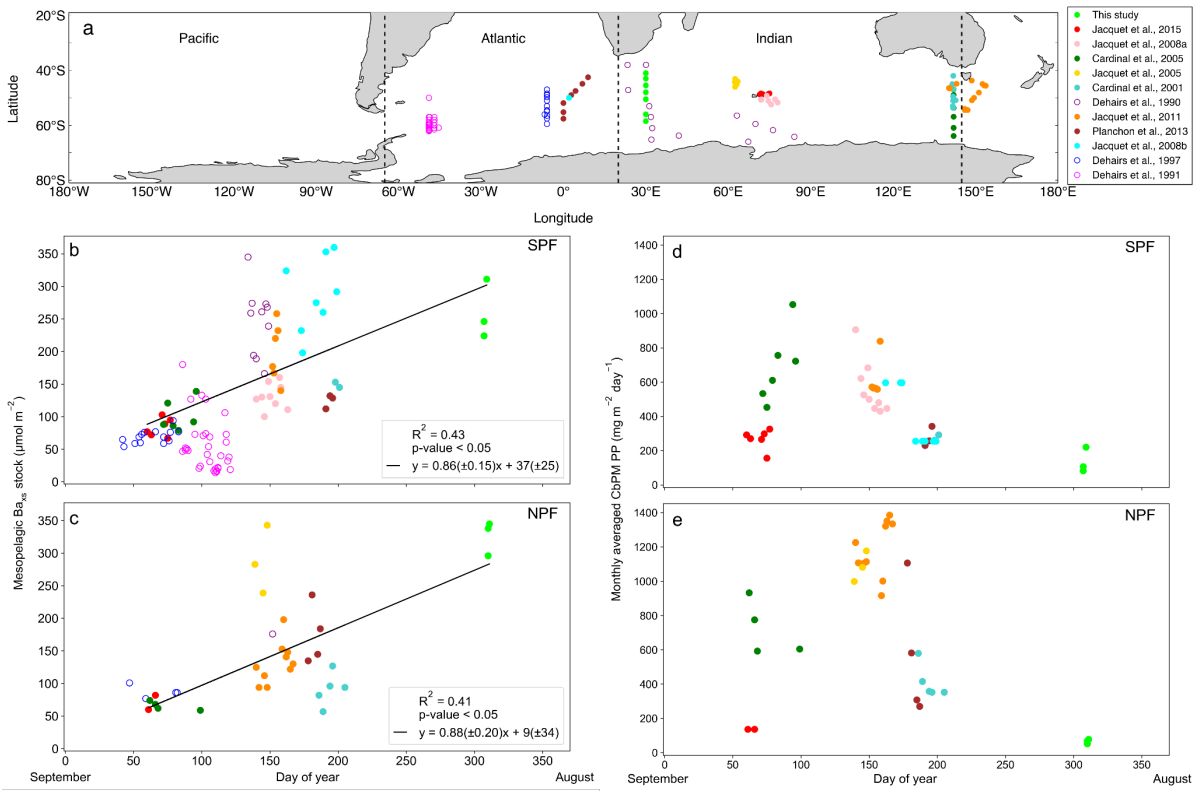

Figure 3.4: (a) Positions of Ba_{xs} observations compiled from all known SO studies, on a cylindrical equal-area projection of the SO, the three SO basin cut offs are indicated by the dashed black lines, from left to right, Pacific, Atlantic and Indian. Integrated mesopelagic Ba_{xs} stock plotted against day of year sampled, with the 1st of September set as day 1, for all available literature data and winter data from this study. Data was split into two zones using the Polar Front (PF) to divide the SO; (b) South of the PF (SPF) and (c) North of the PF (NPF). Monthly averaged remotely sensed PP plotted against day of year, for locations and dates of the SO compilation dataset and winter data from this study; (d) SPF and (e) NPF. Open circles are data points from studies which did not use HF in the particulate sample digestion procedure, regressions did not include these data, there was, however, no significant difference when including these data points (Table B3).

Varying timescales were considered between the preceding September up to 1 month prior to sampling (Sept - T1; Table B4), in monthly increments, that could influence the relationship between remotely sensed PP and the mesopelagic Ba_{xs} stock (Table B4). The strongest and most significant correlation between the mesopelagic Ba_{xs} stock and integrated remotely sensed PP, for both north and south of the PF, was obtained from the preceding September up to 1 month prior to sampling (Table B4, Sept - T1, SPF: Figure 3.5a, $R^2 = 0.55$, p-value < 0.05, n = 39; NPF: Figure 3.5b, $R^2 = 0.42$, p-value < 0.05, n = 31). When remote sensing data was limited due to cloud cover and low sunlight during winter months, specifically at the southernmost stations, all available data was used for the duration of the season. The correlation observed in the STZ is not significant at a 95 % confidence level (p-value = 0.10); however, the limited

number of data points (n = 6) may preclude any significance from emerging. The significant positive correlations obtained south of the STF suggest that mesopelagic Ba_{xs} stock can be used as a remineralisation proxy on an annual timescale instead of only a few weeks. Figure 3.5 also reveals that for a given PP the mesopelagic Ba_{xs} stock was 2-fold higher SPF compared to NPF (Welch's t-test, t-statistic = 2.24; p-value < 0.05), this is further discussed below.

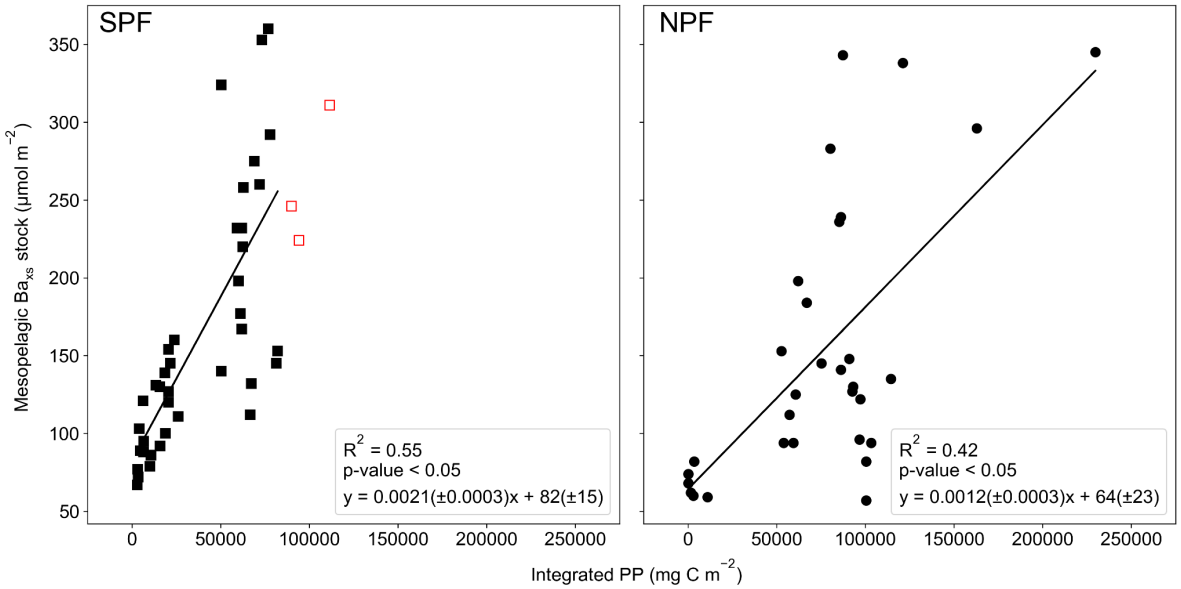

Figure 3.5: Integrated mesopelagic Ba_{xs} stock plotted against integrated remotely sensed PP from the preceding September up to one month prior to sampling, all available literature data and winter data from this study, (a) South of the PF (SPF, black squares) and (b) North of the PF (NPF, black circles). Red open squares are data points from our winter dataset where there was not sufficient remote sensing PP data to integrate up to 1 month prior to sampling and available data up to 3 months prior to sampling was plotted but not included in the statistical analysis.

3.4.3 Environmental factors influencing mesopelagic remineralisation and carbon export efficiency

Estimated POC remineralisation fluxes along the transect (6 - 96 mg C m^{-2} d^{-1}) were on the upper end of the range of fluxes reported in previous studies, with the exception of the STZ station, but within the same order of magnitude for the SO as estimated from spring to autumn (0.2 - 118 mg C m^{-2} d^{-1}; Table B3; Cardinal et al., 2005; Jacquet et al., 2011, 2015; Planchon et al., 2013). As the bloom season progresses, more efficient remineralisation rates have been reported in multiple studies (Cardinal et al., 2005; Jacquet et al., 2011; Planchon et al., 2013). However, during late summer as the bloom declines, observations indicate an inefficient BCP due to enhanced surface nutrient recycling (Dehairs et al., 1992; Jacquet et al., 2011; Planchon

et al., 2013), leading to a decrease in surface POC export (Planchon et al., 2013). Seasonal variation is reported to be more pronounced northwards within the SO with the least variation observed in the southern Antarctic circumpolar current (Dehairs et al., 1997; Planchon et al., 2013).

The percentage of mesopelagic POC remineralisation as calculated from estimated POC remineralisation fluxes over integrated remotely sensed PP, for the SO compilation dataset (SPF; 19 ± 15 %, n = 39 and NPF; 10 ± 10 %, n = 29; mean ± SD; t-statistic = 2.75; p-value <0.05; Table B3), was ~ 2 fold higher SPF than NPF, revealing the higher surface carbon export efficiency SPF. Our estimates of % POC remineralised fall within the range of reported export efficiencies throughout the SO (2 - 58 %; Jacquet et al., 2011; Morris et al,, 2007; Savoye et al., 2008). Our values also support the inverse relationship between export efficiency and productivity, with higher export efficiency in areas of lower production (HPLE; High Productivity Low E-ratio, where e-ratio refers to the ratio between export production and net primary productivity, Fan et al., 2020; Maiti et al., 2013). Estimated mesopelagic POC remineralisation has been reported to account for a significant fraction of exported carbon in the PFZ and southwards, from 31 to 97 %, from spring to summer, whereas it only accounts for ~ 50% in the SAZ and SAF, during summer (Cardinal et al., 2005). A combination of variables can influence surface export efficiency and the magnitude of the subsequent mesopelagic remineralisation, even more so when considering longer timescales. These variables include physical dynamics and interlinked biogeochemical factors, i.e., bacterial activity, phytoplankton community structure, zooplankton grazing and nutrient availability (Bopp et al., 2013; Buesseler and Boyd, 2009; Cardinal et al., 2005; Jacquet et al., 2008b; Pyle et al., 2018). In previous studies, supply and loss via physical transport has been deemed negligible relative to decay and loss via production, due to minimal advection and diffusion gradients observed on the timescale of days to weeks. These processes were therefore assumed

to have minimal impact on the mesopelagic signal (Dehairs et al., 1997; Planchon et al., 2013; Rutgers van der Loeff et al., 2011). It has, however, been observed that features such as mesoscale eddies can have an effect on Ba_{xs} distribution by influencing particle patterns on a broad spatial scale, homogenising mesopelagic remineralisation signals by causing relatively flat profiles or shallower remineralisation peaks (Buesseler et al., 2005; Jacquet et al., 2008b). The region of our winter study is known for being a mesoscale eddy hotspot due to the South-West Indian Ridge (Ansorge et al., 2015). In the STZ, extremely dynamic submesoscale activity due to the ARC may indeed have significantly influenced the mesopelagic signal, and may help explain the absence of correlation with integrated surface PP. On the contrary, south of the STF, the significant correlations seem to indicate that physical transport variability is not the main process affecting the mesopelagic Ba_{xs} signal, and that biogeochemical factors may be dominant.

The Fe-limited SAZ (Ryan-Keogh et al., 2018) and AZ (Viljoen et al., 2018) have generally mixed and seasonally changing assemblages of pico-, nano- and micro-phytoplankton (Eriksen et al., 2018; Gall et al., 2001). Diatoms tend to dominate in the silicate-rich waters south of the PF (Petrou et al., 2016; Rembauville et al., 2017; Wright et al., 2010), whilst seasonally silicate-limited waters north of the PF, favour smaller phytoplankton groups (Freeman et al., 2018; Nissen et al., 2018; Trull et al., 2018). HPLE regimes are indeed characteristic of large areas of the SAZ. They are mainly due to surface POC accumulation caused by non-sinking particles, tending towards less efficient export of smaller cells (Fan et al., 2020). Even when large particles are abundant in HPLE surface layers, a complex grazing community may prevent the export of large particles (Dehairs et al., 1992; Lam and Bishop, 2007). This can explain the higher surface carbon export efficiency that we estimate SPF compared to NPF. Export efficiency has also been linked to bacterial productivity with efficient surface remineralisation limiting surface POC export, when most of the water column integrated bacterial productivity

is restricted to the upper mixed layer (Dehairs et al., 1992; Jacquet et al., 2011), which can be the case to varying degrees throughout the SO. In the STZ phytoplankton communities are reported to be dominated by prokaryotic picoplankton including cyanobacteria and prochlorophytes (Mendes et al., 2015). These groups utilise regenerated nutrients in the surface mixed layer tending towards diminished surface export efficiency with high concentrations of non-sinking POC (Fan et al., 2020; Planchon et al. 2013). In addition to this, the potential influence of high submesoscale activity, may explain the low mesopelagic Ba_{xs} measured at the STZ station of this study, despite it being the station with the highest integrated PP (Figure B1). Linking temporally integrated remotely sensed PP to mesopelagic Ba_{xs} stock, coupled with the added influence of physical dynamics affecting surface export efficiencies, along longer timescales, could give better estimates of export and remineralisation signals throughout the SO, on an annual and basin scale. Our estimates of percentage remineralised POC over remotely sensed PP may contribute to the improved modelling of the C cycle over the SO, on an annual timescale.

3.5 Conclusions

Our unique early winter Ba_{xs} data were similar in magnitude and exhibited the same relationship with σ_θ and dissolved O_2 gradients as observed in summer, indicating that processes controlling this signal in summer are still driving the signal in early winter. The expected decline of the mesopelagic Ba_{xs} signal to background values during winter was not observed in this study, supporting the hypothesis that this remineralisation proxy likely has a longer timescale than previously reported. The absolute decline might be delayed due to the cumulative behaviour of mesopelagic Ba_{xs}, ongoing remineralisation and barite precipitation. The "true" SO background value may thus have to be measured at the very end of winter, prior to bloom initiation.

Significant positive correlations north and south of the PF, between mesopelagic Ba_{xs} stock and remotely sensed PP, integrated from September to 1 month before sampling (Sept - T1), in combination with significant Ba_{xs} accumulation trends obtained for the SO compilation dataset, suggest an annual timescale. They may also indicate that physical processes do not dominate the mesopelagic signal on an annual scale, within the SO, and that biogeochemical factors are dominant. There is no significant difference in mesopelagic Ba_{xs} and POC remineralisation, north and south of the PF, but the significantly higher integrated remotely sensed PP to the north when compared to the south, indicates a greater export efficiency south of the PF. This is in accordance with the phenomenon of HPLE regimes which are common throughout the SO, moreso north of the PF than south of the PF (Fan et al., 2020). The longer timescale of Ba_{xs} and the cumulative behaviour of this proxy in the mesopelagic zone make it possible to use Ba_{xs} on an annual scale for the estimation of POC remineralisation fluxes throughout the SO and to better understand how variable environmental factors influence these processes on a basin scale. We believe that the significance of these relationships will improve as more data become available (e.g., GEOTRACES IDP2021), which will assist in better understanding and constraining the timescale of remineralisation and C export efficiency throughout the SO.

3.6 Author contribution

This study was conceptualised by N.R.vH, H.P, G.S and E.B. Formal analysis, investigation and validation of data was carried out by N.R.vH, H.P, G.S, T.J.R-K and T.N.M. N.R.vH and T.J.R-K contributed towards the visualisation of the data. H.P, G.S, T.N.M, A.R, N.L. and E.B contributed towards supervision and resources. Funding was acquired by N.R.vH, T.N.M, A.R and E.B. All authors contributed towards writing, reviewing and editing of the final manuscript.

3.7 Acknowledgments

This work was supported by the ISblue project, Interdisciplinary graduate school for the blue planet (ANR-17-EURE-0015) and co-funded by a grant from the French government under the program "Investissements d'Avenir". International collaboration was made possible by funding received by the French-South African National Research Foundation (NRF) Collaboration (PROTEA; FSTR180418322331), NRF funding (SNA170518231343 and UID 110715) including funding from South African Department of Science and Technology, French Ministry of National Education, Higher Education and Research, and the French Ministry of Foreign Affairs and International Development. We would like to thank the captain and crew of the R/V *SA Agulhas II* for their invaluable efforts, as well as all the research participants who assisted our fieldwork. Thanks to Prof. I Ansorge, Dr M du Plessis and Dr E Portela for their assistance with water mass identification, and Dr C. Jeandel for her invaluable expert insight.

3.8 References

Anilkumar, N. and Sabu, P.: Physical process influencing the ecosystem of the indian sector of southern ocean-An overview, Proc. Indian Natl. Sci. Acad., 83(2), 363–376, doi:10.16943/ptinsa/2017/48960, 2017.

Ansorge, I. J., Jackson, J. M., Reid, K., Durgadoo, J. V, Swart, S. and Eberenz, S.: Evidence of a southward eddy corridor in the South-West Indian ocean, Deep. Res. Part II Top. Stud. Oceanogr., 119, 69–76, doi:10.1016/j.dsr2.2014.05.012, 2015.

Armstrong, R. A., Peterson, M. L., Lee, C. and Wakeham, S. G.: Settling velocity spectra and the ballast ratio hypothesis, Deep. Res. Part II Top. Stud. Oceanogr., 56(18), 1470–1478, doi:10.1016/j.dsr2.2008.11.032, 2009.

Barbur, V. A., Montgomery, D. C. and Peck, E. A.: Introduction to Linear Regression Analysis., Stat., 43(2), 339, doi:10.2307/2348362, 1994.

Behrenfeld, M. J., Boss, E., Siegel, D. A. and Shea, D. M.: Carbon-based ocean productivity and phytoplankton physiology from space, Global Biogeochem. Cycles, 19(1), 1–14, doi:10.1029/2004GB002299, 2005.

Bishop, J. K. B.: The barite-opal-organic carbon association in oceanic particulate matter, Nature, 332(6162), 341–343, doi:10.1038/332341a0, 1988.

Bishop, J. K. B. and Edmond, J. M.: A new large volume filtration system for the sampling of oceanic particulate matter, J. Mar. Res., 34, 181-198, 1976.

Bopp, L., Resplandy, L., Orr, J. C., Doney, S. C., Dunne, J. P., Gehlen, M., Halloran, P., Heinze, C., Ilyina, T., Séférian, R., Tjiputra, J. and Vichi, M.: Multiple stressors of ocean ecosystems in the 21st century: Projections with CMIP5 models, Biogeosciences, 10(10), 6225–6245, doi:10.5194/bg-10-6225-2013, 2013.

Boyd, P. W., Claustre, H., Levy, M., Siegel, D. A. and Weber, T.: Multi-faceted particle pumps drive carbon sequestration in the ocean, Nature, 568(7752), 327–335, doi:10.1038/s41586-019-1098-2, 2019.

Broecker, W. S., Takahashi, T. and Takahashi, T.: Sources and flow patterns of deep-ocean waters as deduced from potential temperature, salinity, and initial phosphate concentration, J. Geophys. Res. Ocean., 90(C4), 6925–6939, doi:10.1029/JC090iC04p06925, 1985.

Buesseler, K. O.: The decoupling of production and particulate export in the surface ocean, Global Biogeochem. Cycles, 12(2), 297–310, doi:10.1029/97GB03366, 1998.

Buesseler, K. O., Andrews, J. E., Pike, S. M., Charette, M. A., Goldson, L. E., Brzezinski, M. A. and Lance, V. P.: Particle export during the Southern Ocean Iron Experiment (SOFeX), Limnol. Oceanogr., 50(1), 311–327, doi:10.4319/lo.2005.50.1.0311, 2005.

Buesseler, K. O. and Boyd, P. W.: Shedding light on processes that control particle export and flux attenuation in the twilight zone of the open ocean, Limnol. Oceanogr., 54(4), 1210–1232, doi:10.4319/lo.2009.54.4.1210, 2009.

Cardinal, D., Dehairs, F., Cattaldo, T. and André, L.: Geochemistry of suspended particles in the Subantarctic and Polar Frontal zones south of Australia: Constraints on export and advection processes, J. Geophys. Res. Ocean., 106(C12), 31637–31656, doi:10.1029/2000JC000251, 2001.

Cardinal, D., Savoye, N., Trull, T. W., André, L., Kopczynska, E. E. and Dehairs, F.: Variations of carbon remineralisation in the Southern Ocean illustrated by the Baxs proxy, Deep. Res. Part I Oceanogr. Res. Pap., 52(2), 355–370, doi:10.1016/j.dsr.2004.10.002, 2005.

Cavan, E. L., Le Moigne, F. A. C., Poulton, A. J., Tarling, G. A., Ward, P., Daniels, C. J., Fragoso, G. M. and Sanders, R. J.: Attenuation of particulate organic carbon flux in the Scotia Sea, Southern Ocean, is controlled by zooplankton fecal pellets, Geophys. Res. Lett., 42(3), 821–830, doi:10.1002/2014GL062744, 2015.

Cutter, G., Casciotti, K., Croot, P., Geibert, W., Heimbürger, L.-E., Lohan, M., Planquette, H. and van de Flierdt, T.: Sampling and Sample-handling Protocols for GEOTRACES Cruises. Version 3, 139pp. & Appendices [online] Available from: http://www.geotraces.org/images/stories/documents/intercalibration/Cookbook.pdf, 2017.

de Boyer Montégut, C., Madec, G., Fischer, A. S., Lazar, A. and Iudicone, D.: Mixed layer depth over the global ocean: An examination of profile data and a profile-based climatology, J. Geophys. Res. C Ocean., 109(12), 1–20, doi:10.1029/2004JC002378, 2004.

Dehairs, F., Baeyens, W. and Goeyens, L.: Accumulation of Suspended Barite at Mesopelagic Depths and Export Production in the Southern Ocean, Science (80-.)., 258(5086), 1332–1335, doi:10.1126/SCIENCE.258.5086.1332, 1992.

Dehairs, F., Chesselet, R. and Jedwab, J.: Discrete suspended particles of barite and the barium cycle in the open ocean, Earth Planet. Sci. Lett., 49(2), 528–550, doi:10.1016/0012-821X(80)90094-1, 1980.

Dehairs, F., Goeyens, L., Stroobants, N., Bernard, P., Goyet, C., Poisson, A. and Chesselet, R.: On suspended barite and the oxygen minimum in the Southern Ocean, Global Biogeochem. Cycles, 4(1), 85–102, doi:10.1029/GB004I001P00085, 1990.

Dehairs, F., Shopova, D., Ober, S., Veth, C. and Goeyens, L.: Particulate barium stocks and oxygen consumption in the Southern Ocean mesopelagic water column during spring and early summer: Relationship with export production, Deep. Res. Part II Top. Stud. Oceanogr., 44(1–2), 497–516, doi:10.1016/S0967-0645(96)00072-0, 1997.

Dehairs, F., Stroobants, N. and Goeyens, L.: Suspended barite as a tracer of biological activity in the Southern Ocean, Mar. Chem., 35(1–4), 399–410, doi:10.1016/S0304-4203(09)90032-9, 1991.

de Jong, E., Vichi, M., Mehlmann, C. B., Eayrs, C., De Kock, W., Moldenhauer, M. and Audh, R. R.: Sea Ice conditions within the Antarctic Marginal Ice Zone in winter 2017, onboard the SA Agulhas II., Univ. Cape Town, PANGAEA, doi:https://doi.org/10.1594/PANGAEA.885211, 2018.

DeVries, T. and Weber, T.: The export and fate of organic matter in the ocean: New constraints from combining satellite and oceanographic tracer observations, Global Biogeochem. Cycles, 31(3), 535–555, doi:10.1002/2016GB005551, 2017.

Ducklow, H. W., Steinberg, D. K. and Buesseler, K. O.: Upper ocean carbon export and the biological pump, Oceanography, 14(SPL.ISS. 4), 50–58, doi:10.5670/oceanog.2001.06, 2001.

Dymond, J., Suess, E. and Lyle, M.: Barium in Deep-Sea Sediment: A Geochemical Proxy for Paleoproductivity, Paleoceanography, 7(2), 163–181, doi:10.1029/92PA00181, 1992.

Ehrhardt, M. (Manfred), Grasshoff, K., Kremling, K. (Klaus) and Almgren, T., Eds.: Methods of seawater analysis / edited by K. Grasshoff, M. Ehrhardt, K. Kremling ; with contributions by T. Almgren ... [et al.], Verlag Chemie, Weinheim., 1983.

Eriksen, R., Trull, T. W., Davies, D., Jansen, P., Davidson, A. T., Westwood, K. and Van Den Enden, R.: Seasonal succession of phytoplankton community structure from autonomous sampling at the Australian Southern Ocean Time Series (SOTS) observatory, Mar. Ecol. Prog. Ser., 589, 13–21, doi:10.3354/meps12420, 2018.

Fan, G., Han, Z., Ma, W., Chen, S., Chai, F., Mazloff, M. R., Pan, J. and Zhang, H.: Southern Ocean carbon export efficiency in relation to temperature and primary productivity, Sci. Rep., 10(1), 1–11, doi:10.1038/s41598-020-70417-z, 2020.

Ferrari, R. and Nikurashin, M.: Suppression of eddy diffusivity across jets in the Southern Ocean, J. Phys. Oceanogr., 40(7), 1501–1519, doi:10.1175/2010JPO4278.1, 2010.

Freeman, N. M., Lovenduski, N. S., Munro, D. R., Krumhardt, K. M., Lindsay, K., Long, M. C. and Maclennan, M.: The Variable and Changing Southern Ocean Silicate Front: Insights from the CESM Large Ensemble, Global Biogeochem. Cycles, 32(5), 752–768, doi:10.1029/2017GB005816, 2018.

Friedlingstein, P., Jones, M. W., O'Sullivan, M., Andrew, R. M., Hauck, J., Peters, G. P., Peters, W., Pongratz, J., Sitch, S., Le Quéré, C., Bakker, D. C. E., Canadell, J. G., Ciais, P., Jackson, R. B., Anthoni, P., Barbero, L., Bastos, A., Bastrikov, V., Becker, M., Bopp, L., Buitenhuis, E., Chandra, N., Chevallier, F., Chini, L. P., Currie, K. I., Feely, R. A., Gehlen, M., Gilfillan, D., Gkritzalis, T., Goll, D. S., Gruber, N., Gutekunst, S., Harris, I., Haverd, V., Houghton, R. A., Hurtt, G., Ilyina, T., Jain, A. K., Joetzjer, E., Kaplan, J. O., Kato, E., Klein Goldewijk, K., Korsbakken, J. I., Landschützer, P., Lauvset, S. K., Lefèvre, N., Lenton, A., Lienert, S., Lombardozzi, D., Marland, G., McGuire, P. C., Melton, J. R., Metzl, N., Munro, D. R., Nabel, J. E. M. S., Nakaoka, S.-I., Neill, C., Omar, A. M., Ono, T., Peregon, A., Pierrot, D., Poulter, B., Rehder, G., Resplandy, L., Robertson, E., Rödenbeck, C., Séférian, R., Schwinger, J., Smith, N., Tans, P. P., Tian, H., Tilbrook, B., Tubiello, F.

N., van der Werf, G. R., Wiltshire, A. J. and Zaehle, S.: Global Carbon Budget 2019, Earth Syst. Sci. Data, 11(4), 1783–1838, doi:10.5194/essd-11-1783-2019, 2019.

Gall, M. P., Boyd, P. W., Hall, J., Safi, K. A. and Chang, H.: Phytoplankton processes. Part 1: Community structure during the Southern Ocean Iron RElease Experiment (SOIREE), Deep. Res. Part II Top. Stud. Oceanogr., 48(11–12), 2551–2570, doi:10.1016/S0967-0645(01)00008-X, 2001.

GEOTRACES Intermediate Data Product Group: The GEOTRACES Intermediate Data Product 2021 (IDP2021), NERC EDS British Oceanographic Data Centre NOC, doi: 10.5285/cf2d9ba9-d51d-3b7c-e053-8486abc0f5fd, 2021.

Gill, A. E.: Atmosphere-ocean dynamics, NEW YORK, U.S.A., ACADEMIC PRESS INC., 1982.

Gregor, L., Lebehot, A. D., Kok, S. and Scheel Monteiro, P. M.: A comparative assessment of the uncertainties of global surface ocean CO2 estimates using a machine-learning ensemble (CSIR-ML6 version 2019a)-Have we hit the wall?, Geosci. Model Dev., 12(12), 5113–5136, doi:10.5194/gmd-12-5113-2019, 2019.

Gruber, N., Landschützer, P. and Lovenduski, N. S.: The variable southern ocean carbon sink, Ann. Rev. Mar. Sci., 11(September), 159–186, doi:10.1146/annurev-marine-121916-063407, 2019.

Honjo, S., Eglinton, T. I., Taylor, C. D., Ulmer, K. M., Sievert, S. M., Bracher, A., German, C. R., Edgcomb, V., Francois, R., Deboraiglesias-Rodriguez, M., Van Mooy, B. and Repeta, D. J.: Understanding the role of the biological pump in the global carbon cycle: An imperative for ocean science, Oceanography, 27(3), 10–16, doi:10.5670/oceanog.2014.78, 2014.

Ito, T., Follows, M. J. and Boyle, E. A.: Is AOU a good measure of respiration in the oceans?, Geophys. Res. Lett., 31(17), 1–4, doi:10.1029/2004GL020900, 2004.

Jacquet, S. H. M., Dehairs, F., Cardinal, D., Navez, J. and Delille, B.: Barium distribution across the Southern Ocean frontal system in the Crozet-Kerguelen Basin, Mar. Chem., 95(3–4), 149–162, doi:10.1016/j.marchem.2004.09.002, 2005.

Jacquet, S. H. M., Dehairs, F., Dumont, I., Becquevort, S., Cavagna, A. J. and Cardinal, D.: Twilight zone organic carbon remineralization in the Polar Front Zone and Subantarctic Zone south of Tasmania, Deep. Res. Part II Top. Stud. Oceanogr., 58(21–22), 2222–2234, doi:10.1016/j.dsr2.2011.05.029, 2011.

Jacquet, S. H. M., Dehairs, F., Elskens, M., Savoye, N. and Cardinal, D.: Barium cycling along WOCE SR3 line in the Southern Ocean, Mar. Chem., 106(1-2 SPEC. ISS.), 33–45, doi:10.1016/j.marchem.2006.06.007, 2007.

Jacquet, S. H. M., Dehairs, F., Lefèvre, D., Cavagna, A. J., Planchon, F., Christaki, U., Monin, L., André, L., Closset, I. and Cardinal, D.: Early spring mesopelagic carbon remineralization and transfer efficiency in the naturally iron-fertilized Kerguelen area, Biogeosciences, 12(6), 1713–1731, doi:10.5194/bg-12-1713-2015, 2015.

Jacquet, S. H. M., Dehairs, F., Savoye, N., Obernosterer, I., Christaki, U., Monnin, C. and Cardinal, D.: Mesopelagic organic carbon remineralization in the Kerguelen Plateau region tracked by biogenic particulate Ba, Deep. Res. Part II Top. Stud. Oceanogr., 55(5–7), 868–879, doi:10.1016/j.dsr2.2007.12.038, 2008a.

Jacquet, S. H. M., Savoye, N., Dehairs, F., Strass, V. H. and Cardinal, D.: Mesopelagic carbon remineralization during the European Iron Fertilization Experiment, Global Biogeochem. Cycles, 22(1), 1–9, doi:10.1029/2006GB002902, 2008b.

Jochum, K. P., Nohl, U., Herwig, K., Lammel, E., Stoll, B. and Hofmann, A. W.: GeoReM: A new geochemical database for reference materials and isotopic standards, Geostand. Geoanalytical Res., 29(3), 333–338, doi:10.1111/j.1751-908x.2005.tb00904.x, 2005.

Kokoska, S. and Zwillinger, D.: CRC Standard Probability and Statistics Tables and Formulae, Student Edition., 2000.

Lam, P. J. and Bishop, J. K. B.: High biomass, low export regimes in the Southern Ocean, Deep. Res. Part II Top. Stud. Oceanogr., 54(5–7), 601–638, doi:10.1016/j.dsr2.2007.01.013, 2007.

Laurenceau-Cornec, E. C., Trull, T. W., Davies, D. M., Bray, S. G., Doran, J., Planchon, F., Carlotti, F., Jouandet, M. P., Cavagna, A. J., Waite, A. M. and Blain, S.: The relative importance of phytoplankton aggregates and zooplankton fecal pellets to carbon export: Insights from free-drifting sediment trap deployments in naturally iron-fertilised waters near the Kerguelen Plateau, Biogeosciences, 12(4), 1007–1027, doi:10.5194/BG-12-1007-2015, 2015.

Le Moigne, F. A. C.: Pathways of Organic Carbon Downward Transport by the Oceanic Biological Carbon Pump, Front. Mar. Sci., 6, doi:10.3389/fmars.2019.00634, 2019.

Legeleux, F. and Reyss, J. L.: 228Ra/226Ra activity ratio in oceanic settling particles: Implications regarding the use of barium as a proxy for paleoproductivity reconstruction, Deep. Res. Part I Oceanogr. Res. Pap., 43(11–12), 1857–1863, doi:10.1016/S0967-0637(96)00086-6, 1996.

Lemaitre, N., Planquette, H., Planchon, F., Sarthou, G., Jacquet, S., García-Ibáñez, M. I., Gourain, A., Cheize, M., Monin, L., André, L., Laha, P., Terryn, H. and Dehairs, F.: Particulate barium tracing of significant mesopelagic carbon remineralisation in the North Atlantic, Biogeosciences, 15(8), 2289–2307, doi:10.5194/bg-15-2289-2018, 2018.

Maiti, K., Charette, M. A., Buesseler, K. O. and Kahru, M.: An inverse relationship between production and export efficiency in the Southern Ocean, Geophys. Res. Lett., 40(8), 1557–1561, doi:10.1002/GRL.50219, 2013.

Marsay, C. M., Sanders, R. J., Henson, S. A., Pabortsava, K., Achterberg, E. P. and Lampitt, R. S.: Attenuation of sinking particulate organic carbon flux through the mesopelagic ocean, Proc. Natl. Acad. Sci. U. S. A., 112(4), 1089–1094, doi:10.1073/pnas.1415311112, 2015.

McDonnell, A. M. P. and Buesseler, K. O.: Variability in the average sinking velocity of marine particles, Limnol. Oceanogr., 55(5), 2085–2096, doi:10.4319/LO.2010.55.5.2085, 2010.

Mendes, C. R. B., Kerr, R., Tavano, V. M., Cavalheiro, F. A., Garcia, C. A. E., Gauns Dessai, D. R. and Anilkumar, N.: Cross-front phytoplankton pigments and chemotaxonomic groups in the Indian sector of the Southern Ocean, Deep. Res. Part II Top. Stud. Oceanogr., 118, 221–232, doi:10.1016/j.dsr2.2015.01.003, 2015.

Morris, P. J., Sanders, R., Turnewitsch, R. and Thomalla, S.: 234Th-derived particulate organic carbon export from an island-induced phytoplankton bloom in the Southern Ocean, Deep Sea Res. Part II Top. Stud. Oceanogr., 54(18–20), 2208–2232, doi:10.1016/J.DSR2.2007.06.002, 2007.

Nissen, C., Vogt, M., Münnich, M., Gruber, N. and Haumann, F. A.: Factors controlling coccolithophore biogeography in the Southern Ocean, Biogeosciences, 15(22), 6997–7024, doi:10.5194/bg-15-6997-2018, 2018.

Orsi, A. H., Whitworth, T. and Nowlin, W. D.: On the meridional extent and fronts of the Antarctic Circumpolar Current, Deep. Res. Part I, 42(5), 641–673, doi:10.1016/0967-0637(95)00021-W, 1995.

Passow, U. and Carlson, C. A.: The biological pump in a high CO2 world, Mar. Ecol. Prog. Ser., 470(2), 249–271, doi:10.3354/meps09985, 2012.

Petrou, K., Kranz, S. A., Trimborn, S., Hassler, C. S., Ameijeiras, S. B., Sackett, O., Ralph, P. J. and Davidson, A. T.: Southern Ocean phytoplankton physiology in a changing climate, J. Plant Physiol., 203, 135–150, doi:https://doi.org/10.1016/j.jplph.2016.05.004, 2016.

Planchon, F., Cavagna, A. J., Cardinal, D., André, L. and Dehairs, F.: Late summer particulate organic carbon export and twilight zone remineralisation in the Atlantic sector of the Southern Ocean, Biogeosciences, 10(2), 803–820, doi:10.5194/bg-10-803-2013, 2013.

Planquette, H. and Sherrell, R. M.: Sampling for particulate trace element determination using water sampling bottles: Methodology and comparison to in situ pumps, Limnol. Oceanogr. Methods, 10(5), 367–388, doi:10.4319/lom.2012.10.367, 2012.

Pollard, R. T., Lucas, M. I. and Read, J. F.: Physical controls on biogeochemical zonation in the Southern Ocean, Deep. Res. Part II Top. Stud. Oceanogr., 49(16), 3289–3305, doi:10.1016/S0967-0645(02)00084-X, 2002.

Pyle, K. M., Hendry, K. R., Sherrell, R. M., Legge, O., Hind, A. J., Bakker, D., Venables, H. and Meredith, M. P.: Oceanic fronts control the distribution of dissolved barium in the Southern Ocean, Mar. Chem., 204(July), 95–106, doi:10.1016/j.marchem.2018.07.002, 2018.

Rembauville, M., Briggs, N., Ardyna, M., Uitz, J., Catala, P., Penkerc'h, C., Poteau, A., Claustre, H. and Blain, S.: Plankton Assemblage Estimated with BGC-Argo Floats in the Southern Ocean: Implications for Seasonal Successions and Particle Export, J. Geophys. Res. Ocean., 122(10), 8278–8292, doi:10.1002/2017JC013067, 2017.

Riebesell, U.: Particle aggregation during a diatom bloom. II. Biological aspects, Mar. Ecol. Prog. Ser., 69(3), 281–291, doi:10.3354/meps069281, 1991.

Rio, M. H., Guinehut, S. and Larnicol, G.: New CNES-CLS09 global mean dynamic topography computed from the combination of GRACE data, altimetry, and in situ measurements, J. Geophys. Res. Ocean., 116(7), 1–25, doi:10.1029/2010JC006505, 2011.

Robinson, C., Steinberg, D. K., Anderson, T. R., Arístegui, J., Carlson, C. A., Frost, J. R., Ghiglione, J. F., Hernández-León, S., Jackson, G. A., Koppelmann, R., Quéguiner, B., Ragueneau, O., Rassoulzadegan, F., Robison, B. H., Tamburini, C., Tanaka, T., Wishner,

K. F. and Zhang, J.: Mesopelagic zone ecology and biogeochemistry - A synthesis, Deep. Res. Part II Top. Stud. Oceanogr., 57(16), 1504–1518, doi:10.1016/j.dsr2.2010.02.018, 2010.

Rosengard, S. Z., Lam, P. J., Balch, W. M., Auro, M. E., Pike, S., Drapeau, D. and Bowler, B.: Carbon export and transfer to depth across the Southern Ocean Great Calcite Belt, Biogeosciences, 12(13), 3953–3971, doi:10.5194/bg-12-3953-2015, 2015.

Rutgers van der Loeff Michiel, M., Cai, P. H., Stimac, I., Bracher, A., Middag, R., Klunder, M. B. and van Heuven, S. M. A. C.: 234Th in surface waters: Distribution of particle export flux across the Antarctic Circumpolar Current and in the Weddell Sea during the GEOTRACES expedition ZERO and DRAKE, Deep. Res. Part II Top. Stud. Oceanogr., 58(25–26), 2749–2766, doi:10.1016/j.dsr2.2011.02.004, 2011.

Ryan-Keogh, T. J., Thomalla, S. J., Mtshali, T. N., Van Horsten, N. R. and Little, H. J.: Seasonal development of iron limitation in the sub-Antarctic zone, Biogeosciences, 15(14), 4647–4660, doi:10.5194/bg-15-4647-2018, 2018.

Sarmiento, J., & Gruber, N. Ocean Biogeochemical Dynamics, Princeton University Press, Princeton, Oxford doi:10.2307/j.ctt3fgxqx, 2006.

Sathyendranath, S., Brewin, R. J. W., Brockmann, C., Brotas, V., Calton, B., Chuprin, A., Cipollini, P., Couto, A. B., Dingle, J., Doerffer, R., Donlon, C., Dowell, M., Farman, A., Grant, M., Groom, S., Horseman, A., Jackson, T., Krasemann, H., Lavender, S., Martinez-Vicente, V., Mazeran, C., Mélin, F., Moore, T. S., Müller, D., Regner, P., Roy, S., Steele, C. J., Steinmetz, F., Swinton, J., Taberner, M., Thompson, A., Valente, A., Zühlke, M., Brando, V. E., Feng, H., Feldman, G., Franz, B. A., Frouin, R., Gould, R. W., Hooker, S. B., Kahru, M., Kratzer, S., Mitchell, B. G., Muller-Karger, F. E., Sosik, H. M., Voss, K. J., Werdell, J. and Platt, T.: An ocean-colour time series for use in climate studies: The

experience of the ocean-colour climate change initiative (OC-CCI), Sensors (Switzerland), 19(19), doi:10.3390/s19194285, 2019.

Savoye, N., Trull, T. W., Jacquet, S. H. M., Navez, J. and Dehairs, F.: 234Th-based export fluxes during a natural iron fertilization experiment in the Southern Ocean (KEOPS), Deep Sea Res. Part II Top. Stud. Oceanogr., 55(5–7), 841–855, doi:10.1016/J.DSR2.2007.12.036, 2008.

Schlitzer, R.: Carbon export fluxes in the Southern Ocean: Results from inverse modeling and comparison with satellite-based estimates, Deep. Res. Part II Top. Stud. Oceanogr., 49(9–10), 1623–1644, doi:10.1016/S0967-0645(02)00004-8, 2002.

Shopova, D., Dehairs, F. and Baeyens, W.: A simple model of biogeochemical element distribution in the oceanic water column, J. Mar. Syst., 6(4), 331–344, doi:10.1016/0924-7963(94)00032-7, 1995.

Sigman, D. M., Hain, M. P. and Haug, G. H.: The polar ocean and glacial cycles in atmospheric CO2 concentration, Nature, 466(7302), 47–55, doi:10.1038/nature09149, 2010.

Sternberg, E., Jeandel, C., Robin, E. and Souhaut, M.: Seasonal cycle of suspended barite in the mediterranean sea, Geochim. Cosmochim. Acta, 72(16), 4020–4034, doi:10.1016/J.GCA.2008.05.043, 2008.

Sternberg, E., Tang, D., Ho, T. Y., Jeandel, C. and Morel, F. M. M.: Barium uptake and adsorption in diatoms, Geochim. Cosmochim. Acta, 69(11), 2745–2752, doi:10.1016/j.gca.2004.11.026, 2005.

Swart, S., Speich, S., Ansorge, I. J. and Lutjeharms, J. R. E.: An altimetry-based gravest empirical mode south of Africa: 1. Development and validation, J. Geophys. Res. Ocean., 115(3), 1–19, doi:10.1029/2009JC005299, 2010.

Takahashi, T., Sweeney, C., Hales, B., Chipman, D. W., Goddard, J. G., Newberger, T., Iannuzzi, R. A. and Sutherland, S. C.: The changing carbon cycle in the southern ocean, Oceanography, 25(3), 26–37, doi:10.5670/oceanog.2012.71, 2012.

Taylor, S. R. and McLennan, S. M.: The continental crust: Its composition and evolution, Blackwell Scientific Pub., Palo Alto, CA, United States. [online] Available from: https://www.osti.gov/biblio/6582885, 1985.

Thomalla, S. J., Fauchereau, N., Swart, S. and Monteiro, P. M. S.: Regional scale characteristics of the seasonal cycle of chlorophyll in the Southern Ocean, Biogeosciences, 8(10), 2849–2866, doi:10.5194/bg-8-2849-2011, 2011.

Trull, T. W., Passmore, A., Davies, D. M., Smit, T., Berry, K. and Tilbrook, B.: Distribution of planktonic biogenic carbonate organisms in the Southern Ocean south of Australia: A baseline for ocean acidification impact assessment, Biogeosciences, 15(1), 31–49, doi:10.5194/bg-15-31-2018, 2018.

Twining, B. S., Nodder, S. D., King, A. L., Hutchins, D. A., LeCleir, G. R., DeBruyn, J. M., Maas, E. W., Vogt, S., Wilhelm, S. W. and Boyd, P. W.: Differential remineralization of major and trace elements in sinking diatoms, Limnol. Oceanogr., 59(3), 689–704, doi:https://doi.org/10.4319/lo.2014.59.3.0689, 2014.

van Beek, P., François, R., Conte, M., Reyss, J. L., Souhaut, M. and Charette, M.: 228Ra/226Ra and 226Ra/Ba ratios to track barite formation and transport in the water column, Geochim. Cosmochim. Acta, 71(1), 71–86, doi:10.1016/j.gca.2006.07.041, 2007.

Viljoen, J. J., Philibert, R., Van Horsten, N., Mtshali, T., Roychoudhury, A. N., Thomalla, S. and Fietz, S.: Phytoplankton response in growth, photophysiology and community structure to iron and light in the Polar Frontal Zone and Antarctic waters, Deep. Res. Part I Oceanogr. Res. Pap., 141(September), 118–129, doi:10.1016/j.dsr.2018.09.006, 2018.

Wright, S. W., van den Enden, R. L., Pearce, I., Davidson, A. T., Scott, F. J. and Westwood, K. J.: Phytoplankton community structure and stocks in the Southern Ocean (30-80°E) determined by CHEMTAX analysis of HPLC pigment signatures, Deep. Res. Part II Top. Stud. Oceanogr., 57(9–10), 758–778, doi:10.1016/j.dsr2.2009.06.015, 2010.

Zhuang, J.: xESMF: Universal Regridder for GeospatialData, https://github.com/JiaweiZhuang/xESMF, 2018.

Chapter 4: Discussion, Conclusions and Perspectives

4.1 Discussion and Conclusions

The data obtained from this study contributes to spatial and temporal observational gaps with regards to marine Fe biogeochemistry in the SO, as well as insights into the seasonal accumulation of Ba_{xs} as a remineralisation proxy. Recent winter studies, including this study, have very recently started giving insight into the seasonal cycle of dFe in the HNLC regions of the open SO. Despite what was expected, winter surface (< 200 m) and intermediate (200 - 1000 m) water dFe concentrations were not significantly different to the co-located summer concentrations in the Indian and Atlantic basins, and summer dFe concentrations were significantly higher than winter concentrations in the Pacific basin. The higher concentrations observed in the Atlantic basin, from the compilation data comparisons, can be linked to increased lateral advection inputs from the Antarctic Peninsula (De Jong et al., 2012), as well as inter-basin water mass age differences (Ellwood et al., 2008). It is also believed that variable hydrothermal inputs and ligand concentration differences would affect inter- and intra-basin differences in dFe distributions (Tagliabue et al., 2012; Thuróczy et al. 2011).

During this study, surface water dFe concentrations at all stations resembled end of summer observations, indicating that during July there has yet to be noticeable replenishment of surface water dFe concentrations. Surface water dFe depletion increased southwards, whereas macronutrients were high at all stations in the SO, characteristic of the HNLC SO (Martin, 1990; Martin et al., 1990). An intermediate water peak was observed on water column profiles for concentrations of all nutrients, including dFe, as well as the remineralisation proxy, Ba_{xs}, also resembling distributions reported from studies throughout the SO. The separation between the MLD and the ferricline was also similar to previous observations, hindering the supply of subsurface dFe to the upper surface mixed layer. These distributions highlight the significance

of remineralisation within intermediate waters and the lack of surface mixed layer replenishment during early winter in the HNLC open waters of the western SIO.

Intermediate water remineralisation was assessed utilising both the AOU and Ba_{xs} remineralisation proxies. Although both proxies assess remineralisation, they integrate remineralisation over different temporal and spatial scales. AOU integrates remineralisation on timescales of years to decades in water masses as they are subducted, accumulating nutrients as the water masses age via continuous remineralisation (Ito et al., 2004; Tagliabue et al., 2019). The mesopelagic Ba_{xs} signal has been linked to the rate of surface POC export and integrates over seasonal to annual timescales, linked to surface export instead of water mass subduction (Chapter 3, van Horsten et al., In review). Integrated mesopelagic remineralised dFe stock estimates were determined using the AOU proxy (Chapter 2) and POC remineralisation fluxes were estimated using the Ba_{xs} proxy (Chapter 3, van Horsten et al., In review), along the 30°E line. The remineralised dFe stock estimates, using the AOU proxy, increased steadily northwards along the transect. It was estimated that up to 100% of the observed mesopelagic dFe stock is supplied by remineralisation and a minimum of 20 to 60% is lost via scavenging, at all but one station (56°S) along the transect, where a possible unaccounted for dFe input resulted in a remineralisation stock less than 100%. Ba_{xs} estimated POC remineralisation fluxes also increased from the AZ up to maximum values in the SAZ, but the lowest POC remineralisation flux was estimated in the STZ. The subsurface remineralisation signal for dFe and macronutrients, observed at 41°S, therefore seems to be linked more to advected water masses, transporting remineralised nutrients into the STZ rather than from surface export.

Fe remineralisation fluxes were calculated and integrated over the mesopelagic depth range, using POC remineralisation fluxes obtained from the Ba_{xs} proxy method (See section 3.2.4 for detailed methodology), in conjunction with the estimated Fe:C ratios, using dFe/AOU linear regression slopes. Remineralisation fluxes ranged from 0.68 ± 0.14 nmol dFe m^{-3} yr^{-1} to 16.66

± 1.36 nmol dFe m^{-3} yr^{-1} for the study area, increasing northwards from the AZ (1.80 ± 0.45 nmol dFe m^{-3} yr^{-1}), to a maximum in the SAZ (16.66 ± 1.36 nmol dFe m^{-3} yr^{-1}). Fluxes in the AZ (1.80 - 3.51 nmol dFe m^{-3} yr^{-1}) were comparable to values observed in the Southern Pacific Ocean of ~ 2 nmol m^{-3} yr^{-1} (Tagliabue et al., 2019), whereas fluxes in the SAZ (9.86 - 16.66 nmol dFe m^{-3} yr^{-1}) were an order of magnitude larger. The lowest remineralisation flux was in the oligotrophic STZ (0.68 ± 0.14 nmol dFe m^{-3} yr^{-1}). The Fe remineralisation fluxes estimated from the POC remineralisation fluxes, using the Ba_{xs} proxy, are indicative of surface export and subsequent mesopelagic remineralisation, on a seasonal to annual timescale (Chapter 3, van Horsten et al., In Review). The larger remineralisation fluxes estimated in the SAZ can be linked to a relatively higher productive bloom season, evident from the latitudinal trend of the integrated remotely sensed PP along the transect (Figure B1). Although remineralisation fluxes were larger north of the PF, export efficiencies were found to be higher south of the PF, when compared to integrated remotely sensed PP (Chapter 3, van Horsten et al., In review).

The decoupling observed between remineralisation fluxes, magnitude of integrated remotely sensed PP and the export efficiencies, gives insight into the fact that PP alone, does not drive the magnitude of mesopelagic remineralisation in the open waters of the SO (Figure 4.1). In fact, HPLE regimes which are common throughout the SO, more so north of the PF than south of the PF (Fan et al., 2020), can be a significant driving factor in the magnitude of mesopelagic remineralisation throughout the SO and thereby the internal cycling of Fe.

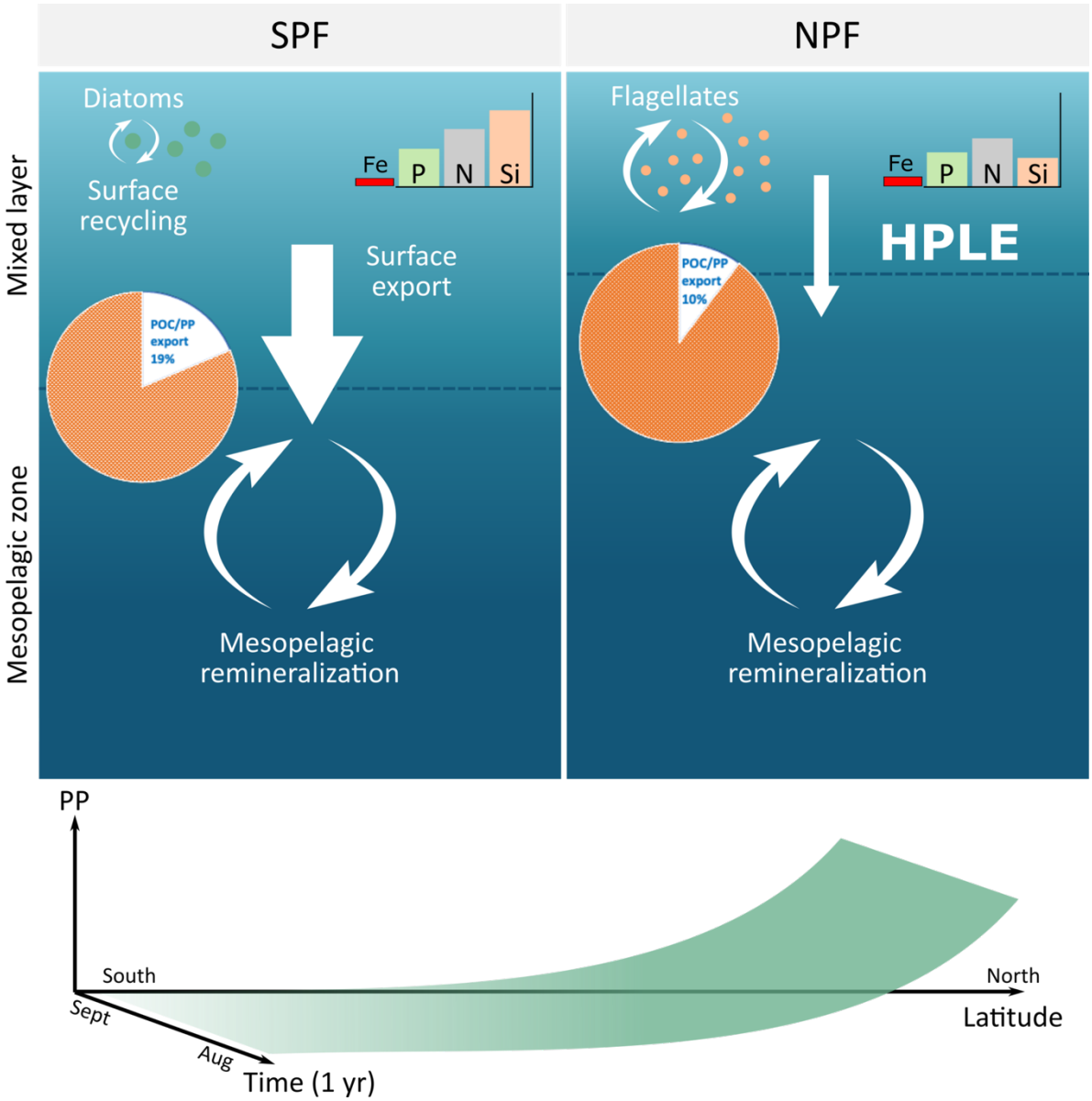

Figure 4.1: Schematic diagram highlighting the contrast between the two zones when comparing surface export in the Fe-limited HNLC SO, SPF and NPF. SPF is diatom dominated, with high concentrations of macronutrients, low surface layer recycling and more efficient surface export despite low PP. NPF is flagellate dominated, tending towards Si limitation, increased surface recycling and less efficient surface export, resulting in comparable mesopelagic remineralisation despite higher PP in the NPF zone, indicative of a high productivity, low export regime whereas SPF has a higher surface export efficiency (created by Dr Llopis Monferrer).

4.2 Perspectives

Although we are aware that scavenging affects dFe distributions, the magnitude to which this process influences observations is still unknown (Achterberg et al., 2018; Boyd and Ellwood, 2010; Tagliabue et al., 2016; 2019). Additional measurements of Fe pools, other than dFe, and fluxes are necessary to better understand the various mechanisms influencing internal cycling (Tagliabue et al., 2019). The balance between the preformed and remineralised components of

the internal cycling of PO_4^{3-} is not as clear for dFe due to scavenging, therefore PO_4^{3-} is used in conjunction with AOU to assess dFe remineralisation, based on the Fe:P cellular ratios of SO phytoplankton (Ito and Follows, 2005; Parekh et al., 2005; Twining et al., 2014). Better insight into the magnitude of scavenging is needed in order to better quantify net dFe remineralisation fluxes in intermediate waters throughout the SO, as this method does not take that into account.

To further facilitate our understanding of the SO Fe biogeochemical cycling we require further investigation into the seasonality and spatial variability with regards to bacterial community, organic speciation and the particulate and colloidal fractions of Fe in the SO. The seasonality of the bacterial community and ligand concentrations could shed light on the inter- and intra-basin trends we observe in the current dFe observations, as well as possible influences on the magnitude of remineralisation and accumulation of nutrients within the SO interior. A better understanding of the interplay between the particulate and dissolved/colloidal fractions of Fe, in conjunction with the organic speciation, can be vital to a clearer characterisation of scavenging rates, and how this affects the temporal and spatial distributions of Fe throughout the water column. It has previously been suggested that colloidal Fe aggregation and scavenging are additional processes that drive the observed loss of dFe from the euphotic zone (Mtshali et al., 2019), these processes could very well be significant within the mesopelagic zone.

These further observations would provide the data needed to determine stocks and residence times of dFe more accurately throughout the SO, contributing useful information to increase the accuracy of estimates of internal cycling of Fe in the SO and how this will change with climate change. Winter studies have thus far been conducted in July and have not shown any significant surface water dFe replenishment to induce bloom initiation. It might be that the time

of sampling thus far has been too early to observe this replenishment; sampling should be conducted at the start of spring, directly before bloom initiation.

It may be useful to compare net dFe remineralisation fluxes, deduced from dFe/AOU slopes to colloidal Fe concentrations, which could shed light on the possible influence by the interplay between soluble and colloidal Fe (Fitzsimmons et al., 2014; Nishioka et al., 2001; Tagliabue et al., 2019; Wu et al., 2001). Factors that influence the internal cycling of Fe, such as phytoplankton community structure, surface water Fe availability, concentrations of strong Fe-binding ligands, bacterial activity and Fe speciation, will significantly influence the future internal cycling of Fe, intermediate water accumulation of Fe (Tagliabue et al., 2019) and thereby the resupply of Fe to surface waters.

References

Achterberg, E. P., Steigenberger, S., Marsay, C. M., Lemoigne, F. A. C., Painter, S. C., Baker, A. R., Connelly, D. P., Moore, C. M., Tagliabue, A., & Tanhua, T. (2018). Iron Biogeochemistry in the High Latitude North Atlantic Ocean. *Scientific Reports*, *8*(1), 1–15. https://doi.org/10.1038/s41598-018-19472-1

Boyd, P. W., & Ellwood, M. J. (2010). The biogeochemical cycle of iron in the ocean. *Nature Geoscience*, *3*(10), 675–682. https://doi.org/10.1038/ngeo964

De Jong, J., Schoemann, V., Lannuzel, D., Croot, P., De Baar, H., & Tison, J. L. (2012). Natural iron fertilization of the Atlantic sector of the Southern Ocean by continental shelf sources of the Antarctic Peninsula. *Journal of Geophysical Research: Biogeosciences*, *117*(1). https://doi.org/10.1029/2011JG001679

Ellwood, M. J., Boyd, P. W., & Sutton, P. (2008). Winter-time dissolved iron and nutrient distributions in the Subantarctic Zone from 40-52S; 155-160E. *Geophysical Research Letters*, *35*(11), 2–7. https://doi.org/10.1029/2008GL033699

Fan, G., Han, Z., Ma, W., Chen, S., Chai, F., Mazloff, M. R., Pan, J., & Zhang, H. (2020). Southern Ocean carbon export efficiency in relation to temperature and primary productivity. *Scientific Reports*, *10*(1), 1–11. https://doi.org/10.1038/s41598-020-70417-z

Fitzsimmons, J. N., & Boyle, E. A. (2014). Both soluble and colloidal iron phases control dissolved iron variability in the tropical north atlantic ocean. *Geochimica et Cosmochimica Acta*, *125*, 539–550. https://doi.org/10.1016/j.gca.2013.10.032

Ito, T., Follows, M. J., & Boyle, E. A. (2004). Is AOU a good measure of respiration in the oceans? *Geophysical Research Letters*, *31*(17), 1–4. https://doi.org/10.1029/2004GL020900

Ito, T., & Follows, M. J. (2005). Preformed phosphate, soft tissue pump and atmospheric CO2. *Journal of Marine Research*, *63*(4), 813–839. https://doi.org/10.1357/0022240054663231

Martin, J. H. (1990). Glacial-Interglacial CO2 change: the iron hypothesis. *Paleoceanography*, *5*(1), 1–13.

Martin, J. H., Fitzwater, S. E., & Gordon, R. M. (1990). Iron deficiency limits phytoplankton growth in Antarctic waters. *Global Biogeochemical Cycles*, *4*(1), 5–12. https://doi.org/10.1029/GB004i001p00005

Mtshali, T. N., van Horsten, N. R., Thomalla, S. J., Ryan-Keogh, T. J., Nicholson, S. A., Roychoudhury, A. N., Bucciarelli, E., Sarthou, G., Tagliabue, A., & Monteiro, P. M. S. (2019). Seasonal Depletion of the Dissolved Iron Reservoirs in the Sub-Antarctic Zone of the Southern Atlantic Ocean. *Geophysical Research Letters*, *46*(8), 4386–4395. https://doi.org/10.1029/2018GL081355

Nishioka, J., Takeda, S., Wong, C. S., & Johnson, W. K. (2001). Size-fractionated iron concentrations in the northeast Pacific Ocean: distribution of soluble and small colloidal iron. *Marine Chemistry*, *74*(2–3), 157–179. https://doi.org/10.1016/S0304-4203(01)00013-5

Parekh, P., Follows, M. J., & Boyle, E. A. (2005). Decoupling of iron and phosphate in the global ocean. *Global Biogeochemical Cycles*, *19*(2), 1–16. https://doi.org/10.1029/2004GB002280

Tagliabue, A., Bowie, A. R., DeVries, T., Ellwood, M. J., Landing, W. M., Milne, A., Ohnemus, D. C., Twining, B. S., & Boyd, P. W. (2019). The interplay between regeneration and scavenging fluxes drives ocean iron cycling. *Nature Communications*, *10*(1), 1–8. https://doi.org/10.1038/s41467-019-12775-5

Tagliabue, A., Mtshali, T., Aumont, O., Bowie, A. R., Klunder, M. B., Roychoudhury, A. N., & Swart, S. (2012). A global compilation of dissolved iron measurements: Focus on distributions and processes in the Southern Ocean. *Biogeosciences*, *9*(6), 2333–2349. https://doi.org/10.5194/bg-9-2333-2012

Tagliabue, A., & Resing, J. (2016). Impact of hydrothermalism on the ocean iron cycle. *Philosophical Transactions of the Royal Society A: Mathematical, Physical and Engineering Sciences*, *374*(2081). https://doi.org/10.1098/rsta.2015.0291

Thuróczy, C. E., Gerringa, L. J. A., Klunder, M. B., Laan, P., & de Baar, H. J. W. (2011). Observation of consistent trends in the organic complexation of dissolved iron in the Atlantic sector of the Southern Ocean. *Deep Sea Research Part II: Topical Studies in Oceanography*, *58*(25–26), 2695–2706. https://doi.org/10.1016/J.DSR2.2011.01.002

Twining, B. S., Nodder, S. D., King, A. L., Hutchins, D. A., LeCleir, G. R., DeBruyn, J. M., Maas, E. W., Vogt, S., Wilhelm, S. W., & Boyd, P. W. (2014). Differential remineralization of major and trace elements in sinking diatoms. *Limnology and Oceanography*, *59*(3), 689–704. https://doi.org/https://doi.org/10.4319/lo.2014.59.3.0689

Wu, J., Boyle, E., Sunda, W., & Wen, L.-S. (2001). Soluble and Colloidal Iron in the Oligotrophic North Atlantic and North Pacific. *Science*, *293*(5531), 847–849. https://doi.org/10.1126/SCIENCE.1059251

Appendix A

This appendix contains supplementary data and figures linked to the interpretation of Chapter 2 of this manuscript; Early winter Southern Indian Ocean dissolved iron distributions and remineralisation (GEOTRACES GIPr07 cruise).

Table A 1: Parameters used to calculate physical supply terms of dFe into the surface mixed layer

Physical dFe supply term			Diapycnal diffusion		Vertical Ekman pumping	Lateral advection		Winter entrainment
Station	Latitude (°S)	Longitude (°E)	Diffusivity constant (k_z) ($m^2\ s^{-1}$)	$\delta dFe/\delta z_{MLD}$ ($\mu mol\ m^{-3}$)	Wind stress curl ($m\ d^{-1}$)	$[dFe]_{MLD}$ ($nmol\ L^{-1}$)	$\delta dFe/\delta x$ ($\mu mol\ m^{-4}$)	Surface current velocity ($m\ s^{-1}$)	$\int[dFe]_{maxMLD}$ ($\mu mol\ m^{-2}$)
TM1	58.5	30	10^{-4}	8.8×10^{-4}	-0.129	0.103	5.4×10^{-8}	-0.016	4.36
TM2	56	30	10^{-4}	1.5×10^{-3}	-0.095	0.114	5.4×10^{-8}	0.006	10.28
TM4	50.5	30	10^{-4}	-4.1×10^{-5}	0.162	0.045	5.4×10^{-8}	0.019	6.48
TM5	48	30	10^{-4}	2.5×10^{-3}	0.267	0.223	5.4×10^{-8}	-0.066	15.10
TM6	45.5	30	10^{-4}	7.1×10^{-4}	0.105	0.277	5.4×10^{-8}	-0.008	21.22
TM7	43	30	10^{-4}	-3.3×10^{-3}	-0.013	0.142	5.4×10^{-8}	-0.012	27.21
TM8	41	30	10^{-4}	9.8×10^{-3}	-0.017	0.382	5.4×10^{-8}	-0.165	73.11

Table A 2: Winter 30°E transect station information; zones Antarctic zone (AZ), Polar Frontal zone (PFZ), Subantarctic zone (SAZ) and the Subtropical zone (STZ), the mixed layer depth (MLD), and the ferricline depths at each station, the apparent oxygen utilisation (AOU) remineralisation depth range used to estimate subsurface remineralisation, the estimated pre-formed PO_4^{3-} concentrations ($[PO_4^{3-}{}_{pre}]$) based on PO_4^{3-} against AOU linear regressions and the integrated subsurface remineralised dFe ($[dFe_{rem}]$)stock, as estimated by AOU.

Station	Date (dd/mm/yr)	Latitude (°S)	Longitude (°E)	Zone	MLD (m)	Ferricline (m)	Remineralisation depth range (m)	$[PO_4^{3-}{}_{pre}]$ ($\mu mol\ L^{-1}$)	$[dFe_{rem}]$ stock ($\mu mol\ m^{-2}$)
TM1	06/07/2017	58.5	30	AZ	156	250	150 - 451	1.77	75.7
TM2	06/07/2017	56	30	AZ	129	150	100 - 501	1.97	52.7
TM4	08/07/2017	50.5	30	AZ	97	300	100 - 501	1.78	138.7
TM5	09/07/2017	48	30	PFZ	126	400	100 - 1252	1.41	564.6
TM6	09/07/2017	45.5	30	SAZ	215	598	100 - 1249	0.62	796.9
TM7	10/07/2017	43	30	SAZ	165	400	175 - 1250	0.33	899.2
TM8	10/07/2017	41	30	STZ	118	100	76 - 1501	0	946.4

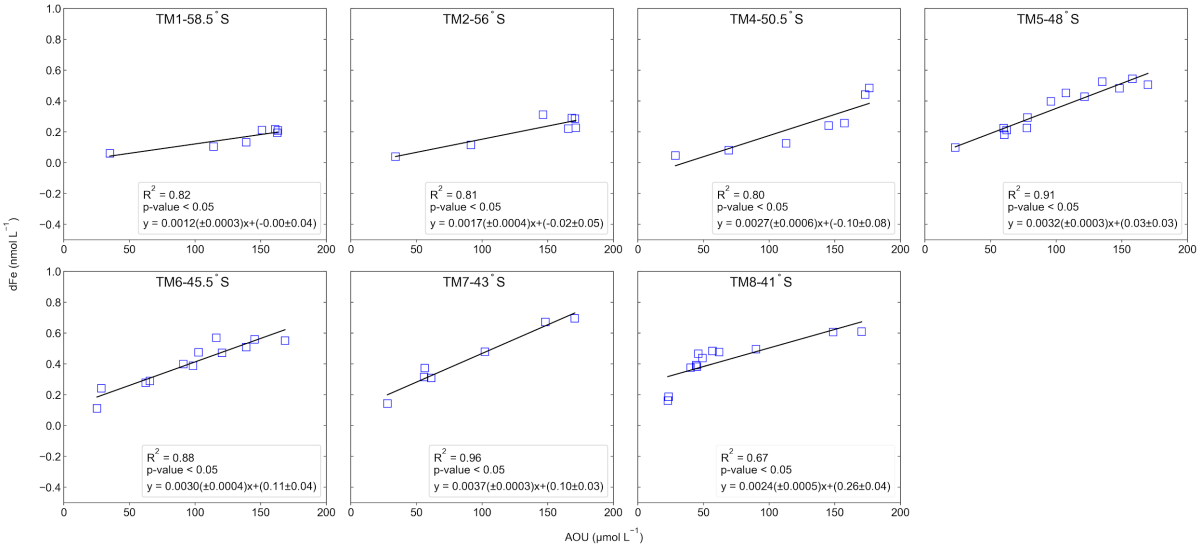

Figure A 1: Least squares linear regression of dFe concentrations within the AOU remineralisation depth range plotted against AOU, for each station along the transect, from TM1 to TM8, from south to north.

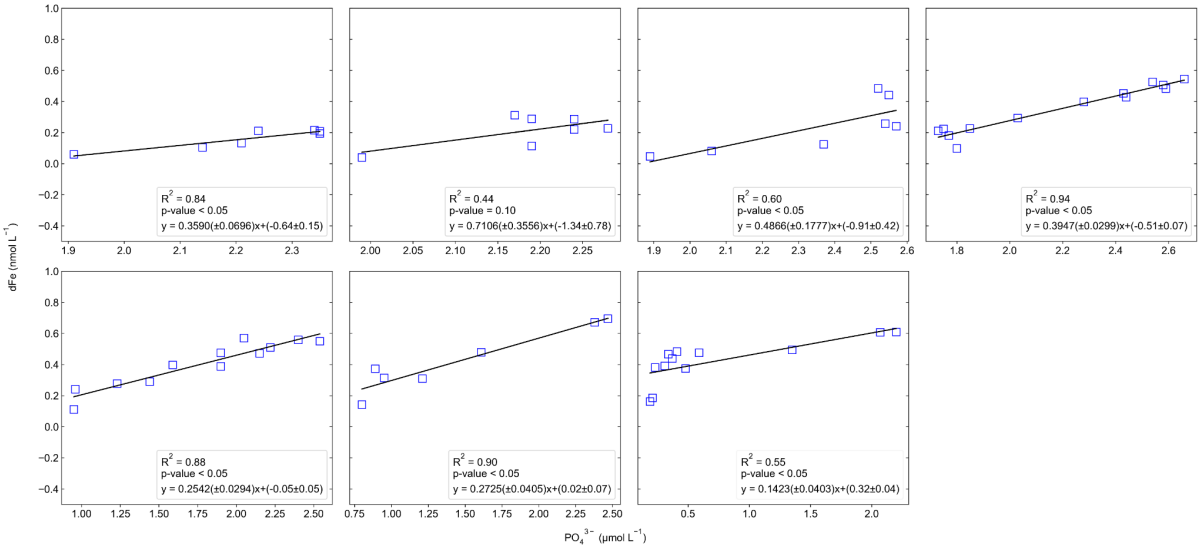

Figure A 2: Least squares linear regression of dFe concentrations within the AOU remineralisation depth range plotted against PO_4^{3-}, for each station along the transect, from TM1 to TM8, from south to north.

Table A 3: Median and standard deviation of dFe (nmol L^{-1}) and macronutrient concentrations (µmol L^{-1}) (Weir et al., 2020) and the number of observations (n), for this study, divided into water masses sampled; namely, Subtropical Surface Water (STSW), South Indian Central Water (SICW), Subantarctic Mode Water (SAMW), Subantarctic Surface Water (SASW), Antarctic Intermediate Water (AAIW), Antarctic Surface Water (AASW), North Atlantic Deep Water (NADW), Lower Circumpolar Deep Water (LCDW), Upper Circumpolar Deep Water (UCDW), Antarctic Bottom Water (AABW).

Nutrient	dFe (nmol L^{-1})			PO_4^{3-} (µmol L^{-1})			NO_3^- (µmol L^{-1})			$Si(OH)_4$ (µmol L^{-1})		
Water mass	Median	SD	n	Median	SD	n	Median	SD	n	Median	SD	n
AASW	0.05	0.04	13	1.91	0.11	13	28.50	1.60	13	44.73	10.05	13
SASW	0.11	0.06	18	0.95	0.41	18	12.15	4.98	18	2.65	1.24	18
STSW	0.14	0.04	4	0.20	0.02	4	2.80	0.41	4	2.91	0.02	4
UCDW	0.24	0.12	23	2.34	0.14	23	35.10	1.32	23	80.19	16.09	23
LCDW	0.38	0.10	15	2.11	0.13	15	33.40	1.12	15	97.99	13.00	15
AAIW	0.44	0.15	26	1.89	0.44	26	27.75	6.24	26	15.99	13.77	26
SAMW	0.48	0.08	3	0.59	0.11	3	7.20	3.09	3	4.82	0.42	3
SICW	0.44	0.05	5	0.34	0.07	5	5.00	0.85	5	3.96	0.30	5
AABW	0.40	0.06	9	2.23	0.08	9	34.20	0.92	9	124.07	9.45	9
NADW	0.55	0.08	15	2.20	0.24	15	33.60	3.07	15	64.66	13.44	15

Table A 4: Statistical data (t-statistic and p-value) for Welch's t-tests conducted on the in situ dFe, PO_4^{3-}, NO_3^- and $Si(OH)_4$ concentration comparisons between water masses sampled. Highlighted comparisons are significantly different, at a 95% confidence level.

	dFe		PO_4^{3-}		NO_3^-		$Si(OH)_4$	
Water mass comparisons	t-statistic	p-value	t-statistic	p-value	t-statistic	p-value	t-statistic	p-value
AASW vs SASW	4.73	6×10^{-5}	8.37	5×10^{-8}	11.31	2×10^{-10}	13.93	7×10^{-9}
SASW vs STSW	0.19	0.85	8.85	8×10^{-8}	9.61	2×10^{-8}	1.11	0.28
AASW vs STSW	3.65	0.01	52.66	1×10^{-16}	52.36	2 x 10-18	14.12	8×10^{-9}
AASW vs UCDW	7.73	1×10^{-8}	9.41	2×10^{-10}	12.50	3×10^{-11}	8.09	2×10^{-9}
UCDW vs LCDW	3.36	0.00	5.38	7×10^{-6}	4.84	3×10^{-5}	4.53	7×10^{-5}
LCDW vs AAIW	1.10	0.25	2.72	0.01	5.21	2×10^{-5}	18.14	6×10^{-18}
AAIW vs SAMW	0.49	0.65	11.74	4×10^{-8}	8.29	0.00	5.85	4×10^{-6}
SAMW vs SICW	0.61	0.59	3.66	0.04	1.90	0.19	3.63	0.03

SASW vs AAIW	8.62	3×10^{-10}	5.97	6×10^{-7}	7.22	8×10^{-9}	6.51	7×10^{-7}
STSW vs SICW	10.31	2×10^{-5}	4.14	0.01	5.35	0.00	8.26	0.00
AABW vs NADW	5.19	4×10^{-5}	0.90	0.38	1.45	0.16	11.76	9×10^{-11}
LCDW vs AABW	1.01	0.33	3.27	0.00	1.66	0.11	4.84	9×10^{-5}
AAIW vs NADW	3.71	7×10^{-4}	4.32	0.00	4.13	0.00	10.30	2×10^{-11}

Table A 5: Median and standard deviation of dFe concentrations (nmol L^{-1}), and the number of observations (n) of the dFe compilation dataset.

All data	**Median (nmol L^{-1})**	**SD (nmol L^{-1})**	**n**
Indian			
SAZ Surface	0.17	0.16	355
SAZ Intermediate	0.29	0.20	190
SAZ Deep	0.51	0.65	62
AZ Surface	0.16	0.22	85
AZ Intermediate	0.29	0.18	64
AZ Deep	0.41	0.69	43
Pacific			
SAZ Surface	0.21	0.15	353
SAZ Intermediate	0.31	0.14	178
SAZ Deep	0.56	0.23	42
AZ Surface	0.21	0.09	37
AZ Intermediate	0.36	0.11	9
AZ Deep	0.38	0.01	2
Atlantic			
SAZ Surface	0.17	0.24	231
SAZ Intermediate	0.41	0.20	147
SAZ Deep	0.58	0.19	217
AZ Surface	0.32	0.67	253
AZ Intermediate	0.38	0.43	109

AZ Deep	0.49	0.38	100
Seasonal data			
Indian Winter			
Surface	0.12	0.11	31
Intermediate	0.43	0.12	37
Deep	0.54	0.10	25
Indian Summer			
Surface	0.18	0.14	14
Intermediate	0.47	0.13	10
Deep	-	-	-
Pacific Winter			
Surface	0.10	0.05	49
Intermediate	0.29	0.13	61
Deep	0.55	0.07	4
Pacific Summer			
Surface	0.39	0.13	90
Intermediate	0.38	0.13	39
Deep	0.60	0.23	21
Atlantic Winter			
Surface	0.25	0.10	6
Intermediate	0.55	0.16	8
Deep	0.79	0.08	7
Atlantic Summer			
Surface	0.17	0.08	37
Intermediate	0.37	0.14	31
Deep	0.63	0.23	31

Table A 6: Statistical data (t-statistic and p-value) for Welch's t-tests conducted on the dFe compilation dataset. Highlighted comparisons are significantly different, at a 95% confidence level.

SO basin comparisons		**t-statistic**	**p-value**
Indian			
SAZ Surface	AZ Surface	0.28	0.78
SAZ Intermediate	AZ Intermediate	0.47	0.64
SAZ Deep	AZ Deep	0.02	0.98
Pacific			
SAZ Surface	AZ Surface	3.88	3×10^{-4}
SAZ Intermediate	AZ Intermediate	0.70	0.50
SAZ Deep	AZ Deep	5.41	3×10^{-6}
Atlantic			
SAZ Surface	AZ Surface	7.38	1×10^{-12}
SAZ Intermediate	AZ Intermediate	1.80	0.07
SAZ Deep	AZ Deep	0.35	0.73
Indian	**Pacific**		
SAZ Surface	SAZ Surface	3.13	2×10^{-3}
SAZ Intermediate	SAZ Intermediate	0.14	0.89
SAZ Deep	SAZ Deep	0.38	0.70
AZ Surface	AZ Surface	0.81	0.42
AZ Intermediate	AZ Intermediate	0.86	0.41
AZ Deep	AZ Deep	2.23	0.03
Pacific	**Atlantic**		
SAZ Surface	SAZ Surface	0.93	0.35
SAZ Intermediate	SAZ Intermediate	6.04	6×10^{-9}
SAZ Deep	SAZ Deep	0.76	0.45
AZ Surface	AZ Surface	8.54	8×10^{-16}
AZ Intermediate	AZ Intermediate	4.03	3×10^{-4}
AZ Deep	AZ Deep	5.51	3×10^{-7}

Atlantic	**Indian**		
SAZ Surface	SAZ Surface	1.10	0.27
SAZ Intermediate	SAZ Intermediate	5.40	1×10^{-7}
SAZ Deep	SAZ Deep	0.06	0.95
AZ Surface	AZ Surface	7.38	1×10^{-12}
AZ Intermediate	AZ Intermediate	3.97	1×10^{-4}
AZ Deep	AZ Deep	0.20	0.84
Winter study comparisons			
Indian	**Pacific**		
SAZ Surface	SAZ Surface	2.44	0.02
SAZ Intermediate	SAZ Intermediate	4.30	5×10^{-5}
SAZ Deep	SAZ Deep	0.04	0.97
Pacific	**Atlantic**		
SAZ Surface	SAZ Surface	3.57	0.01
SAZ Intermediate	SAZ Intermediate	3.96	3×10^{-3}
SAZ Deep	SAZ Deep	5.59	6×10^{-4}
Atlantic	**Indian**		
SAZ Surface	SAZ Surface	2.02	0.08
SAZ Intermediate	SAZ Intermediate	1.96	0.08
SAZ Deep	SAZ Deep	6.84	2×10^{-5}
Seasonal comparisons			
Indian			
Winter Surface	Summer Surface	1.12	0.28
Winter Intermediate	Summer Intermediate	0.67	0.52
Winter Deep	Summer Deep	-	-
Pacific			
Winter Surface	Summer Surface	17.49	5×10^{-36}
Winter Intermediate	Summer Intermediate	4.85	6×10^{-6}

Winter Deep	Summer Deep	1.06	0.30
Atlantic			
Winter Surface	Summer Surface	1.77	0.13
Winter Intermediate	Summer Intermediate	1.95	0.08
Winter Deep	Summer Deep	3.45	2×10^{-3}

Appendix B

This appendix contains supplementary data and figures, as submitted with the Early winter barium excess in the Southern Indian Ocean as an annual remineralisation proxy (GEOTRACES GIPr07 cruise) paper, presented as Chapter 3 of this manuscript.

Table B 1: Winter 30°E transect station information; regions - north of the Polar Front (NPF), south of the Polar Front (SPF) and the subtropical zone (STZ), mixed layer depth (MLD) and mesopelagic depth-weighted average Ba_{xs} concentrations.

Station	Date (dd/mm/yr)	Latitude (°S)	Longitude (°E)	Zone	MLD (m)	Ba_{xs} (pmol L^{-1})
TM1	06/07/2017	58.5	30	SPF	156	249
TM2	06/07/2017	56	30	SPF	129	273
TM4	08/07/2017	50.5	30	SPF	97	346
TM5	09/07/2017	48	30	NPF	126	375
TM6	09/07/2017	45.5	30	NPF	215	329
TM7	10/07/2017	43	30	NPF	165	383
TM8	10/07/2017	41	30	STZ	118	192

Table B 2: Particulate Ba (pBa), particulate Al (pAl) and barium excess (Ba_{xs}) profile concentrations for seven stations along the 30°E transect study during winter 2017.

Station Latitude (°S), Longitude (°E)	Depth (m)	pBa (pmol L^{-1})	pAl (nmol L^{-1})	Ba_{xs} (pmol L^{-1})
TM1 58.5°S, 30°E	25	134	0.76	133
	75	131	1.09	130
	100	193	0.77	192
	150	153	1.18	151
	200	340	0.58	339
	250	357	1.25	355
	299	375	0.29	375
	349	343	0.78	342
	401	352	0.84	351
	451	271	0.36	271
	500	229	0.33	229
	550	150	1.98	147
	751	256	1.63	254
	1001	203	1.20	201
	1250	245	1.45	243
	1500	207	1.47	205
TM2 56°S, 30°E	25	127	0.72	126
	51	121	1.30	119
	76	113	0.74	112
	100	113	0.31	113
	150	271	0.57	270
	201	248	0.25	248
	250	311	0.69	310
	300	453	0.82	452
	401	356	1.11	355
	501	315	0.75	314
	599	253	0.74	252
	701	228	0.48	227
	801	224	0.98	223
	901	235	1.17	233
	1001	228	1.46	226
	1250	235	1.33	233
	1751	206	1.68	204
	2250	192	1.94	189
	2769	163	2.03	160

	3500	194	2.83	190
TM4 50.5°S, 30°E	26	121	0.67	120
	75	132	0.79	131
	99	154	1.39	152
	151	536	0.28	536
	200	634	0.67	633
	250	560	0.92	559
	300	607	0.97	606
	399	155	0.66	154
	501	399	1.20	397
	602	289	0.64	288
	701	271	0.93	270
	799	281	0.68	280
	901	245	1.29	243
	999	361	2.92	357
	1250	225	2.18	222
	2000	164	1.37	162
	2502	183	2.52	180
	3001	163	3.41	158
	3501	249	6.24	241
TM5 48°S, 30°E	26	143	0.88	142
	50	135	1.63	133
	75	113	0.86	112
	100	127	0.39	126
	150	627	1.46	625
	201	349	0.58	348
	251	686	1.29	684
	301	561	1.61	559
	400	510	1.15	508
	501	368	1.89	365
	601	318	1.72	316
	700	185	0.95	184
	802	320	1.67	318
	900	305	1.54	303
	1000	342	2.12	339
	1752	308	2.44	305
	2250	187	2.09	184
	2751	186	2.03	183
	3501	136	2.03	133
	4251	92	2.97	88
TM6 45.5°S, 30°E	23	89	0.66	88
	76	83	0.64	82
	101	92	0.72	91
	149	115	1.28	113
	200	128	1.01	127
	251	639	2.99	635
	300	285	1.24	283
	400	439	3.48	434
	598	404	3.74	399
	701	299	3.50	294
	800	319	3.11	315
	902	323	4.01	318
	1000	348	2.76	344
	1249	218	1.86	215
	1750	257	2.32	254
	2249	188	2.50	185
	2750	180	3.68	175
	3500	116	2.27	113
	4249	82	2.98	78

TM7 43°S, 30°E	26	102	0.99	101
	75	109	1.13	107
	101	128	1.47	126
	126	114	1.13	112
	150	129	1.13	127
	175	158	1.16	156
	202	619	2.01	616
	253	559	1.85	557
	301	570	1.70	568
	400	364	2.23	361
	500	480	2.59	477
	750	380	2.29	377
	1008	272	2.74	268
	1250	260	4.74	254
	1503	280	3.35	275
TM8 41°S, 30°E	25	61	1.53	59
	76	74	1.98	71
	100	76	2.55	73
	120	159	1.24	157
	151	211	2.15	208
	175	169	2.50	166
	200	207	2.36	204
	251	238	3.47	233
	299	158	3.53	153
	401	128	3.47	123
	501	168	3.82	163
	801	253	5.37	246
	1000	248	5.22	241
	1249	240	5.31	233
	1501	178	4.23	172

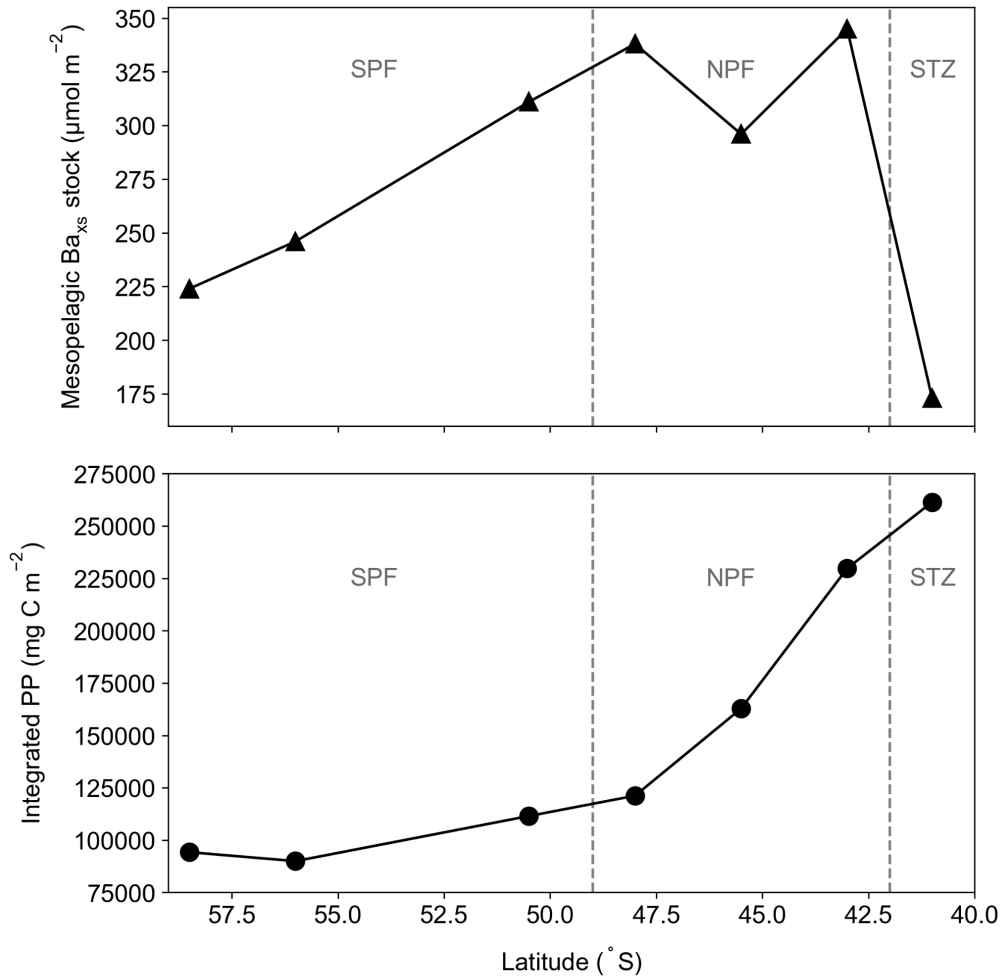

Figure B 1: Top panel is the latitudinal trend, south to north, left to right, of winter integrated mesopelagic Baxs stock concentrations (black triangles). The bottom panel is the latitudinal trend of the corresponding annually integrated remote sensing PP (black circles). Sampling regions are overlaid in grey, namely SPF, NPF and STZ.

Table B 3: Barium excess data used for the Southern Ocean (SO) compilation dataset, split into regions sampled during each study (south of the Polar Front (SPF), north of the Polar Front (NPF) and the subtropical zone (STZ)), the SO basin sampled, estimated POC remineralisation fluxes (POC_{rem}) using the Ba_{xs} method, integrated POC_{rem} is the POC flux multiplied by number of days from preceding September up to 1 month prior to sampling, $PP_{integrated}$ is the integrated remotely sensed PP multiplied by the number of days used for integrated POC_{rem} and % integrated POC_{rem} is the percentage integrated POC_{rem} to $PP_{integrated}$. No remotely sensed PP was available for studies preceding September 1997. *Particulate sample digestion methods did not use HF and thus may overestimate Ba_{xs} concentrations.

Basin	Zone	Date	Latitude (°S)	Longitude (°E)	Ba_{stock} (µmol m^{-2})	POC_{rem} (mg C m^{-2} d^{-1})	Integrated POC_{rem} (mg C m^{-2})	$PP_{integrated}$ (mg C m^{-2})	% Integrated POC_{rem}	Reference
Indian (20°E - 145°E)	SPF	06/07/2017	58.5	30.0	224	32	8896	94226	9	This study
	SPF	06/07/2017	56.0	30.0	246	44	12232	89959	14	
	SPF	08/07/2017	50.5	30.0	311	78	21840	111498	20	
	NPF	09/07/2017	48.0	30.0	338	92	25852	121189	21	
	NPF	09/07/2017	45.5	30.0	296	70	19670	162823	12	
	NPF	10/07/2017	43.0	30.0	345	96	27072	229782	12	
	STZ	10/07/2017	41.0	30.0	173	6	1692	261424	1	
	SPF	01/11/2011	48.5	72.1	77	42	1302	3246	40	Jacquet et al. (2015)
	SPF	04/11/2011	48.7	72.0	72	35	1190	3505	34	
	SPF	12/11/2011	48.8	71.4	103	76	3192	4189	76	
	SPF	14/11/2011	48.7	72.6	89	58	2552	4693	54	
	SPF	16/11/2011	50.6	72.1	67	11	506	2957	17	
	SPF	18/11/2011	48.4	71.9	95	66	3168	6557	48	
	NPF	02/11/2011	48.4	75.0	60	20	640	3016	21	
	NPF	07/11/2011	48.5	74.7	82	49	1813	3387	54	

	SPF	20/01/2005	49.2	74.0	127	32	3552	20593	17	
	SPF	24/01/2005	50.6	72.1	130	34	3910	15787	25	
	SPF	26/01/2005	51.7	78.0	100	21	2457	18911	13	
	SPF	29/01/2005	50.5	77.0	154	45	5400	20634	26	
	SPF	30/01/2005	51.1	74.6	131	34	4114	13586	30	Jacquet et al. (2008a)
	SPF	03/02/2005	50.6	72.1	120	29	3625	20508	18	
	SPF	06/02/2005	51.7	78.0	160	48	6144	23831	26	
	SPF	07/02/2005	52.4	75.6	145	41	5289	21603	25	
	SPF	12/02/2005	50.6	72.1	111	25	3350	26108	13	
	SPF	13/11/2001	53.7	142.0	88	15	645	6486	10	
	SPF	16/11/2001	56.9	142.0	121	29	1334	6259	21	
	SPF	20/11/2001	60.9	142.0	86	14	700	10680	7	
	SPF	24/11/2001	63.9	142.0	79	12	648	10144	6	
	SPF	05/12/2001	63.9	142.0	92	17	1105	15831	7	Cardinal et al. (2005)
	SPF	07/12/2001	60.9	142.0	139	36	2412	18509	13	
	NPF	03/11/2001	46.9	142.0	74	10	330	-	-	
	NPF	07/11/2001	48.9	142.0	68	7	259	-	-	
	NPF	09/11/2001	51.0	142.0	62	5	195	1621	12	
	NPF	10/12/2001	51.0	142.0	59	4	280	10929	3	

	NPF	19/01/1999	46.0	62.5	283	102	11220	80171	14	
	NPF	25/01/1999	45.1	63.1	239	63	7308	86214	9	
	NPF	28/01/1999	44.5	62.5	343	118	14042	87265	16	
	STZ	31/01/1999	44.3	62.4	234	65	7930	92009	9	Jacquet et al. (2005)
	STZ	02/02/1999	44.2	62.3	283	82	10168	93316	11	
	STZ	07/02/1999	44.0	63.4	292	86	11094	90692	12	
	STZ	13/02/1999	43.1	62.5	151	32	4320	100687	4	
	SPF	19/03/1998	53.7	141.8	153	41	6929	82220	8	
	SPF	22/03/1998	53.0	141.7	145	35	6020	81306	7	
	NPF	07/03/1998	45.0	141.5	82	14	2198	100516	2	
	NPF	10/03/1998	46.8	142.0	57	2	320	100374	0	Cardinal et al. (2001)
	NPF	15/03/1998	49.5	141.8	96	20	3300	96739	3	
	NPF	17/03/1998	51.0	141.8	127	30	5010	92570	5	
	NPF	26/03/1998	50.9	142.8	94	17	2992	103327	3	
	STZ	03/03/1998	42.0	141.9	87	15	2295	94660	2	
	SPF	14/01/1987	56.5	63.2	345	93	12491			
	SPF	16/01/1987	59.5	69.9	259	55	7587			Dehairs et al. (1990)*
	SPF	17/01/1987	61.8	76.3	274	66	9082			
	SPF	18/01/1987	64.2	84.0	194	21	2964			

	SPF	20/01/1987	66.0	67.3	189	14	1952			
	SPF	24/01/1987	63.8	42.0	261	50	7301			
	SPF	26/01/1987	65.2	32.0	166	2	305			
	SPF	27/01/1987	61.0	32.3	273	58	8569			
	SPF	28/01/1987	57.0	31.8	268	54	7996			
	SPF	29/01/1987	53.0	31.2	239	39	5817			
	NPF	01/02/1987	47.2	23.6	176	7	1108			
	STZ	05/02/1987	38.0	23.3	161	-	-			
	STZ	07/02/1987	38.0	30.0	116	-	-			
Indian (20°E - 145°E) & Pacific (145°E - 65°W)	SPF	01/02/2007	54.0	145.9	177	43	5314	61097	9	Jacquet et al. (2011)
	SPF	02/02/2007	54.0	146.1	167	38	4762	61864	8	
	SPF	03/02/2007	54.1	146.3	220	65	8100	62461	13	
	SPF	04/02/2007	54.5	146.1	258	84	10584	62828	17	
	SPF	05/02/2007	54.5	147.1	232	71	8992	61876	15	
	SPF	07/02/2007	50.9	148.7	140	44	5676	50368	11	
	NPF	20/01/2007	44.9	143.1	125	37	4107	60591	7	
	NPF	22/01/2007	46.3	140.6	94	22	2441	53982	5	
	NPF	26/01/2007	46.5	140.3	112	33	3875	57207	7	
	NPF	28/01/2007	46.6	140.6	94	22	2570	59415	4	

	NPF	08/02/2007	50.0	149.4	153	52	6760	52597	13	
	NPF	09/02/2007	48.1	151.2	198	73	9563	61995	15	
	NPF	11/02/2007	45.6	153.2	141	46	6065	86173	7	
	NPF	12/02/2007	45.5	153.4	148	49	6593	90826	7	
	NPF	14/02/2007	44.9	152.5	122	36	4896	97168	5	
	NPF	16/02/2007	45.6	153.7	130	40	5465	93136	6	
	STZ	19/02/2007	43.7	148.6	73	12	1692	114832	1	
Atlantic (65°W - 20°E)	SPF	11/03/2008	51.9	0.0	112	13	2155	66711	3	Planchon et al. (2013)
	SPF	14/03/2008	55.2	0.0	132	23	3861	67327	6	
	NPF	27/02/2008	42.5	8.9	135	25	3740	114462	3	
	NPF	01/03/2008	44.9	6.9	236	77	11658	85271	14	
	NPF	05/03/2008	47.5	4.4	145	30	4680	75250	6	
	NPF	07/03/2008	49.0	2.8	184	50	7900	66889	12	
	SPF	11/02/2004	50.0	2.0	324	78	10374	50310	21	Jacquet et al. (2008b)
	SPF	22/02/2004	50.0	2.0	232	31	4464	59284	8	
	SPF	23/02/2004	50.0	2.0	198	14	2030	60100	3	
	SPF	04/03/2004	50.0	2.0	275	40	6200	69011	9	
	SPF	09/03/2004	50.0	2.0	260	45	7200	71992	10	
	SPF	11/03/2004	50.0	2.0	353	92	14904	73184	20	

	SPF	17/03/2004	50.0	2.0	360	96	16128	76760	21	
	SPF	19/03/2004	50.0	2.0	292	61	10370	77953	13	
	SPF	13/10/1992	56.5	-6.0	65	13	528			
	SPF	14/10/1992	54.5	-6.0	54	7	293			
	SPF	22/10/1992	56.1	-6.8	59	9	480			
	SPF	25/10/1992	55.0	-6.0	69	14	779			
	SPF	26/10/1992	53.0	-6.0	60	10	549			
	SPF	27/10/1992	51.0	-6.0	73	16	923			
	SPF	29/10/1992	49.0	-6.0	76	18	1052			
	SPF	06/11/1992	59.5	-6.0	77	19	1226			
	SPF	12/11/1992	57.5	-6.0	59	9	681			Dehairs et al. (1997)*
	SPF	12/11/1992	57.5	-6.0	69	14	1023			
	SPF	16/11/1992	53.0	-6.0	63	12	878			
	SPF	17/11/1992	51.0	-6.0	76	25	1920			
	SPF	19/11/1992	49.0	-6.0	94	27	2152			
	SPF	23/11/1992	49.8	-6.0	77	19	1548			
	NPF	18/10/1992	48.5	-6.0	101	31	1436			
	NPF	30/10/1992	47.0	-6.0	77	18	1079			
	NPF	21/11/1992	47.0	-6.0	86	23	1876			

	NPF	22/11/1992	48.5	-6.0	86	23	1891	
	SPF	26/11/1988	57.0	-49.0	180	9	775	
	SPF	27/11/1988	58.0	-48.9	47	-	-	
	SPF	28/11/1988	59.0	-49.0	52	-	-	
	SPF	28/11/1988	60.0	-49.0	49	-	-	
	SPF	29/11/1988	61.0	-49.1	51	-	-	
	SPF	30/11/1988	62.0	-49.0	48	-	-	
	SPF	02/12/1988	61.0	-49.0	127	-	-	
	SPF	05/12/1988	59.0	-49.0	73	-	-	
	SPF	08/12/1988	59.4	-48.7	21	-	-	Dehairs et al. (1991)*
	SPF	09/12/1988	59.4	-48.7	24	-	-	
	SPF	10/12/1988	57.0	-49.0	133	-	-	
	SPF	11/12/1988	57.0	-48.7	71	9	870	
	SPF	13/12/1988	57.0	-47.0	127	28	2890	
	SPF	13/12/1988	58.0	-47.0	74	1	117	
	SPF	14/12/1988	59.0	-47.0	42	-	-	
	SPF	15/12/1988	60.0	-47.0	54	-	-	
	SPF	16/12/1988	61.0	-47.0	69	-	-	
	SPF	16/12/1988	61.5	-47.0	31	-	-	

	SPF	19/12/1988	60.9	-45.4	17	0.2	25
	SPF	20/12/1988	50.0	-49.0	20	-	-
	SPF	20/12/1988	59.5	-49.0	14	-	-
	SPF	21/12/1988	60.0	-49.0	16	-	-
	SPF	21/12/1988	60.5	-49.0	17	-	-
	SPF	22/12/1988	61.0	-49.0	21	-	-
	SPF	22/12/1988	61.5	-49.0	22	-	-
	SPF	24/12/1988	62.1	-49.0	40	-	-
	SPF	27/12/1988	57.0	-48.9	106	20	2331
	SPF	28/12/1988	58.0	-49.0	73	3	390
	SPF	28/12/1988	59.0	-49.0	61	-	-
	SPF	29/12/1988	60.0	-49.0	32	-	-
	SPF	30/12/1988	61.0	-49.0	38	-	-
	SPF	31/12/1988	61.7	-48.8	19	-	-

Table B 4: Least squares regression statistics for correlations between mesopelagic Ba_{xs} stock and temporally integrated remotely sensed PP of the SO compilation data for all tested timescales between the preceding September and 1 month prior to sampling (Sept - T1) where the T-value is the number of months prior to sampling. Sept - T1 regressions considered integrated PP from Sept 2016 to June 2017 and T1 - T2 considered PP from May 2017 to June 2017, for this study (July 2017). For a study conducted in March 1998, Sept - T1 considered PP from September 1997 to February 1998 and T1 - T2 considered PP from January 1998 to February 1998. Highlighted comparisons are significantly different, at a 95% confidence level.

Zones	SPF			NPF			STZ		
Time scales	R^2	p-value	n	R^2	p-value	n	R^2	p-value	n
Sept - T1	0.55	6×10^{-8}	39	0.42	9×10^{-5}	31	0.53	0.10	6
Sept - T2	0.30	2×10^{-3}	29	0.34	2×10^{-3}	26	0.93	2×10^{-3}	6
Sept - T3	0.19	0.02	30	0.37	1×10^{-3}	25	0.37	0.20	6
Sept - T4	0.09	0.13	26	0.67	3×10^{-5}	18	0.12	0.57	5
T1-T2	0.51	2×10^{-7}	40	0.01	0.60	30	0.06	0.63	6
T1-T3	0.33	8×10^{-4}	30	0.11	0.11	25	0.16	0.43	6
T1-T4	0.31	2×10^{-3}	28	0.16	0.05	24	0.45	0.14	6
T2-T3	0.29	2×10^{-3}	30	0.15	0.05	26	0.57	0.08	6
T2-T4	0.25	6×10^{-3}	28	0.10	0.13	25	0.76	0.02	6
T3-T4	0.14	0.04	30	0.00	0.77	25	0.56	0.09	6

Appendix C

This appendix contains ancillary and metadata for stations sampled along the 30°E line during the GEOTRACES GIpr07 cruise. This data was used for the interpretation of dFe and Ba_{xs} measurements conducted during this study.

Table C1: Metadata, ancillary data and nutrient concentrations (Weir et al., 2020) of samples collected along the 30°E line, during the GEOTRACES GIpr07 process study, from 58.5°S to 41°S (TM1 to TM8).

Station	Date (dd/mm/yr)	Latitude (°S)	Depth (m)	Salinity	Temperature (°C)	Dissolved O_2 (ml/L)	dFe (nmol/L)	$Si(OH)_4$ (µmol/L)	NO_3^- (µmol/L)	PO_4^{3-} (µmol/L)	Chl α (µg/L)
TM1	06/07/2017	58.5	25	34.00	-0.06	7.44	0.05	46.79	28.60	1.78	0.19
			52	34.00	-0.06	7.42	0.02	45.62	28.50	1.76	0.20
			75	34.00	-0.06	7.41	0.04	44.73	28.70	1.80	0.23
			100	34.00	-0.06	7.40	0.02	53.35	28.00	2.00	0.23
			150	34.01	-0.03	7.32	0.06	49.63	28.20	1.91	0.18
			200	34.41	0.63	5.39	0.10	77.55	34.50	2.14	0.00
			250	34.49	0.76	4.80	0.13	84.75	35.20	2.21	0.01
			299	34.55	1.00	4.48	0.21	86.42	35.20	2.24	0.00
			349	34.61	1.30	4.19	0.22	91.97	35.10	2.34	0.00
			401	34.64	1.35	4.14	0.19	96.24	35.00	2.35	0.00
			451	34.66	1.36	4.13	0.21	97.45	34.70	2.35	0.00
			500	34.67	1.32	4.15	0.18	98.61	34.60	2.34	0.00
			550	34.70	1.46	4.16	0.17	99.14	34.20	2.26	0.00
			650	34.71	1.37	4.23	0.34	101.33	33.60	2.20	0.00
			751	34.70	1.10	4.28	0.36	105.06	33.80	2.21	0.00
			1001	34.70	0.91	4.40	0.34	111.84	34.10	2.11	-0.01
			1250	34.69	0.66	4.42	0.48	114.82	34.10	2.14	0.00
			1500	34.69	0.54	4.44	0.41	122.50	34.60	2.24	-0.01
TM2	06/07/2017	56	25	33.97	0.50	7.26	0.05	42.91	28.70	1.93	0.23
			51	33.97	0.50	7.26	0.17	42.43	28.80	1.97	0.23
			76	33.97	0.51	7.25	0.04	43.24	28.50	2.01	0.23
			100	33.97	0.51	7.23	0.04	45.57	28.90	1.99	0.23
			150	34.17	0.87	5.86	0.11	56.73	32.90	2.19	0.05
			201	34.38	1.44	4.50	0.31	69.74	35.70	2.17	0.01
			250	34.48	1.80	3.93	0.29	73.71	36.00	2.19	0.00
			300	34.51	1.70	4.01	0.22	78.68	36.40	2.24	0.01
			401	34.58	1.69	3.88	0.23	83.56	35.80	2.28	0.01
			501	34.65	1.80	3.87	0.29	88.71	35.10	2.24	0.00
			599	34.69	1.87	3.90	0.29	89.39	34.10	2.24	0.00
			701	34.70	1.69	4.01	0.31	91.83	33.50	2.14	0.00
			801	34.74	1.89	4.17	0.35	91.18	33.10	2.03	0.00
			901	34.74	1.77	4.24	0.63	89.90	32.50	1.80	0.00
			1001	34.74	1.62	4.28	0.40	90.04	32.10	1.97	0.00
			1250	34.74	1.40	4.37	0.41	97.99	32.20	2.00	0.00
			1751	34.71	0.87	4.42	0.37	114.90	33.40	1.99	0.00
			2250	34.69	0.52	4.46	0.37	124.07	34.50	2.11	0.00
			2769	34.68	0.30	4.57	0.40	129.32	34.60	2.21	0.00
			3500	34.67	0.05	4.78	0.47	129.21	34.60	2.17	0.00
TM4	08/07/2017	50.5	26	33.77	1.79	7.16	0.03	25.11	26.40	1.91	0.34
			50	33.77	1.79	7.17	0.05	26.94	26.60	1.87	0.33
			99	33.78	1.74	7.11	0.05	26.56	26.80	1.89	0.28
			151	34.02	1.43	6.25	0.08	32.84	31.30	2.06	0.01
			200	34.17	1.65	5.22	0.12	45.20	34.60	2.37	0.00
			250	34.33	2.03	4.41	0.24	55.86	36.60	2.57	-0.01
			300	34.39	2.08	4.13	0.26	63.80	37.40	2.54	0.01
			399	34.51	2.23	3.74	0.44	71.58	36.60	2.55	0.00

			501	34.59	2.26	3.66	0.48	75.30	35.30	2.52	0.00
			602	34.65	2.27	3.72	0.43	79.12	34.90	2.47	0.00
			701	34.68	2.22	3.79	0.40	81.95	34.20	2.45	0.00
			799	34.70	2.17	3.84	0.49	81.07	33.50	2.43	0.00
			901	34.72	2.12	3.97	0.40	80.19	32.70	2.33	0.00
			999	34.75	2.14	4.14	0.38	79.07	31.50	2.21	0.00
			1250	34.77	2.03	4.34	0.46	78.35	30.70	1.94	0.00
			1750	34.74	1.38	4.38	0.49	97.72	32.20	2.11	0.00
			2502	34.71	0.77	4.45	0.38	117.35	33.40	2.27	0.00
			3001	34.69	0.50	4.52	0.37	126.77	34.20	2.23	-0.01
			3501	34.67	0.08	4.79	0.40	132.22	34.20	2.17	-0.01
			26	33.81	5.10	6.63	0.10	5.22	22.80	1.74	0.49
			50	33.81	5.09	6.61	0.09	5.28	22.90	1.77	0.50
			75	33.81	5.09	6.62	0.10	5.32	23.10	1.75	0.49
			100	33.81	5.10	6.61	0.10	5.31	23.10	1.80	0.45
			150	34.28	6.74	5.49	0.22	9.17	23.50	1.75	-0.01
			201	34.26	6.24	5.52	0.21	10.12	24.40	1.73	-0.01
			251	34.23	5.64	5.66	0.18	10.32	25.50	1.77	-0.01
			301	34.23	5.33	5.33	0.23	13.42	27.60	1.85	0.00
			400	34.16	4.31	5.50	0.29	15.98	29.00	2.03	-0.01
			501	34.22	4.18	5.12	0.40	22.89	31.00	2.28	-0.01
TM5	09/07/2017	48	601	34.23	3.64	4.96	0.45	29.70	32.30	2.43	0.00
			700	34.26	3.27	4.71	0.43	35.96	33.80	2.44	0.00
			802	34.31	3.13	4.43	0.53	42.22	34.60	2.54	0.00
			900	34.37	3.04	4.15	0.48	49.26	35.30	2.59	0.00
			1000	34.42	2.93	3.95	0.54	54.95	35.90	2.66	0.00
			1252	34.53	2.71	3.72	0.51	64.12	35.80	2.58	0.01
			1752	34.73	2.61	4.00	0.63	67.27	32.10	2.12	0.00
			2249	34.78	2.31	4.28	0.65	71.93	30.20	2.02	0.00
			2751	34.78	1.89	4.37	0.60	80.79	30.60	2.11	0.00
			3501	34.73	1.16	4.39	0.51	103.18	32.50	2.30	0.00
			4251	34.70	0.73	4.50	0.41	113.04	33.60	2.25	0.00
			23	34.44	9.56	5.87	0.12	3.44	12.20	1.02	0.39
			49	34.45	9.58	5.86	0.13	2.51	12.40	1.02	0.36
			76	34.44	9.55	5.86	0.13	3.24	12.40	0.95	0.40
			101	34.46	9.64	5.84	0.28	2.70	12.10	0.95	0.38
			149	34.48	9.73	5.81	0.11	2.59	12.10	0.95	0.34
			200	34.70	10.58	5.61	0.24	2.79	13.10	0.96	0.16
			251	34.70	9.95	4.94	0.28	4.02	15.00	1.23	-0.01
			300	34.55	8.79	5.04	0.29	6.65	17.40	1.44	-0.01
			400	34.52	7.92	4.60	0.40	11.57	21.50	1.59	0.00
			500	34.36	6.10	4.73	0.39	16.00	25.90	1.90	0.00
TM6	09/07/2017	45.5	598	34.31	5.25	4.78	0.48	19.28	27.90	1.90	-0.01
			701	34.32	4.59	4.59	0.57	27.00	29.40	2.05	-0.01
			800	34.29	3.93	4.61	0.47	32.05	30.80	2.15	0.00
			902	34.36	3.74	4.23	0.51	40.73	32.00	2.22	0.00
			1000	34.37	3.28	4.17	0.56	47.39	32.90	2.40	0.00
			1249	34.51	2.93	3.71	0.55	64.62	33.60	2.54	0.01
			1750	34.70	2.66	3.90	0.52	69.47	31.00	2.19	0.01
			2249	34.80	2.46	4.41	0.53	64.66	27.10	2.01	0.00
			2750	34.82	2.21	4.57	0.55	68.44	26.80	1.98	0.00
			3500	34.75	1.40	4.40	0.45	101.65	30.00	2.19	0.00
			4249	34.71	0.81	4.45	0.52	116.94	32.10	2.40	0.00
			26	34.58	10.55	5.78	0.11	1.65	8.40	0.63	0.51
			50	34.58	10.55	5.78	0.11	2.25	10.10	0.63	0.52
			75	34.58	10.55	5.77	0.15	2.27	10.80	0.70	0.51
TM7	10/07/2017	43	101	34.60	10.60	5.75	0.11	2.27	11.40	0.70	0.49
			126	34.66	10.79	5.70	0.10	2.39	11.30	0.81	0.38
			150	34.69	10.88	5.65	0.22	2.45	11.40	0.79	0.32
			175	34.65	10.64	5.62	0.14	2.57	11.80	0.80	0.18

			202	34.75	10.63	4.98	0.37	2.89	11.80	0.89	0.01
			253	34.71	10.06	5.07	0.31	4.59	13.50	0.95	0.00
			301	34.61	9.32	5.06	0.31	6.08	18.60	1.21	0.00
			400	34.58	8.53	4.57	0.67	10.10	22.60	1.45	-0.01
			500	34.47	7.11	4.48	0.48	14.96	27.00	1.61	-0.01
			750	34.25	4.36	4.93	0.68	24.48	31.00	2.11	-0.01
			1008	34.40	3.63	4.04	0.67	46.89	34.70	2.38	0.00
			1250	34.54	3.26	3.60	0.70	63.49	35.30	2.47	0.01
			1503	34.62	2.86	3.69	0.73	66.09	34.50	2.24	0.00
TM8	10/07/2017	41	25	35.59	18.02	4.84	0.10	2.92	2.40	0.22	0.33
			51	35.59	18.03	4.83	0.11	2.90	2.50	0.19	0.36
			76	35.59	18.03	4.83	0.16	2.90	3.20	0.19	0.37
			100	35.58	18.00	4.82	0.19	2.94	3.10	0.21	0.32
			120	35.56	17.50	4.39	0.38	3.76	4.30	0.23	0.01
			151	35.55	17.24	4.43	0.39	3.87	4.30	0.31	0.03
			175	35.53	16.99	4.42	0.47	3.96	5.00	0.34	0.02
			200	35.52	16.71	4.38	0.44	4.03	5.70	0.37	0.02
			251	35.50	16.14	4.27	0.48	4.54	6.20	0.41	0.01
			299	35.32	14.89	4.79	0.38	4.78	6.40	0.48	0.03
			401	35.29	13.73	4.44	0.48	4.82	7.20	0.59	0.00
			501	35.12	12.42	4.56	0.54	5.53	12.10	0.70	0.00
			801	34.56	8.15	4.59	0.49	11.96	21.20	1.35	0.00
			1000	34.39	5.56	4.38	0.68	27.49	29.80	1.88	0.00
			1249	34.43	4.22	3.92	0.61	46.23	33.40	2.07	0.01
			1501	34.54	3.49	3.56	0.61	64.21	34.80	2.20	0.01

Titre : Distributions en fer dissous et en baryum particulaire pour l'étude de la reminéralisation en début d'hiver dans le secteur Indien de l'Océan Austral (mission GEOTRACES GIPr07)

Mots clés : L'Océan Austral, excès de baryum en hiver, cyclage du fer en hiver, reminéralisation

Résumé : L'océan Austral est d'une importance centrale pour l'océan mondial, reliant les bassins Atlantique, Pacifique et Indien grâce notamment au courant circumpolaire antarctique, qui transporte de grandes quantités de chaleur, de carbone et de nutriments. Ainsi, cette province océanique régule en partie le climat de la Terre. Un des facteurs influençant la pompe à carbone biologique de l'Océan Austral est la disponibilité en fer, qui est un nutriment essentiel à la cellule phytoplanctonique. Or, les observations dans cette région ont été principalement menées au printemps et en été, laissant des lacunes importantes dans notre connaissance du cycle biogéochimique du fer notamment sur la saisonnalité des processus internes tels que la reminéralisation mésopélagique.
Au cours de cette thèse, les distributions en fer dissous et d'excès de baryum (Ba_{xs}) qui est un proxy de la réminéralisation mésopélagique, ont été mesurés dans toute la colonne d'eau, à sept stations le long de 30°E dans le sud de l'océan Indien au début de l'hiver austral 2017. Nos résultats suggèrent que la reminéralisation est maintenue à des niveaux comparables à l'été, bien après la fin de la floraison, au début de l'hiver.
Concernant le fer dissous, les concentrations hivernales ne sont pas significativement différentes des observations estivales mesurées dans l'ouest de l'océan Indien Austral, restant à des concentrations sub-nanomolaires, de 0.02 à 0.73 nmol L^{-1}. Les concentrations dans les eaux de surface sont diminués, indiquant qu'en juillet, il n'y a pas encore eu de reconstitution du stock de fer dissous dans les eaux de surface. Les distributions de fer dissous et d'excès de baryum présentent des pics dans les eaux intermédiaires sur les profils de colonne d'eau, indiquant une reminéralisation du fer.
En utilisant le proxy d'utilisation apparente de l'oxygène nous avons estimé qu'une fraction importante (de 58 ± 1 à 160 ± 2 %) du stock de fer dissous mésopélagique mesuré était fourni par reminéralisation.

Title : Insights into early winter Southern Indian Ocean dissolved iron distributions and remineralisation using excess barium (GEOTRACES GIPr07 cruise)

Keywords : Southern Ocean, winter barium excess, winter iron cycling, remineralisation

Abstract : The Southern Ocean is of central importance to the global ocean, connecting the Atlantic, Pacific and Indian basins via the Antarctic Circumpolar Current, which carries large amounts of heat, carbon and nutrients. Thus, this oceanic province partly regulates the Earth's climate. One of the factors influencing the biological carbon pump of the Southern Ocean is the availability of iron, which is an essential nutrient for phytoplankton. However, observations in this region have mainly been conducted in spring and summer, leaving significant gaps in our knowledge of the biogeochemical cycle of iron, in particular on the seasonality of internal processes such as mesopelagic remineralisation.
During this study, the distributions of dissolved iron and excess barium (Ba_{xs}), a mesopelagic remineralisation proxy, were measured throughout the water column, at seven stations along 30°E in the Southern Indian Ocean during early austral winter of 2017. Our results suggest that remineralization is maintained at comparable levels as observed during summer, well after the bloom decline, at the onset of winter.
Regarding dissolved iron, the winter concentrations were not significantly different to summer observations in the western Southern Indian Ocean, remaining at sub-nanomolar concentrations, from 0.02 to 0.73 nmol L^{-1}. Concentrations in surface water were depleted, indicating that in July there has not yet been a replenishment of the dissolved iron stock in surface waters.
The distributions of dissolved iron and Ba_{xs} exhibited peaks in intermediate waters on the water column profiles, indicating iron remineralization. Using the apparent oxygen utilization proxy, we estimated that a large fraction (58 ± 1 to 160 ± 2%) of the measured mesopelagic dissolved iron stock was provided by remineralisation.